Role of Uncoupling Protein 2 in Right Heart Hypertrophy

Inaugural Dissertation

Submitted to the

Faculty of Medicine

in partial fulfillment of the requirements for the

PhD-Degree

of the Faculties of Veterinary Medicine and Medicine

of the Justus Liebig University Giessen

by

Esfandiary, Azadeh

of

Babol, Iran

Giessen, 2018

From the Department of Internal Medicine II

Director / Chairman: Prof. Dr. Werner Seeger

of the Faculty of Medicine of the Justus Liebig University Giessen

First Supervisor and Committee Member: Prof. Dr. Norbert Weissmann

Second Supervisor and Committee Member: Prof. Dr. Martin Diener

Committee Members: Prof. Dr. Klaus-Dieter Schlüter, Prof. Dr. Robert Naeije

Date of Doctoral Defense: 25.07.2018

Dedicated to:

My Beloved Parents
Fereshteh & Amir

Declaration

I hereby declare that the present PhD thesis is my original work and that it has not been previously presented in this or any other university for any degree. I have appropriately acknowledged and referenced all text passages that are derived literally from or are based on the content of published or unpublished work of others, and all information that relates to verbal communications. I have abided by the principles of good scientific conduct laid down in the charter of the Justus Liebig University of Giessen in carrying out the investigations described in the dissertation.

Azadeh Esfandiary

Giessen, Germany

Table of contents

Table of contents

Table of contents

Table of contents

Table of contents

List of tables

II. List of tables

List of figures

IV. List of figures

List of figures

List of abbreviations

IV. List of abbreviations

$[Ca^{2+}]_c$	Cytosolic Ca^{2+}
$[Ca^{2+}]_i$	Intracellular Ca^{2+}
$[Ca^{2+}]_m$	Mitochondrial Ca^{2+}
µl	Microliter
µm	Micrometer
ADP	Adenosine diphosphate
ALK-1	Activin receptor-like kinas
ATF6	Activating transcription factor 6
ATP	Adenosine triphosphate
au	Arbitrary unit
BAT	Brown adipose tissue
BH4	Tetrahydrobiopterin
BMCP1	Brain mitochondrial carrier protein 1
BMPR2	Bone morphogenic protein receptor type II
BNP	Brain natriuretic peptide
BSA	Bovine serum albumin
BW	Body weight
CaMKII	Ca^{2+}-calmodulin-dependent protein kinase II
cAMP	Cyclic adenosine monophosphate
CAV1	Caveolin-1
cDNA	Complementary DNA
CH	Chronic hypoxia
CICR	Ca^{2+}-induced Ca^{2+} release
CO	Cardiac output
COPD	Chronic obstructive pulmonary disease
COXII	Cytochrome c oxidase subunit II
CSA	Cross sectional area
CTEPH	Chronic thromboembolic pulmonary hypertension
DAPI	4 ', 6-diamidino-2-phenylindole dihydrochloride
DCA	Dichloroacetate

List of abbreviations

Doux	Dual oxidase
DTT	Dithiothreitol
E-C	Excitation-contraction
ECG	Electrocardiography
ECL	Enhanced chemiluminescence
ECM	Extracellular matrix
EF	Ejection fraction
EGTA	Ethylene glycol-bis (β-aminoethyl ether)
ENG	Endoglin
ER	Endoplasmic reticulum
ERK	Extracellular-signal regulated kinase
ET	Ejection time
ETC	Electron transport chain
FA	Fatty acid
FCS	Fetal calf serum
FHF	First heart field
FITC	Fluorescein isothiocyanate
GAPDH	Glyceraldehyde 3-phosphate dehydrogenase
H_2O_2	Hydrogen peroxide
HCL	Hydrogen chloride
IB4	Isolectin B4
ISO	Isoprenaline
HCX	H^+-Ca^{2+} exchanger
HEPES	4-(2-hydroxyethyl)-1-piperazine ethanesulfonic acid
HIF-1α	Hypoxia-inducible factor-1α
HIV	Human immunodeficiency virus
HPRT	Hypoxanthine-guanine phosphoribosyl transferase
HR	Heart rate
HRP	Horseradish peroxidase
IMM	Inner mitochondrial membrane

List of abbreviations

ISO	Isoprenaline
IVCT	Isovolumic contraction time
IVRT	Isovolumic relaxation time
IU	International unit
JNK	c-Jun N-terminal kinase
KCl	Potassium chloride
KCNK3	Potassium channel subfamily K member 3
KH_2PO_4	Monopotassium phosphate
KO	Knockout
LTCC	L-type Ca^{2+} channel
LV	Left ventricle
LVF	Left ventricular failure
LVH	Left ventricular hypertrophy
LVOT	Left Ventricular outflow tract
MAO	Monoamine oxidase
MAPK	Mitogen-activated protein kinase
MCT	Monocrotaline
MCU	Mitochondrial Ca^{2+} uniporter
MES	4-Morpholineethanesulfonic acid
MFN2	Mitofusin-2
$MgSO_4$	Magnesium sulfate
MI	Myocardial infarction
MMP	Matrix metalloproteinase
MPAP	Mean pulmonary arterial pressure
MPI	Myocardial performance index
mPTP	Mitochondrial permeability transition pore
MRI	Magnetic resonance imaging
mV/div	millivolts per division
NaCl	Sodium chloride
NADPH	Nicotinamide adenine dinucleotide phosphate hydrogen

List of abbreviations

NCX	Na^+-Ca^{2+} exchanger
NF-κB	Nuclear factor-kappa B
NHX	Na^+-H^+ exchanger
NO	Nitric oxide
NOS2	Nitric oxide synthase 2
NOX	NADPH oxidase
O_2	Oxygen
$O_2^{\bullet-}$	Superoxide
$^{\bullet}OH$	Hydroxyl radical
OMM	Outer mitochondrial membrane
OX-PHOS	Oxidative phosphorylation
PAB	Pulmonary artery banding
PAH	Pulmonary arterial hypertension
PASMC	Pulmonary artery smooth muscle cell
PBS	Phosphate buffered saline
PCR	Polymerase chain reaction
PDK	Pyruvate dehydrogenase kinase
PGI_2	Prostaglandin I_2
PH	Pulmonary hypertension
PK	Protein kinase
PKA	Protein kinase A
PKB	Protein kinase B
PKC	Protein kinase C
PLB	Phospholamban
PMSF	Phenylmethane sulfonyl fluoride
PN	Purine nucleotide
PP	Protein phosphatase
PPAR	Peroxisome proliferator-activated receptor
PPAR-α	Peroxisome proliferator-activated receptor-alpha
PPARGC-1β	peroxisome proliferative-activated receptor-gamma coactivator-1 beta
PPAR-δ	Peroxisome proliferator-activated receptor-delta

List of abbreviations

PPHN	Persistent pulmonary hypertension of the newborn
PVDF	Polyvinylidene fluoride
PVR	Pulmonary vascular resistance
RaM	Rapid mode of Ca^{2+} uptake
RHC	Right heart catheterization
RNA	Ribonucleic acid
RNS	Reactive nitrogen species
ROS	Reactive oxygen species
RT PCR	Reverse transcription PCR
RV	Right ventricle
RVF	Right ventricular failure
RVID	Right ventricular internal diameter
RVH	Right ventricular hypertrophy
RVSP	Right ventricular systolic pressure
RVOT	Right ventricular outflow tract
RVWT	Right ventricular wall thickness
RyR	Ryanodine receptor
S	Septum
SAP	Systemic arterial pressure
SDF1	stromal-derived factor 1
SDS	Sodium dodecyl sulfate
SEM	Standard error of mean
SERCA2a	Sarco(endo)plasmic reticulum Ca^{2+}-ATPase 2a
SGC	Soluble guanylate cyclase
SHF	Second heart field
SOD	Superoxide dismutase
SR	Sarcoplasmic reticulum
SV	Stroke volume
SVao	Aortic stroke volume
TAC	Transverse aortic constriction

List of abbreviations

TAPSE	Tricuspid annular plane systolic excursion
TBS	Tris buffered saline
TCA	Tricarboxylic acid
TDI	Tissue doppler imaging
Tempol	4-hydroxy-2, 2, 6, 6-tetramethylpiperidin-1-oxyl)
TNF-α	Tumour necrosis factor-alpha
TRITC	Tetramethylrhodamine-5 (-6) isothiocyanate
Trx1	Thioredoxin 1
UCP	Uncoupling protein
UCP1	Uncoupling protein 1
UCP2	Uncoupling protein 2
UCP3	Uncoupling protein 3
UCP4	Uncoupling protein 4
UCP5	Uncoupling protein 5
VEGF	Vascular endothelial growth factor
VTI	Velocity time interval
WGA	Wheat germ agglutinin
WT	Wild type
$\Delta\psi_m$	Mitochondrial membrane potential

Introduction

1. Introduction

1.1. The right ventricle (RV) under pressure

In recent years, earlier recognition and new treatment modalities have improved prognosis for patients with left heart failure. Unfortunately, still little is known about the cellular and molecular mechanisms that underlie right heart failure as well as therapeutic approaches. Moreover, the effects of current available treatments to improve the right heart function are not yet clear and more investigation in this respect is needed.

1.1.1. Structure and function of the RV

Left heart anatomy, function, and its response to acute cardiac events have been widely studied. Less is known about right heart development, physiology, and pathophysiology, and it remains relatively understudied. Right heart failure is substantially different from left heart failure due to their difference in anatomy and development [1]. First heart field (FHF) progenitor cells contribute exclusively to the development of the left ventricular (LV) myocardium while the second heart field (SHF) contributes to development of outflow tract and RV myocardium [2, 3]. Therefore, the difference in cardiac progenitor cells of RV and LV myocytes may result in structural, functional and geometric differences between the RV and LV [4].

The RV wall is much thinner compared to the LV and its mass is $1/6^{th}$ of that of the LV. The low volume to surface area ratio of the RV makes it a highly conformable chamber [4]. Sinus and cone are two anatomically and functionally different cavities in RV which generate and regulate systolic pressure respectively [4]. The RV and LV share a wall (septum) and share the pericardial space besides pericardial fibers [1]. The septum and RV wall have approximately an equal share in RV function [1]. Mammalian cardiomyocytes contain isoforms of β-myosin and α–myosin heavy chains mainly expressed in ventricles and atria, respectively, which in association with myosin light chains form a single hexameric unit [4]. The ventricles contract through interaction of myosin complexes with actin complexes.

The RV is responsible for pumping the same stroke volume as the LV. However, the RV requires 25% of the stroke work of the LV due to lower pulmonary vasculature resistance that is $1/10^{th}$ of the systemic vascular resistance. The RV delivers deoxygenated blood to the lungs for gas exchange and is structurally adapted for sustained low–pressure perfusion of the pulmonary circulation. Systolic pressures generated by the RV is dependent on the LV and right ventricular systolic pressure (RVSP) is greater when LV pressure is increased [4]. The RV has

no effect on the systolic pressure of the LV unless severe LV hypotension was present [4]. Altogether, the RV is dependent on the LV for at least a part of its contractility.

1.1.2. Right ventricular hypertrophy (RVH), right heart failure and remodelling

Our knowledge from left ventricular hypertrophy (LVH), failure, and remodelling can be partially helpful in recognition of RV failure (RVF) as both ventricles have different embryonic origins. RVF is a major determinant of morbidity and mortality in pulmonary vascular diseases such as acute pulmonary embolism and chronic pulmonary hypertension (PH). It is also a determinant in other non-pulmonary vasculopathies such as systemic hypertension [5, 6].

Right heart hypertrophy is divided into adaptive and maladaptive forms. Adaptive right heart hypertrophy is an adjustment of RV to increased afterload, leading to myocardial remodelling and concentric right heart hypertrophy. This situation is also called compensated right heart insufficiency with largely preserved right heart function. In contrast, the concept of maladaptive right heart hypertrophy reflects a lack of compensation for elevated right heart afterload by the right heart which results in eccentric hypertrophy. Eccentric maladaptive hypertrophy is accompanied by reduced right heart function and progressive symptoms of heart failure in decompensated RV insufficiency [7]. The mechanisms determining the transition between concentric and eccentric remodelling are still unclear.

Despite an increase in compliance to accommodate an increased volume, the capacity of the RV to respond to chronic pressure overload is finite and the RV will develop muscle mass accumulation (hypertrophy). Adaptive alterations to increased afterload include elevation of intraluminal pressure and increased wall stress [6]. The intraluminal pressure elevation leads to increased oxygen consumption in heart with concomitantly reduced myocardial perfusion [6]. The increased wall stress can be counteracted with a reduction in the intraluminal diameter or thickening of the wall in order to maintain cardiac output (CO) [8]. This adaptive myocardial hypertrophy is mediated via strain sensitive ion channels and integrins in cardiac cells and is enhanced by autocrine, paracrine and neurohumoral influences [9]. This results in alterations at cellular level, formation of extracellular matrix (ECM), and the growth of vascular cells [9]. If these compensatory mechanisms are exceeded, contractile dysfunction, myocardial fibrosis, right ventricular dilatation and right heart failure occur.

The transition from compensated to decompensated right heart failure is insufficiently characterized [5, 9]. At cellular level, increased pressure overload causes the myocyte damage or myocyte lost which results in remodelling as a compensatory response. In remodelling, the

cells undergo hypertrophy which includes increased size of cardiomyocytes, elevated protein synthesis, thickening of ventricular wall and increased cell contraction [10]. In left heart failure due to ischemia, increased diameter and length of cardiomyocytes as well as increased cross-sectional area (CSA) of cells are reported [10]. Alteration in re-expression of fetal-type contraction genes, changes in cellular energetic and metabolic status, changes in expression and/or function of excitation-contraction (E-C) coupling proteins, and subsequently myocyte death are other alterations in cardiac remodelling [6, 11]. At the compensated stage, adenosine triphosphate (ATP) production can be maintained by increased glycolysis, whereas e.g. reactive oxygen species (ROS)-dependent signalling pathways are involved in the induction of protein synthesis and formation of hypertrophy. Furthermore, the low levels of mitochondrial ROS result in induction of hypoxia-inducible factor-1α (HIF-1α) and decreased ratio of glycolysis to glucose oxidation [12]. The activated HIF-1α increases the proangiogenetic factors and chemokines such as vascular endothelial growth factor (VEGF) and stromal-derived factor 1 (SDF1) and subsequently increases the angiogenesis [12]. Upon transition to decompensated right heart failure, factors such as hypoxia, ROS and transcription factors, e.g., HIF-1α cause the mitochondrial dysfunction [12]. In more detail, elevated levels of mitochondrial ROS suppress the HIF-1α, reverse the glycolytic phenotype, and suppress the angiogenesis in the hypertrophied heart [12]. Respiratory capacity and complex V-dependent ATP production continue to fall. As a result of the decrease in mitochondrial glucose oxidation, the energy requirement cannot be covered despite increased glycolytic ATP production. This energy deficit has a direct effect on the systolic and diastolic function of the cardiomyocytes. The damage of the mitochondrial respiratory chain complexes, the resulting decrease in respiration and possibly a calcium overload of the mitochondria lead to a further massive ROS increase, which leads to an activation of apoptosis, necrosis and further damage to the mitochondria. In addition, impairment of the E-C coupling causes relaxation by an increase in the diastolic calcium concentration, while a possible decrease in the calcium peak in the systole can additionally reduce the contraction.

Increased RV wall tension under pressure overload activates signalling cascades in RV promoting fibrosis accompanied by ECM synthesis and vascularization [9, 13]. The predominant increase of collagen in the ECM network will affect ventricular size and shape [9]. Increased RV fibrosis and matrix metalloproteinase (MMP) signalling leading to abnormal ECM degradation impairs cardiac function and may contribute to reduced ventricular compliance [9, 14]. The aberrant ECM degradation in decompensated heart hypertrophy is mediated by increased tumour necrosis factor-α (TNF-α) , chymase and tryptase secretion

leading to MMPs activation [9]. Furthermore, RV hypertrophy in rabbits is associated with increased collagen synthesis and diminished collagen degradation [15]. Moreover, increased fibrosis is found in pulmonary arterial hypertension (PAH) patients as well as in rats with right heart hypertrophy [9].

In the left heart, it is already shown that the contractile dysfunction is associated with alterations in contractile proteins, deficiency of E-C coupling, mitochondrial defects and a decrease in the phosphorylation potential of the ATP. Moreover, extracellular changes in the matrix and fibrosis formation, possibly triggered by hypoxia and enhanced by insufficient vascularization, contribute to the development of heart failure [5, 9]

The mechanisms involved in cardiac hypertrophy lead to increased oxygen demand and promoted myocardial angiogenesis to maintain the contractile function. Thus, the interaction between cardiomyocytes and microvasculature plays an important role [16]. Improved ventricular function could be achieved by an increased capillary density in the RV by Iloprost administration.[17]. Iloprost is a synthetic analogue of prostaglandin I_2 (PGI_2) that dilates systemic and pulmonary arterial vascular beds. Furthermore, the role of ischemia in progressive right heart failure is evident by stress-induced angina, decreased systolic epicardial blood flow and diminished myocardial perfusion in PH patients [18-20]. Lack of angiogenesis plays a central role in transition from compensated to decompensated left heart failure [21]. Furthermore, a mismatch between the number of capillaries and size of cardiomyocytes in left heart may cause myocardial hypoxia, cardiac contractile dysfunction, apoptosis and cardiac hypertrophy [9]. This mismatch during LV hypertension resulted in transition from adaptive hypertrophy to heart failure, but little is known about the role of angiogenesis in RVH [9]. In the transverse aortic constriction (TAC) animal model for pressure overload-induced cardiac hypertrophy and heart failure, the number of microvessels per myocytes was initially increased, but, then declined [9]. Monocrotaline (MCT)-induced PH is accompanied by reduced capillary density in the RV of rats in contrast to the chronic hypoxia (CH)-induced PH model in rats [22]. In this model, it has been shown that angiogenesis is dependent on the expression of the VEGF [22].

Understanding the pathways involved in cardiac remodelling as well as gaining insight into the relationship between remodelling and heart failure progression might result in developing novel therapeutic targets.

1.1.3. Oxidative and nitrosative stress in cardiac hypertrophy and failure

ROS such as superoxide ($O_2^{\bullet-}$) and the hydroxyl radical ($^{\bullet}OH$) or other non-radical oxidative agents such as hydrogen peroxide (H_2O_2) are detrimental to proteins, lipids, and DNA. Damage can lead to deterioration of cellular functions. Reactive nitrogen species (RNS) are molecules derived from nitric oxide (NO^{-}) and $O_2^{\bullet-}$, e.g. produced by the inducible nitric oxide synthase 2 (NOS2) and the nicotinamide adenine dinucleotide phosphate hydrogen (NADPH) oxidase, respectively. RNS act in combination with reactive ROS to damage cells.

Potential sources of ROS inside the cell include NADPH oxidases (NOX 1-5 and Doux 1-2), cyclooxygenases, xanthine oxidases, cytochrome P450 enzymes, lipoxygenases, NO synthases and mitochondria [23-27]. In mitochondria, complex I and complex III of electron transport chain (ETC) are known the main sources of ROS generation via " electron leakage" during respiration [26, 28-31]. Impaired mitochondrial function is associated with increased ROS generation that impairs tricarboxylic acid (TCA) cycle and ETC complexes and subsequently disturbs mitochondrial ATP production. Mitochondrial respiratory chain complexes, xanthine oxidases, the uncoupled NO synthase, monoamine oxidases (MAO) and NADPH oxidases are the major known sources of ROS in left heart hypertrophy and heart failure [26].

Besides detrimental effects of ROS, a wide range of physiological roles in biological processes including intracellular homeostasis, adaptation to cellular stress such as hypoxia as well as autophagy and immune regulation are proposed to them [32, 33]. However their effect seems to be concentration dependent, as excessive ROS can cause deleterious effects by overwhelming antioxidant defences resulting in pathologies such as development of heart failure.

With regard to their function in the heart, ROS and RNS are involved in redox signalling and contribute to cardiac contraction, hypertrophy, and cardiac disease. ROS activate several enzyme/gene cascades in cardiac disorders. Protein kinases B (PKB) and C (PKC) and mitogen-activated protein kinases (MAPKs) such as extracellular signal–regulated kinase (ERK), p38-MAPK, nuclear factor-kappa B (NF-κB), and c-Jun N-terminal kinase (JNK) are redox-modulated proteins and they play an important role in left heart failure [25, 26]. ROS in high concentration induce apoptosis and necrosis of myocytes via p38- MAPK and JNK [34]. Moreover, the level of oxidative stress-induced apoptosis in cardiomyocytes appears to be dependent upon the level of ROS produced [27]. In other words, level of ROS is a determinant of myocyte phenotype via activation and interplay of multiple kinase signalling pathways including JNK, ERK1/2 and PKB which reflect pro-apoptotic or anti-apoptotic effects [27].

ROS lead to cardiomyocyte hypertrophy via one of the main molecular mechanisms which is thioredoxin 1 (Trx1)-sensitive oxidation of G protein Ras [26]. NOS particularly NOS3 is a source of ROS in regard to RVH [35]. NOS3 uncoupling occurs in myocardium exposed to chronic pressure load, and this serves as a major source for myocardial ROS, which is linked to dilative hypertrophy remodelling [35]. Furthermore, increased NOX2 expression and activation is demonstrated during chronic cardiac hypertrophy and in cardiac biopsies from patients with left heart failure [26]. Increased generation of ROS and RNS induces contractile dysfunction via suppression of enzymes responsible for E-C coupling as well as polynitrosylation of the ryanodine receptor (RyR) [9].

In the RV, increased mitochondrial complex II expression and ROS generation are observed in MCT-induced PAH rats compared to control group [36]. Furthermore, generation of extra mitochondrial- and mitochondrial-ROS is increased in the severely hypertrophied RV of PAH rats [37]. Sutendra et al showed that transition from compensated RVH to maladaptive RVH is accompanied by an increase in mitochondrial ROS leading to HIF-1α inhibition and attenuation of angiogenesis [12]. Furthermore, mitochondrial NOX4–derived ROS generation and mitochondrial dysfunction is implicated in autophagy and results in remodelling of the RV and LV in murine model of right heart hypertrophy [38]. Therefore, addressing increased ROS production could be a therapeutic target in the treatment of cardiac hypertrophy and heart failure [39-41].

1.1.4. Animal models to study RVH

Various species ranging from mice to primates has been utilized as models of RVH to study anatomic, pathophysiologic and molecular adaptations of right heart to increased pressure.

Most models used for RVH are rodents, particularly mice. Despite the increased costs and effort, large animal models are still used as they provide us with additional insight that can not be gained from rodent models due to significant differences between mice and humans in terms of heart rate (HR), oxygen consumption, contractile protein expression and response to loss of regulatory proteins. Animal models can provide insights about the determinants of right ventricular dysfunction, biomarkers and molecular patterns associated with RVH.

Hypoxia-induced RVH

Chronic exposure of animals to hypoxia is the most common PH model resulting in pulmonary vasoconstriction, with subsequent vascular remodelling which in turn will culminate in the development of PH as well as right heart hypertrophy. This model has greatly contributed to

understanding the molecular processes involved in the vascular remodelling induced by chronic pulmonary disease and oxygen deprivation. CH can be induced by exposing animals normobaric or hypobaric hypoxia [42]. CH model is used in a wide variety of animals including mice, rats, guinea pigs, dogs, cows, pigs and sheep [43, 44]. This classic model produces PH with some variability across species. For example, the degree of hypoxia-induced PH developed in mice is rather modest as compared to bovines [45]. CH is characterized by mostly mild-to-moderate pulmonary vascular and RV remodelling [42, 46]. Therefore, this model is only partially suited to investigate the mechanisms of human PH [44].

MCT-induced RVH

The MCT model is another classical PH model currently used in rats by oral administration of monocrotaline phytotoxin [43]. Two weeks after MCT administration, progressive remodelling of the pulmonary vasculature occurs which results in elevated pulmonary vascular resistance (PVR), PH development and finally RV hypertrophy and failure. The MCT model has contributed to an improved understanding of vascular remodelling in PH and serves as a model system for severe PH [47]. This model has been particularly beneficial in investigating the role of lung injury and chronic inflammation in pulmonary vascular diseases [47]. The complex obliterative lesions found in human patients with severe PAH do not develop in this rodent model [47].

Additional advantages of the MCT PH model are its technical simplicity, reproducibility, and low cost compared with other models [47]. Furthermore, the investigation of functional, structural, and molecular changes accompanied with RV compensated hypertrophy and RVF will be possible in this model [48-52]. This model allows precise measurements of CO besides right ventricular and central pulmonary arterial compliance [45]. The bigger size of rat plays a role in more precise measurement of cardiac factors. Interestingly, MCT has been found to be ineffective in mice [45].

Pulmonary artery banding (PAB)

In our study, PAB model in mice is used to investigate the RVH due to increased afterload. The surgical technique of PAB was first described by Muller and Dammann in 1952 as a model of pressure-induced RVH and RVF [44, 53]. The PAB model is induced by putting a constricting band or clip around pulmonary artery/trunk. Clinically it is used as a temporary surgical palliation to prevent excessive pulmonary blood flow in congenital cardiac defects with large left-to-right shunts [54]. RV strain due to pulmonary artery/trunk stenosis in PAB results initially in compensated hypertrophy. If untreated, RV will progress to decompensated hypertrophy and right-sided heart failure. Therefore, the PAB model is ideally suited to

investigate mechanisms underlying the progression from compensated to decompensated RVH. Pressure-induced right heart strain resulting in significant RVH is the central feature of the PAB model [45]. Unfortunately, the high operative mortality rate associated with this model is a disadvantage of this model. Given the technical difficulty of the surgery itself prohibits PAB from being a more common model for right heart failure studies [53]. The extremely thin fragile wall of the pulmonary trunk and the inability of the RV to withstand stress while the pulmonary artery is being manipulated are the challenges while performing this operation [53]. Because of low blood pressure in the RV any dissection underneath the pulmonary trunk using forceps may lead to blockage of blood flow to the lungs and consequently results in immediate respiratory and cardiac distress [53]. In CH and MCT models, the effect of increased afterload cannot be discriminated from the impact of hypoxia and / or MCT treatment. In line with this, MCT has been shown to induce myocarditis in rats complicating thus the study of the RV hypertrophy and failure [55]. In PAB model, right heart hypertrophy can be examined as a primary disease and not as secondary symptom of PH, which can be seen in the CH and MCT models [56].

1.2. Pulmonary hypertension (PH)

1.2.1. PH definition and classification

PH is the leading cause of RVH and RVF. It is a complex and multifactorial disease caused by functional and structural changes in the pulmonary vasculature. PH is characterised by vascular constriction leading to elevated pulmonary arterial resistance, vascular remodelling, RVH, and ultimately RVF. It is defined by elevated resting mean pulmonary artery pressure (MPAP) which is equal or more than 25 mmHg measured by right heart catheterization (RHC) [57, 58].

PH is classified by etiology, which was last revised in 2013 [59, 60]. PH is divided into five main subtypes according to pathological, pathophysiological and therapeutic characteristics: 1) PAH; 2) PH due to left heart disease; 3) PH associated with respiratory system disorders and/or hypoxia ; 4) chronic thromboembolic PH (CTEPH) or embolic PH; and 5) PH with unclear and/or multifactorial mechanisms [60, 61] (Table 1). PAH is a rapidly progressing disease with mortality rate of 20-40% at 3 years after diagnosis [9].

Table 1. Clinical classification of pulmonary hypertension, Nice, France, 2013[60]

1. PAH
1.1. Idiopathic PAH
1.2. Heritable PAH
1.2.1. BMPR2
1.2.2. ALK-1, ENG, **SMAD9, CAV1, KCNK3**
1.2.3. Unknown
1.3. Drug and toxin induced
1.4. PAH associated with
1.4.1. Connective tissue diseases
1.4.2. HIV infection
1.4.3. Portal hypertension
1.4.4. Congenital heart diseases
1.4.5. Schistosomiasis
1'. Pulmonary veno-occlusive disease and/or pulmonary capillary hemangiomatosis
1". Persistent pulmonary hypertension of the newborn (PPHN)
2. PH due to left heart disease
2.1. Left ventricular systolic dysfunction
2.2. Left ventricular diastolic dysfunction
2.3. Valvular heart disease
2.4 Congenital/acquired left heart inflow/outflow tract obstruction and congenital cardiomyopathies
3. PH due to lung diseases and/or hypoxia
3.1. Chronic obstructive pulmonary disease (COPD)
3.2. Interstitial lung disease
3.3. Other pulmonary diseases with mixed restrictive and obstructive pattern
3.4. Sleep-disordered breathing
3.5. Alveolar hypoventilation disorders
3.6. Chronic exposure to high altitude
3.7. Developmental lung diseases
4. CTEPH
5. PH with unclear multifactorial mechanisms

5.1 Hematologic disorders: **chronic hemolytic anemia**, myeloproliferative disorders, splenectomy
5.2 Systemic disorders: sarcoidosis, pulmonary histiocytosis, lymphangioleiomyomatosis
5.3 Metabolic disorders: glycogen storage disease, Gaucher disease, thyroid disorders
5.4 Others: tumoral obstruction, fibrosing mediastinitis, chronic renal failure, **segmental PH**

***5th WSPH Nice 2013. Main modifications to the previous Dana Point classification are in bold. BMPR2 = bone morphogenic protein receptor type II; CAV1 = caveolin-1; ENG = endoglin; HIV = human immunodeficiency virus; PAH =pulmonary arterial hypertension.**

1.2.2. Pathophysiology of PH

The pathophysiology of PH is complex and multifactorial. Different pathobiological features characterize the clinical PH groups [62].

PAH (group 1) is caused by increased PVR. Vasoconstriction, obstructive remodelling of the pulmonary vessel wall, inflammation and thrombosis are the main factors responsible for the elevated resistance of the pulmonary circulation. All cell types of the pulmonary arterial vessel are affected in PAH. Furthermore, the release of cytokines and chemokines from activated endothelial cells mediates the influx of inflammatory cells such as monocytes, T or B lymphocytes contributing to pulmonary artery smooth muscle cell (PASMC) proliferation [63].

In PH due to left heart disease (group 2), elevated left atrial pressure induces reactive PH. Chronic left heart failure may be due to systolic or diastolic cardiac dysfunction or due to valvular diseases [64].

PH due to lung disease and/or hypoxia (group 3) is characterized by multiple mechanisms including hypoxic vasoconstriction, mechanical stress of hyperinflated lungs, loss of capillaries, inflammation as well as toxic effects of inhalative agents e.g. cigarette smoke [65].

CTEPH (group 4) is induced by failure to resolve acute emboli that later undergoes fibrosis resulting in mechanical obstruction of the pulmonary arteries. Abnormalities in platelet function or in the coagulation cascade may cause or aggravate the initial thrombosis and provoke a chronic obstruction of the vascular bed [66].

Group 5 consists of several forms of PH with an unclear or multifactorial etiology as well as heterogenic pathophysiology. Various pathologies such as hematological disorders, systemic disorders, metabolic disorders or patients with chronic renal failure are grouped in this category [67].

1.2.3. Diagnosis and treatment of PH

RHC is the gold standard in the diagnosis of PH, allowing for measurement of pulmonary artery pressure and CO [4, 57, 59]. Transthoracic echocardiography is the main non-invasive diagnostic tool to evaluate PH and its severity. Brain natriuretic peptide (BNP) and troponins are two biomarkers that are frequently elevated in PH due to myocardial stretch and ischemia. These biomarkers can be used to evaluate severity in PH, but they are not sensitive and specific for diagnosis alone [68, 69]. Magnetic resonance imaging (MRI) is utilized to assess RV mass, RV volume and RV ejection fraction (EF) in PH associated with RV failure [14].

Current available treatments for most forms of PH only attenuate the progression of PH, with an overall poor diagnosis with lung or combined heart-lung transplant being the only therapeutic options. Supportive treatments include anticoagulation, diuretics and oxygen (O_2) therapy [59]. Pharmacologic treatments targeting some of the underlying molecular pathways in PH include soluble guanylate cyclase (SGC)-stimulators, prostacyclin derivatives, endothelin receptor antagonist and phosphodiesterase 5 inhibitors [4, 9, 59, 70, 71].

RV adaptation to PH determines the clinical prognosis. Although there are numerous therapeutic options for left ventricular failure (LVF), only a few specific interventions to support RV function and prevent right heart failure are currently available. These interventions are mostly indirect and non-selective. A poor understanding of the underlying pathophysiology of RVH and RVF results in scarce pharmacologic treatment options [4, 5]. Available treatments for RVF in PH are diuretics and continuous intravenous inotrope infusion [5].

Novel therapies for the pulmonary vasculature and RV in PH are aimed to target mitochondria, for example Archer et al showed that inhibition of the pyruvate dehydrogenase kinase (PDK) by dichloroacetate (DCA) partially reverts RVH by restoring mitochondrial membrane potential ($\Delta\psi_m$) and improving glucose oxidation [72] . Another emerging concept to treat RV failure is to inhibit mitochondrial fission and promote mitochondrial fusion [73].

1.3. Mitochondria and the heart

Mitochondria are the power plant of the cell and play an important role in ATP production, ROS production and detoxification, metabolism, apoptosis, and cellular Ca^{2+} homeostasis [74, 75]. As mitochondria occupy at least 30% of the cardiac cell volume, mitochondrial dynamics are a particular focus in cardiac research.

1.3.1. Role of mitochondria in heart function and heart failure

Myocardial mitochondria play a central role in cellular energy production, generation and scavenging of ROS, intracellular calcium ($[Ca^{2+}]_i$) homeostasis, and regulation of apoptosis and growth [76]. Mitochondrial dysfunction may result in maladaptive right ventricular remodelling and transition from compensated to decompensated right heart failure. Conversely, healthy mitochondria may support adaptive remodelling and function of the RV.

An increasing number of studies are focusing on right heart dysfunction and its related mitochondrial abnormalities. In regard to mitochondrial metabolic alterations, reduced glucose oxidation and increased glycolysis are found in MCT-induced RVH in rats [72]. Moreover, Fang et al have shown increased RV fatty acid (FA) oxidation and reduced glucose oxidation in rats exposed to PAB operation [77]. Dysfunctional RVH in hypoxia-induced right heart hypertrophy model in rats is characterized by a gene expression profile compatible with impairment of FA and glucose oxidation [78]. Elevation of glycolysis-related genes expression and higher PDK-mediated glycolytic shift were observed in two rat models of RVH [72, 79]. In early stages of hypertrophy in dogs and rats, FA metabolism is compromised [80]. Conversely, no significant decline in FA oxidation could be detected in mild and compensated hypertrophy induced by suprarenal aortic banding in rats [80]. This is in line with a finding in a canine model of coronary microembolization-induced heart failure in which no decrease in FA oxidation was observed during compensated stage compared to healthy animals [81]. Additionally, in compensated hypertrophy induced by abdominal aortic constriction in rats, glycolysis was modestly increased with unchanged glucose oxidation [82]. Moreover, following aortic constriction in rats, cardiac glucose oxidation tended to increase initially, but, was unchanged in the phase of compensated hypertrophy and decreased when systolic dysfunction occurred [82]. These findings suggest the decreased mitochondrial ATP production in advanced LVF. A reduction in total and mitochondrial creatine kinase activity, a slight decrease in ATP concentration and a significant decrease of creatine and phosphocreatine occurred during the transition from compensated to decompensated heart failure [83, 84]. This reduced energy reserve may contribute to the progression of heart failure, although it is still a question whether it is sufficient to be a primary divert of heart failure [85]. Also, in hypertrophied isolated perfused RVs from ferrets a decreased phosphocreatine and creatine content as well as a decreased creatine kinase activity were observed while ATP level was unchanged. The ATP content could be maintained by enhanced glycolysis [86]. In patients with precapillary PH, elevated myocardial glucose uptake and shift of FA oxidation to glucose oxidation were seen in the development of cardiac hypertrophy [87]. Moreover, a shift towards

elevated FA oxidation and glycolysis associated with RVF is reported in PH patients [88]. Furthermore, a lower FA oxidation with restricted RV function was observed in PH patients [89].

Decreased mitochondrial capacity for oxygen consumption and oxidative phosphorylation are observed in MCT-induced right heart hypertrophied rats which highlight the alteration of mitochondrial energy-producing ability in RVF [90]. Reduced mitochondrial respiration at complex I of the ETC is observed in rats with hypoxia-induced right heart hypertrophy which had dysfunction of RV [78]. In a rat model of CH-induced heart hypertrophy; mitochondrial respiration was compromised in the LV within 24 h of hypoxic exposure and remained reduced afterward while it was unaffected in the RV [91]. Moreover elevated mitochondrial respiration via an increase in number of mitochondria was detected in hypoxia-induced RVH model in rats [92, 93]. In the neonatal rabbit model of thoracic aortic banding-induced pressure overload hypertrophy, activity of complex I and III of the mitochondrial respiratory chain is reduced during compensated hypertrophy, which was associated with diminished ROS and oxidative damage at the phase of transition to heart failure [94].

These studies suggest that the RV is also subjected to metabolic remodelling during the formation of hypertrophy, with various findings depicting that hypertrophy of the right heart is partially different from that of the left heart. The inhibition of mitochondrial respiration could be compensated in the short term by increased glycolytic ATP production. This compensation thus contributes as an adaptive mechanism to maintain the RV function. However, since the glycolytic ATP production is less efficient than the oxidative ATP production and also it leads to lactic acidosis, it may not be able to compensate for the increased energy requirement in the case of progressive hypertrophy in the long term. This hypothesis is supported by the finding that an increase in mitochondrial metabolism by DCA leads to an improvement in right ventricular function [72]. In the stage of compensated cardiac insufficiency the diminished mitochondrial ATP production can be compensated by an increased glycolytic activity [80].

The RV undergoes a metabolic remodelling and alteration in mitochondria biogenesis and function during hypertrophy. It is still debateable whether these changes are secondary effects in heart failure or if the primary mitochondrial alterations lead to heart failure. The role of structural and functional changes of mitochondrial respiratory chain complexes, mitochondrial membrane proteins, and proteins involved in ROS and calcium homeostasis specifically in the transition from compensated to decompensated right heart failure need to be further explored.

1.3.1.1. Mitochondrial ROS in right heart hypertrophy

ROS can be generated during oxidative phosphorylation in the mitochondria as a by-product of normal aerobic metabolism [95]. Therefore, the main process by which the heart generates energy can lead to ROS production. ROS are the possible mediators of cardiac hypertrophy and contractile dysfunction. Interactions of ROS with E-C coupling pathways e.g. polynitrosylation of RyRs can cause functional impairment of the myocardium. In addition, ROS induce necrosis and apoptosis in higher concentrations via p38-MAPK and JNK [34]. The involvement of superoxides in myocardial hypoxia is also probable as superoxides are able to limit NO mediated vasodilation [96] . Characteristically, left heart failure is associated with excessive ROS production and lack of detoxification mechanisms. A down-regulation of peroxisome proliferator-activated receptor-alpha (PPAR-α) and mitochondrial superoxide dismutase (SOD) is involved in this process [97]. High ROS level results in generation of nitrotyrosine residues in tissue inhibitor of metalloproteinases and liberation of active MMPs which induce RV remodelling and fibrosis in a model of PAB [38]. Moreover, histological analysis of collagen content in RVs from PAB-induced right heart hypertrophy in mice demonstrated a significant increase of ROS in comparison with control mice [38]. An increased ROS production by complex II of the mitochondrial respiratory chain in conjunction with increased HIF-1α expression and activation of the p38-MAPK was responsible for the transition from compensated to decompensated right heart failure [27, 98]. The antioxidant EUK-1340, a superoxide dismutase superoxide and catalase mimetic, reduced myocardial hypertrophy and fibrosis in MCT-induced PAH in rats [99].

In connection with the increased pressure load of the RV, NO synthases, in particular NOS3, must be also considered as a source for ROS. The mechanical and oxidative stress under the increased afterload leads to the decoupling of the NO synthases during the formation of hypertrophy. In this state, the NO synthases provide a non-inconsiderable contribution to the ROS production and, apart from the formation of myocardial hypertrophy, are involved in a negative functional and structural remodelling. In addition, a down-regulation of their reducing co-factor tetrahydrobiopterin (BH4) in the pressure-loaded heart supports decoupling and thus accelerates the further production of radicals [35].

1.3.2. Mitofusin-2 and mitochondrial homeostasis in heart

Mitofusin-2 (MFN2) is a protein responsible for rearrangement of the outer mitochondrial membrane (OMM). This large GTPase is an essential mediator of mitochondrial fusion, a critical process of mitochondrial homeostasis [73, 100]. It is strongly expressed in heart tissue and its deficiency is associated with disturbance of the mitochondrial network in cultured

neonatal cardiomyocytes promoting early apoptosis in cells [101]. In addition to its localization in the mitochondria, large amounts of MFN2 are located on endoplasmic reticulum (ER) membranes where it facilitates the transfer of Ca^{2+} from the ER into the adjacent mitochondria, subsequently exposing mitochondria to very high local Ca^{2+} concentrations [100, 101]. High expression of MFN2 in the myocardium confirms its crucial role in ER-mitochondrial coupling in the heart. Ablation of MFN2 results in a change of the ER structure and ER fragmentation [100]. Cells lacking MFN2 have slower Ca^{2+} release from the ER associated with decreased mitochondrial Ca^{2+} uptake [100]. Pressure-induced hypertrophy in left heart caused downregulation of MFN2 in a compensatory mechanism mediated by peroxisome proliferator-activated receptor-delta (PPAR-δ) and PPAR-gamma coactivator-1 beta (PPARGC-1β) [100].

1.3.3. Mitochondrial uncoupling proteins (UCPs)

1.3.3.1. Definition, distribution and function of UCPs

Uncoupling proteins are a subfamily of the mitochondrial anion carrier protein family located in inner mitochondrial membrane (IMM) [102, 103]. Five isoforms of uncoupling proteins have been discovered thus far. UCPs contain six α-helical hydrophobic transmembrane domains by which they are inserted into the mitochondrial membrane. UCPs are proteins that uncouple oxygen consumption from oxidative phosphorylation (i.e. ATP production) [104] by catalysing proton transport across the inner membrane, thereby dissipating the proton electrochemical gradient built up by the respiratory chain [102]. UCP activity might be regulated by superoxide or ROS products [103]. UCPs might be protective against ROS and attenuate or prevent oxidative damage by decreasing the reduced state of the mitochondrial respiratory chain [102, 105]. Although the exact physiological/pathological functions of UCPs are still not fully understood, a few molecular functions are suggested for these proteins.

The best-characterized UCP to date, UCP1 is a 33-kDa tissue specific protein exclusively found in brown adipose tissue (BAT) of hibernators, small mammals and new-borns of large mammals. UCP1 is present in large number in the mitochondria and is required for cold-induced non-shivering thermogenesis in mammals [103, 105]. As the activity of an individual UCP1 is low, a large number of UCP1 complexes are required to ensure fast and complete uncoupling of respiration in order for thermogenesis [106]. This protein increases BAT respiration rate in response to hormonal stimuli by sustaining a free FA-induced purine nucleotide (PN)–inhibited H^+ conductance [102, 105, 107]. The sympathetic nervous system is a major factor for UCP1 activation [106].

Introduction

UCP2 and UCP3 are uncoupling proteins identified following UCP1 on the basis of their sequence similarity [107]. The mild-uncoupling hypothesis states that these two proteins are activated under specific stress situations to ameliorate the superoxide production [105, 106, 108]. They do not play a role in cold-induced thermogenesis and keep the $\Delta\psi_m$ at a low level in order to minimise ROS production [104, 105]. ROS production is higher in UCP2 or UCP3 knockout mice [106]. UCP2 and UCP3 may also be involved in the regulation of the resting metabolic rate as a basal proton leak in the IMM is associated with the resting metabolic rate [106].

UCP2 mRNA is detected in several cell types and tissues for example macrophages, lymphocytes, pulmonary cells, liver, spleen, brain, kidney, heart, digestive tracts and muscles [105, 106, 109]. Stress conditions stimulate UCP2 expression in certain areas of the brain and the liver [105] .The distribution of the UCP2 protein in the heart is controversially discussed [110]. UCP2 shares 72% of the amino acid sequence with UCP1 [106]. UCP2 mRNA levels are much higher than the actual protein [103]. The reason for this discrepancy might be related to 5´ non-coding region of mRNA that contains an additional open reading frame [103, 111]. The UCP2 gene is located on chromosome 11 in humans and chromosome 7 in mice, close to a region that has been linked to obesity and diabetes [109]. UCP2 is not very stable with a half-life of approximately 30 minutes [110, 112].

Very little is known about the physiological/pathological roles of UCP2 and its regulation despite its ubiquitous distribution. It should also be mentioned that the exact functions of UCP2 are not yet clearly understood. UCP2 may mediate proton leak across the IMM into the matrix and therefore decrease the $\Delta\psi_m$ [110, 113, 114]. As a mild uncoupler of oxidative phosphorylation (OX-PHOS), UCP2 may play a role in reduced mitochondrial-derived ROS production [35, 114-116]. Moreover, UCP2 seems to be involved in a “metabolic switch” described as compensatory increased FA entry into TCA cycle which occurs as a result of reduced/inhibited pyruvate entry. Furthermore, UCP2 probably is a sensor for the substrates entering the TCA cycle and may function as a carrier exporting pyruvate out of the mitochondrial matrix. This proposed function is consistent with increased FA oxidation and limited glycolysis –derived pyruvate utilization during starvation [108]. Of note, the $\Delta\psi_m$ can interfere with UCP2 function by limiting pyruvate export in case of insufficient mitochondrial polarization [108]. UCP2 operates cooperatively or sequentially with additional Ca^{2+} transport modulators and mechanisms across the IMM, as ATP-dependent inhibition of mitochondrial Ca^{2+} uptake is mediated via UCP2 [117]. Additionally, UCP2 is shown to play a role for

efficient mitochondrial oxidation of glutamine, an alternative fuel for the respiratory chain in absence of glucose, in human hepatocarcinoma cells [118]. In summary, UCP2 may influence mitochondrial respiration by decreasing $\Delta\psi_m$, regulate ROS, act as a calcium modulator, and negatively regulate pyruvate uptake into mitochondria thereby enhancing FA oxidation [119].

Suppression of UCP2 with antisense oligonucleotides increased $\Delta\psi_m$ and $O_2^{\bullet -}$ production in murine endothelial cells [3]. Interestingly, $O_2^{\bullet -}$ and products of lipid peroxidation activate UCP2. This highlights the potential role of UCP2 to be an effective regulator of $O_2^{\bullet -}$ production in mitochondria [120]. Genipin, a highly selective inhibitor of UCP2, increases $\Delta\psi_m$ and ATP levels via inhibition of proton leak [121]. Surprisingly, a loss of function of UCP2 in fibroblasts did not cause a significant increase in ROS production [111] which underscores the cell specific function of UCP2. In this murine model, the presence of UCP2 caused a decline in $\Delta\psi_m$, raised the respiration rate and reduced the sensitivity to uncouplers [111]. UCP2 is associated with decreased intracellular ROS concentration and resistance to degenerative processes [106]. UCP2 and UCP3 are shown to cooperatively play a role in mitochondrial Ca^{2+} uptake when highly expressed [122]. In this study, knock-down of UCP2 and UCP3 was neither additive nor synergistic in Ca^{2+} uptake [122].

UCP3 is also tissue specific and its mRNA is found predominantly in skeletal muscles of humans and rodents as well as BAT, white adipose tissue and heart of mice [102, 109, 123]. Traces of UCP3 are also detected in human heart [109]. UCP3 has 73% amino acid sequence homology with UCP2. UCP3 is involved in control of substrate utilization such as FAs without being a transporter of FA itself [105]. However, some studies show its role as a FA exporter outside of mitochondrial matrix [106].

So far, UCP4 and UCP5 are not characterized. UCP4 is a putative mitochondrial carrier that is more distant from other UCPs and is discovered in brain and UCP5 or brain mitochondrial carrier protein (BMCP1) is also found in brain [102, 106].

1.3.4. Mitochondrial coupling in right heart hypertrophy

Hyperpolarization of the $\Delta\psi_m$ in right heart hypertrophy appears to correlate with the development of hypertrophy [124]. A reduction of the mitochondrial proton leak has been observed in hypoxia-induced RVH [86, 92]. Hyperpolarization could serve as an adaptive mechanism for more efficient energy production in cardiac hypertrophy. However, how $\Delta\psi_m$ is augmented and how this affects mitochondrial ROS production is still unclear. Moreover, studies in a compensated LVH canine model induced by ischemia and re-perfusion injury did

not show a loss of $\Delta\psi_m$ [125]. In hypertrophied RVs of rats exposed to hypobaric hypoxia, mitochondrial O_2 consumption is raised despite of decreased mitochondrial proton leak which is associated with induction of transcript levels of a few genes including cytochrome c oxidase subunit II (COXII) and UCP2 as well as reduction of UCP3 [92].

1.4. Calcium homeostasis in cardiac physiology and pathology

1.4.1. Calcium dynamics in the heart

Calcium as a second messenger is the major regulator of a number of various cellular functions such as stimulation of ATP production, E-C coupling and muscle contraction. E-C coupling is one of the fundamental properties of cardiomyocytes which turns the electrical excitation of the cardiomyocytes into contraction of the heart. Tight regulation of $[Ca^{2+}]_i$ concentration and Ca^{2+} signalling in cardiac tissue is crucial, as phasic high amplitude Ca^{2+} transients govern contractions in the heart.

Subcellular mechanisms contribute to the transition from the resting state to contraction. During the cardiac action potential, depolarization of the cell membrane of the myocyte via Ca^{2+}-induced Ca^{2+} release (CICR) occurs. The membrane depolarization during the action potential opens sarcolemmal voltage-gated L-type calcium channels (LTCCs) and results in influx of low amounts of Ca^{2+} into the myocyte, triggering a large-scale Ca^{2+} release via stimulated RyRs which are Ca^{2+} release channels of the sarcoplasmic reticulum (SR). This increase of calcium termed "calcium spark" followed by binding of the released calcium to troponin C regulatory protein within the myofilaments activates the contractile machinery [126].

Heart relaxation is triggered by a decrease of cytosolic Ca^{2+} concentration. This process is initiated by dissociation of Ca^{2+} from troponin C. Its re-uptake to the SR is mediated by the sarco(endo)plasmic reticulum Ca^{2+}-ATPase 2a (SERCA2a) as well as Ca^{2+} removal from the sarcolemma by Na^+-Ca^{2+} exchanger (NCX) , albeit to a lesser extent [127-129]. As this is an energy-intensive process requiring high amount of ATP, the heart is one of the most mitochondrial-rich organs with mitochondria occupying approximately 30% of the volume of ventricular myocytes [100].

1.4.2. Regulatory components of mitochondrial calcium signalling

Defective EC-coupling in heart failure may be the result of an altered amount or function of proteins relevant for calcium homeostasis. The characterization of those alterations is a prerequisite for understanding the pathophysiology of myocardial failure and for the

development of new strategies to treat patients with heart failure. An overview of the major channels, transporters and proteins associated with calcium homeostasis in myocytes are shown in the figure 1.

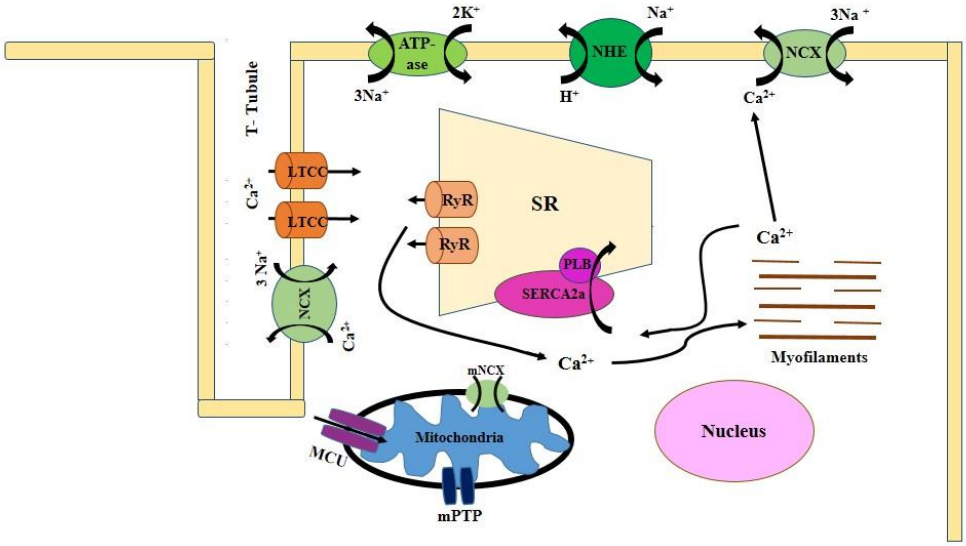

Figure 1. Cardiac cellular Ca^{2+} handling and Ca^{2+}-dependent signalling in adult ventricular cardiomyocyte

Intracellular Ca^{2+} ($[Ca^{2+}]_i$) is regulated by Ca^{2+} flux into the cytoplasm and via different transporters and channels: Ca^{2+} enters the myocyte through the L-type Ca^{2+} channel (LTCC), and activates the ryanodine receptor (RyR) to release Ca^{2+} from the sarcoplasmic reticulum (SR). The Ca^{2+} released from the internal stores, paired with Ca^{2+} entering through LTCC causes a rise in intracellular free Ca^{2+} that can bind to troponin C (that resides in myofilaments) to cause contraction. Ca^{2+} is then extruded from the cell via the Na^+-Ca^{2+} exchanger (NCX) or taken up by the SR via the sarco(endo)plasmic reticulum Ca^{2+}-ATPase 2a (SERCA2a). Na^+-H^+ exchanger (NHX) regulates the intracellular pH and transcellular Na^+ absorption. Na^+-K^+-ATPase pumps Na^+ out of the cell while K^+ is pumped in. Calcium enters the mitochondria primarily through the mitochondrial Ca^{2+} uniporter (MCU). Mitochondrial permeability transition pore (mPTP) increases the permeability of the mitochondrial membranes to molecules of less than 1500 Daltons in molecular weight.

In order for Ca^{2+} to enter the mitochondria, it diffuses freely through the highly permeable OMM. In order to enter the matrix, Ca^{2+} must pass through the IMM which is essentially impermeable to Ca^{2+}. There are three mechanisms for Ca^{2+} entry into mitochondria which the mitochondrial Ca^{2+} uniporter (MCU) is perhaps the most important one [130]. The MCU is an ion channel with high conductance and selectivity which drives the short term and massive

entry of Ca^{2+} ions into mitochondria [131]. Rapid mode of Ca^{2+} uptake (RaM) and mitochondrial RyR1 are the two other mechanisms responsible for Ca^{2+} entry into mitochondria [132, 133]. Three Ca^{2+} efflux pathways are also identified including the mitochondrial NCX, H^{+}-Ca^{2+} exchanger (HCX) and the mitochondrial permeability transition pore (mPTP).

1.4.2.1. Three crucial regulators of cardiac contractility

SERCA is one of the main Ca^{2+} regulatory proteins. SERCA is encoded by three genes SERCA1, SERCA2 and SERCA3 [127, 134]. SERCA2a is an isoform predominantly expressed in cardiac and slow twitch skeletal muscle [127, 134, 135]. SERCA2a mRNA and protein level in heart muscle and slow twitch skeletal muscle is 10- to 50-fold higher than its level in smooth muscle and non-muscle tissue [134]. SERCA2a is critical for cardiac development [135]. SERCA2a elevates myocyte relaxation by decreasing cytosolic Ca^{2+} concentration and active Ca^{2+} transport thus replenishing the $[Ca^{2+}]_i$ stores which subsequently provides Ca^{2+} for the next contraction [128]. SERCA2a is responsible for transporting two Ca^{2+} ions per every molecule of hydrolyzed high energy phosphate against the high ion gradient between the free $[Ca^{2+}]_i$ (100 nM-1 μM) and free Ca^{2+} in the SR (~1 mM) [127].

Phospholamban (PLB) is a small transmembrane protein expressed in cardiac and slow twitch skeletal muscle.This protein is located in the SR and plays an important role in calcium signalling of myocytes. It is one of the main mediators of the interaction between the β-adrenergic signalling pathway leading to protein phosphorylation and the Ca^{2+} signalling pathway leading to muscle contraction [129]. Stimulation of β-adrenergic signalling causes increased concentration of cyclic adenosine monophosphate (cAMP) and subsequent phosphorylation of PLB either by protein kinase A (PKA) or Ca^{2+}-calmodulin-dependent protein kinase II (CaMKII) [136]. PLB modulates SERCA2a by inhibiting the activity of SERCA2a and SR Ca^{2+} transport in its non-phosphorylated form, whereas phosphorylation of PLB at either Ser^{16} by PKA or Thr^{17} by CaMKII results in disruption of the ATPase-PLB interaction and removal of its inhibitory effects on SERCA2a which consequently accelerates Ca^{2+} uptake by the SR [127, 128, 136]. PLB can be dephosphorylated by protein phosphatases (PPs) including phosphatase type 1 (PP1) and type 2A (PP2A) in cardiomyocytes [126]. PP1 seems to have higher affinity to PLB [126]. PKA and CaMKII are also able to phosphorylate LTCC and RyR channels and thus regulate cardiac Ca^{2+}cycling [126].

The NCX plays the most dominant role in myocardial calcium efflux. The NCX in its forward-mode is responsible for extrusion of one Ca^{2+} ion for three Na^{+} ions [127, 137]. NCX is a voltage-dependent protein and can operate in reverse-mode at low stimulation frequencies or

during the action potential, promoting Ca^{2+} influx and prolongation of the Ca^{2+} transients in order to increase E-C coupling [127, 137].

1.4.3. Calcium signalling and ROS

Calcium interacts with other pathways including ROS. Interactions among ROS and calcium signalling can be considered as bidirectional, in which ROS can regulate cellular calcium signalling and calcium signalling is essential for ROS generation. Elevated levels of Ca^{2+} activate ROS-production which results in formation of free radicals. Because Ca^{2+} uptake leads to mild uncoupling of mitochondria and dissipation of the $\Delta\psi_m$, some of its effects on ROS generation may be due to this uncoupling effect [138]. The mechanism by which uncouplers enhance ROS generation is still under debate, but probably involves perturbation of the pH gradient across the mitochondrial membrane, which affects the topology of H_2O_2 generation [138].

Several calcium transporters or proteins which are localized in plasma membrane, can be regulated by ROS. In ventricular cardiomyocytes isolated from guinea pig, exogenous ROS suppressed L-type Ca^{2+} current irreversibly [139]. Moreover, ROS increased the $[Ca^{2+}]_i$ by stimulation of SR Ca^{2+} release via RyR channels and activation of Ca^{2+} entry via the reverse-mode of NCX in permeabilized rat ventricular myocytes [140]. In canine model of chronic heart failure, the ROS generated in the failing heart led to modification of RyR2 and its subsequent abnormal activity [141]. Furthermore, reduced cytosolic Ca^{2+} transients , elevated SR Ca^{2+} leak and reduced $[Ca^{2+}]_{SR}$ are demonstrated in this study [141]. Additionally, in Langendorff perfused rat hearts mild oxidative stress enhanced the Ca^{2+} response of RyR2 channels to cytoplasmic Ca^{2+} and this process was mediated by NOX2 [142]. In cardiomyocytes, mitochondria-derived ROS have been found necessary to maintain spontaneous RyR2-mediated Ca^{2+} spark activity while excessive mitochondrial ROS production exerted a bidirectional regulation of Ca^{2+} spark activity in a dose-and time- dependent fashion supporting a mitochondrial control of SR Ca^{2+} release [143]. In rat cardiomyocytes, stretch-induced NOX2-dependent ROS production in the sarcolemmal and t-tubule membranes sensitized the nearby RyR2 in the SR and triggered a burst of Ca^{2+} sparks, resulting in the induction of arrhythmogenic Ca^{2+} waves [144].

1.4.4. Calcium signalling and heart failure

Increasing evidences point to altered Ca^{2+} homeostasis as a highly relevant pathomechanism of heart failure characterized by abnormal contraction and relaxation as well as insufficient SR

Ca^{2+} uptake. Alterations in calcium signalling mostly occur due to disturbed function of the SR associated with impaired SR calcium content and subsequent prolongation of calcium transients. SR Ca^{2+} content reflects the balance between Ca^{2+} uptake and Ca^{2+} efflux. Diminished SR calcium content and its subsequent reduced systolic Ca^{2+} release from the SR as well as elevated diastolic Ca^{2+} concentrations in myocytes are well-known characteristics of heart failure [100, 145].

Several studies focused on components regulating Ca^{2+} dynamics as well as the expression and function of these components in cardiac pathologies. Alterations in Ca^{2+} uptake into the SR in left heart failure resulting in decreased Ca^{2+} concentration in the SR have been ascribed to decreased SERCA2a production, reduced levels of PLB phosphorylation and increased Ca^{2+} depletion of the SR via leaky RyR channels [11, 100]. These events tend to shift Ca^{2+} out of the cell and reduce SR Ca^{2+} content. Moreover, decreased expression and activity of SERCA2a is reported in the failing left heart in animal studies [128, 146]. Furthermore, reduced SERCA2a expression and function is known as a main parameter leading to diminished Ca^{2+} accumulation in the SR associated with disturbed systolic and diastolic function in isolated myocytes from failing left human hearts [147]. In the failing human heart, a decline of the PLB mRNA level was consistently observed, while no difference was found between the failing and non-failing left heart in PLB protein level [127, 148]. However, selective enhancement of PLB phosphorylation is beneficial for treatment of left heart failure [126]. Moreover, a partial or total lack of phosphorylation of PLB disturbed SR Ca^{2+} uptake and resulted in dilated cardiomyopathy and heart failure [126]. Also, improved SR Ca^{2+} cycling linked to left heart function and remodelling in animal models of heart failure occurred by transfer of gene encoding SERCA2a, production of a constitutively phosphorylated PLB, and deletion/ablation of gene encoding PLB [11, 100, 128, 145, 147]. Interestingly, increased SERCA2a protein expression and preserved SR Ca^{2+} loading were also observed in RV of post- myocardial infarction (-MI) rats which suggested SERCA2a may play a role in the preservation of RV function in post-MI rat model [149]. Decreased SR Ca^{2+} uptake in the LV and increased SR Ca^{2+} uptake in the RV were reported in the left heart failure in MI rats which depicted the different SR remodelling of the SR membrane with regard to Ca^{2+} pump mechanisms [150]. Accelerated NCX forward-mode activity resulting in declined SR Ca^{2+} content and systolic SR Ca^{2+} release is described in a canine model of left heart failure [151]. In transgenic mice overexpressing NCX, reverse-mode NCX resulted in accelerated Ca^{2+} storage of the SR [137]. Elevated NCX activity/expression in left heart failure and hypertrophy may compensate for depressed sarcoplasmic reticular Ca^{2+} uptake, provide inotropic support through reverse-mode

Ca^{2+} entry, and/or deplete $[Ca^{2+}]_i$ stores. Hasenfuss et al have shown that the expression of NCX mRNA and protein have been changed in failing left human heart [127]. Fang et al have demonstrated that MFN2 expression was downregulated in hypertrophied left hearts of rats and this downregulation was dependent on the etiology and time course of hypertrophy [152]. Moreover, MFN2 was reported as a main protein in modulating angiotensin-II-induced hypertrophy in neonatal rat cardiomyocytes and its upregulation inhibited the hypertrophy of these cells [153]. Moreover, human gene studies have detected the mutations of a few calcium cycling components in cardiomyopathies [154].

Other regulatory factors of $[Ca^{2+}]_i$ cycling also play important roles in cardiac failure. Although in most of left heart failures the density of LTCCs seems to be either unchanged or reduced, alteration in its function is demonstrated in studies [155, 156]. Functional defect in LTCC [157], the increase in the space between LTCC and RyR [158], and abnormality in the channel-gating property of RyR [159, 160] are the factors which resulted in reduced E-C coupling in left heart. Dysfunction of RyR including changes in its properties or its sensitivity to activation by L-type Ca^{2+} current may contribute to calcium handling alteration in left heart failure [161]. Altered phosphorylation levels of three $[Ca^{2+}]_i$ regulators PLB, LTCC and RyR in myocytes are shown in left heart hypertrophy and left heart failure [126]. It is proposed that, Phosphorylation of RyR channels by PKA or CaMKII causes leakage of Ca^{2+} from SR and induces Ca^{2+} handling dysregulation in myocardium and finally decline of left heart contractility [11]. In a study of MI model, CaMKII inhibition could prevent the progression of adverse cardiac remodelling [126].

In failing right heart, the alteration of these Ca^{2+} signalling components at mRNA and protein level, their function and abnormalities, as well as their contribution to development of right heart hypertrophy and its progression to right heart failure are not yet well clarified. To determine how these components influence the SR Ca^{2+} content, Ca^{2+} cycling as well as cardiomyocyte contractility and to clarify the underlying mechanisms, more investigation is needed. Moreover, although there are a limited number of key players among these regulatory components, they are subject to numerous levels of regulation and cross talk. Characterization of these regulations and interactions will need further investigations.

2. Aim of the study

There is still hardly proven therapeutic option for right heart hypertrophy which allows the simultaneous treatment and decompensation of right heart failure. Recently, major attention is paid to target the mitochondrial dynamics in heart failure etiology, diagnosis and treatment. Elucidating the functional and cellular effects of mitochondrial interventions on the development of cardiac hypertrophy and failure can help us to understand the underlying mechanisms. As failing myocardium upon pressure overload faces significant alterations in energy metabolism and from the other hand UCP2 is a critical protein in modulating energy metabolism, we hypothesized that UCP2 could contribute to the etiology of right heart hypertrophy. Also, based on critical functions of balanced calcium homeostasis in normal heart physiology the maintenance of calcium balance is central to cardiac contractility and function. So, assuming the imbalanced cardiac calcium haemostasis as one of the main problems in cardiac hypertrophy and failure made us interested in focusing on this topic.

In the present study a few main questions are going to be answered:

- Does UCP2 play a role in the pathogenesis of right heart hypertrophy?
- Which severities of right heart hypertrophy do the $UCP2^{-/-}$ mice develop?
- What are the functional characteristics of $UCP2^{-/-}$ mice after PAB operation *in vivo* and *in vitro*?
- What is the probable role of UCP2 in association with PAB operation in development of RVH?
- What are the probable effects of UCP2 in association with PAB operation in isolated cardiomyocytes with special focus on ROS and Ca^{2+} signalling regulatory components?

Aim of the study

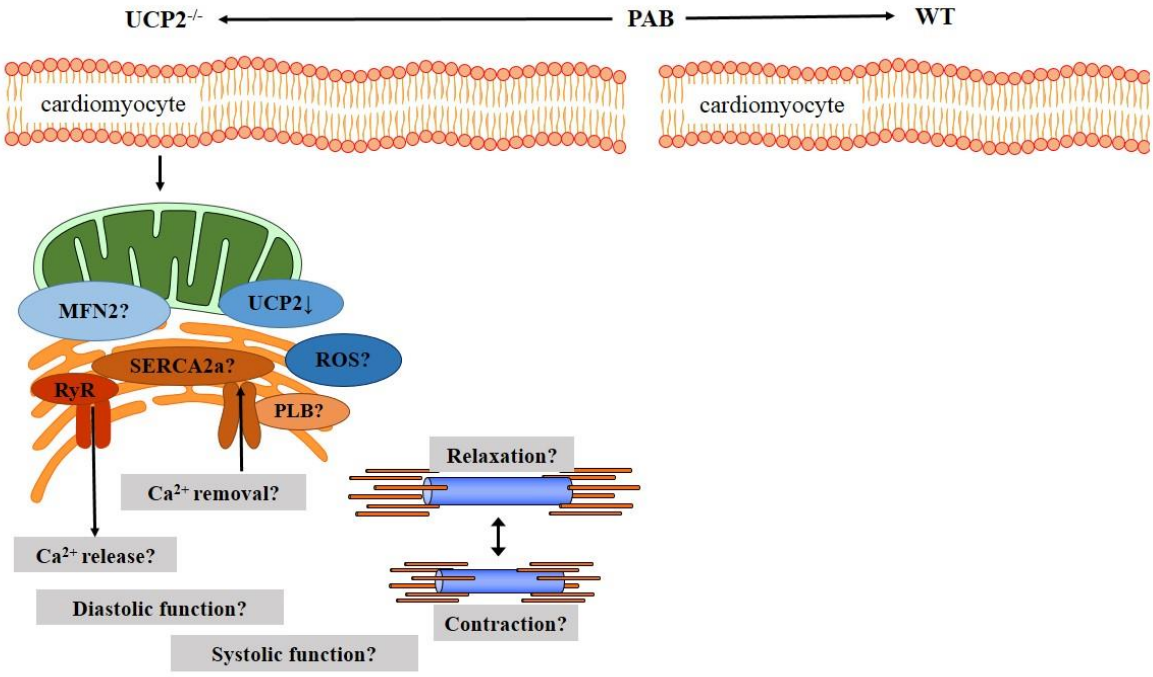

Figure 2. Effect of pulmonary artery banding (PAB) on calcium regulatory proteins in the cardiomyocytes

Does pulmonary artery banding (PAB) affect the calcium regulatory proteins; sarco(endo)plasmic reticulum Ca^{2+}-ATPase 2a (SERCA2a) and phospholamban (PLB) at cardiomyocyte level? Is PAB in $UCP2^{-/-}$ cardiomyocytes associated with alterations in calcium cycling? Does knockout of UCP2 ($UCP2^{-/-}$) affect the contractility of cardiomyocytes? Do PAB and $UCP2^{-/-}$ interact with ROS to play their role?

3. Materials and methods

3.1. Materials

3.1.1. Experimental animals

Adult male homozygous UCP2$^{-/-}$ mice (B6.129S4-Ucp2^{tm1Lowl}/J) were purchased from Jackson Laboratory (Bar Harbor, USA) and bred up to the 6th generation in our facilities. Male C57BL/6J mice bought from Charles River Laboratories (Sulzfeld, Germany) were used as wild type (WT) animals.

All mice used in the experiments had a weight of 22 to 28 gram each. During the experimental period, the animals were housed in the animal facility of the Excellence Cluster of Cardio-Pulmonary System (ECCPS) Institute of the Justus-Liebig University of Giessen.

3.1.2. Regional council's approvals for animal experiments

All animal experiments were performed according to the regulations of the regional authorities and ethics committees for animal research. Approval numbers are mentioned below:

GI 20/10 Nr. 86/2011

„ Rechtsherzhypertrophie- Rolle verschiedener ROS-Produzenten bei ihrer Entstehung“

GI 20/10 Nr. 40/2012

„ Rechtsherzhypertrophie und Mitochondrien “

3.1.3. Mouse model of PAB, echocardiography and hemodynamic measurements

Table 2. Substances and solutions

Substance	Trade name/ Description	Company
Buprenorphine hydrochloride	Temgesic®	Essex Pharma GmbH, Munich, Germany
50% 2-Propanol/1% Povidone iodine-solution	Braunoderm®	B. Braun Melsungen AG, Melsungen, Germany
Glucose 5%	Glucose 20%® Diluted 1:4	B. Braun Melsungen AG, Melsungen, Germany
Heparin	Heparin-Natrium-25000®	Ratiopharm GmbH, Ulm, Germany
Isoflurane	Isoflurane Baxter®	Baxter Deutschland GmbH, Unterschleißheim, Germany
Ketamine hydrochloride (100 mg/ml)	Ketamin 10%®	bela-pharm GmbH & Co, Vechta, Germany
Lidocaine hydrochloride	Xylocaine Jelly 2%	Astra Zeneca, Wedel, Germany
Potassium chloride (KCl)	30 mg/ml KCl	Carl Roth GmbH & Co, Karlsruhe, Germany
Physiological saline solution		DeltaSelect GmbH, Dreieich, Germany
Sodium chloride (NaCl) solution	Isotonic NaCl solution 0.9% ®	B. Braun Melsungen AG, Melsungen, Germany
NaCl solution (1000 ml)	for flushing and washing	B. Braun Melsungen AG, Melsungen, Germany
Ventilation gas 100% O_2		Air Liquid, Siegen, Germany
Xylazine hydrochloride	Xylazin 2%	Ceva Tiergesundheit GmbH, Düsseldorf, Germany

Table 3. Consumables

Article	Trade name/ Description	Company
Cannula 24G (0,55 mm x 25 mm) 26G (0,45 mm x 25 mm) 30G (0,3 mm x 25 mm)	BD Microlance 3®	Becton Dickinson, Heidelberg, Germany
Depilatory cream	Veet®	Veet, Heidelberg, Germany
Dexpanthen ophtalmic ointment	Bepanthen® eye and nasal ointment	Bayer Vital, Leverkusen, Germany
Embedding cassette, small size	Rotilabo®-embedding cassette Macro	Carl Roth GmbH & Co, Karlsruhe, Germany
Embedding cassette, big size	Tissue-Tek® Uni-Cassette®	Sakura Finetek Europe, Zoeterwoude, Netherlands
Falcon tube 15 ml, 50 ml	Cellstar® Tubes	Greiner Bio-One GmbH, Frickenhausen, Germany
IV Catheter, 14G x 2", 20G x 1¼"	Vasofix® Safety	B. Braun Melsungen AG, Melsungen, Germany
Medical adhesive band	Durapore®	3M, St. Paul, USA
Parafilm		American National Can Co, Menasha, USA
Scalpel	Feather® Disposal Scalpel	Pfm Medical AG, Cologne, Germany
Eppendorf tube	1,5 ml & 2 ml tube	Sarstedt AG & Co, Nümbrecht, Germany
Single use nitrile glove	Peha soft® Nitrile	Paul Hartmann AG, Heidenheim, Germany
Single use glove	Vasco® Nitril White	B. Braun Melsungen AG, Melsungen, Germany
Single use syringe, 1 ml, 2 ml, 5 ml, 10 ml, 20 ml	Inject Luer®	B. Braun Melsungen AG, Melsungen, Germany
Single use syringe, 50 ml	Original Perfusor® syringe	B. Braun Melsungen AG, Melsungen, Germany
Three way stopcock	Discofix®	B. Braun Melsungen AG, Melsungen, Germany
Cannula 20G (0,9 mm x 40 mm) 24G (0,55 mm x 2 mm) 26G (0,45 mm x 25 mm) 30G (0,3 mm x 25 mm)	BD Microlance 3®	Becton Dickinson, Heidelberg, Germany

Table 4. Equipment

Equipment	Trade name/ Description	Company
Anesthesia chamber		Von Keutz Labortechnik, Reiskirchen, Germany
Cannula for flushing		Hugo Sachs Elektronik - Harvard Apparatus GmbH, March, Germany
Caliper	ABSOLUTE digimatic caliper	Mitutoyo Deutschland GmbH, Neuss, Germany
Catheter for carotid artery	Micro Cannulation System	FST GmbH, Heidelberg, Germany
Catheter for jugular vein	Hyman Mouse Pressure Catheter (14 cm)	NuMED Inc, Hopkinton, USA
Light source	KL-200 Fiber Optic Illuminator Light Source	Leica Microsystems, Nussloch, Germany
Pressure converter	Combitrans Monitoring Set Mod. II for arterial blood pressure measurement	B. Braun Melsungen AG, Melsungen, Germany
Pressure transducer	APT300	Hugo Sachs Elektronik - Harvard Apparatus GmbH, March, Germany
Retractors	Self-made from cannula 20G BD Microlance 3®	
Software	HSE-HA-PULMODYN W- for hemodynamic	Hugo Sachs Elektronik- Harvard Apparatus GmbH, March, Germany
Stereomicroscope	Leica MS5	Leica Microsystems, Nussloch, Germany
Stylet (for intubation)	Self-made from spinal cannula 20G (0.9 mm x 75 mm)	B. Braun Melsungen AG, Melsungen, Germany
Tracheal tube	Self-made from Vasofix® Safety 20G IV Catheter, shortened to 1.5cm	B. Braun Melsungen AG, Melsungen, Germany
Tripod	For holding syringes while flushing procedure	
Ventilator	MiniVent Type 845	Hugo Sachs Elektronik - Harvard Apparatus GmbH, March, Germany
Water bath		Von Keutz Labortechnik, Reiskirchen, Germany

Table 5. Surgical instruments, needles and sutures

Article Number	Company	Article description
11009-13	FST	Semken forceps: Curved, Serrated tips, 1.3 mm x 1 mm tip dimensions
11050-10	FST	Graefe forceps: Straight, Serrated tips, 0.8 mm x 0.7 mm tip dimensions
11052-10	FST	Graefe forceps: Curved, Serrated tips, 0.8 mm x 0.7 mm tip dimensions
11370-31	FST	Moria MC 31 Iris forceps: Curved, Serrated tips, 0.5 mm x 0.4 mm tip dimensions
12060-01	FST	Castroviejo Micro needle holder: Straight, Slightly blunted tips, with lock
14106-09	FST	Fine scissor: Straight, Large finger loops, Sharp tips
15003-08	FST	Vannas-Tübingen Spring scissor: Sharp, 5 mm cutting edge
15024-10	FST	Spring scissor: Straight, Sharp tips, 8 mm cutting edge
18025-10	FST	Suture Tying forceps: Straight, Smooth tips
304000	Becton Dickinson	BD Microlance™ 3 disposable hypodermic needles, 20G x 1½", 0.9 x 40 mm, yellow
303800	Becton Dickinson	BD Microlance™ 3 disposable hypodermic needles, 26G x ½", 0.45 x 13 mm, brown
30200	Becton Dickinson	BD Microlance™ 3 disposable hypodermic needles, 27G x ¾", 0.40 x 19 mm, grey
304000	Becton Dickinson	BD Microlance ™ 3 disposable hypodermic needles, 30G x ½", 0.30 x 13 mm, yellow
4268113S-01	B. Braun Melsungen	Vasofix® Safety 20G x 1¼", 1.1 x 33 mm, safety intravenous catheter with injection port
4268210S-01	B. Braun Melsungen	Vasofix® Safety 14G x 2", 2.2 x 50 mm, safety intravenous catheter with injection port
523735	Teleflex Medical	Weck hemoclip® Traditional, titanium ligating clip
8728810F	B. Braun Melsungen	Perfusor® syringe 50 ml
BC313R	Aesculap	Standard scissors – Blunt

EH7228	Ethicon	6-0 Prolene, C-1 13 mm 3/8c, polypropylene, blue monofil suture, non resorbable
FD562R	Aesculap	Aesculap® Biemer clip , vascular clip, jaw opening 5 mm, jaw length 9 mm, closing force 20-25G
	Edward Weck	Clip applier
	Ethicon	Surgical threads non-absorbable ETHIBOND EXCEL®, size 5-0

Table 6. Echocardiography devices

Device	**Trade name/ Description**	**Company**
Isoflurane vaporizer	VetEquip	KF Technology Rom, Italy
Rectal thermometer		Indus Instruments Houston, USA
Software	Vevo® LAB- for analyzing ultrasound and photoacoustic data	VisualSonics Inc. Toronto, Canada
Ultrasound platform	Vevo® 2100 -High-Frequency Imaging Platform	VisualSonics Inc. Toronto, Canada
Ultrasound gel	Aquagel®	Parker Laboratories Inc. Fairfield, USA

3.1.4. Histology and stereology

Table 7. Substances and solutions

Article	Trade name/ Description	Company
Acetic acid 100%		Merck KGaA, Darmstadt, Germany
4′,6-Diamidino-2-Phenylindole Dihydrochloride	fluorescent stain	Sigma-Aldrich, Steinheim, Germany
Ethanol 70%, 96%, 99.6% denatured with methyl-ethyl ketone		Fischer, Saarbrücken, Germany
Isolectin B4-TRITC	Lectin from Bandeiraea simplicifolia	Sigma-Aldrich, Steinheim, Germany
Isopropanol 99.8%		Fluka Chemie, Buchs, Switzerland
Mounting medium	Dako fluorescence mounting medium	Dako Deutschland GmbH, Hamburg, Germany
Mounting medium	Pertex®- Xylene-soluble	MEDITE GmbH, Burgdorf, Germany
Picric acid	aqueous, saturated	AppliChem GmbH, Darmstadt, Germany
Proteinase K		BIOZOL Diagnostica Vertrieb GmbH, Eching, Germany
Sirius Red F3B		Niepötter Labortechnik, Bürstadt, Deutschland
NaCl		Carl Roth GmbH, Karlsruhe, Germany
Trizma® base		Sigma-Aldrich, Steinheim, Germany
WGA lectin (-FITC)	Lectin from Triticum vulgaris conjugated to fluorescein isothiocyanate	Sigma-Aldrich, Steinheim, Germany
Xylol		Carl Roth GmbH, Krlsruhe, Germany

Table 8. Consumables

Article	Trade name/ Description	Company
Coverslip 24 x 36 mm		R. Langenbrinck, Emmendingen, Germany
Embedding paraffin	Paraplast Plus®	Sigma Aldrich, Steinheim, Germany
Microscope slide	Superfrost Plus®	R. Langenbrinck, Emmendingen, Germany
Microtome blade S35	Feather®	A. Hartenstein GmbH, Würzburg, Germany

Table 9. Devices and software

Article	Trade name/ Description	Company
Cooling plate	Leica EG1150C- Modular Tissue Embedding Center	Leica Microsystems, Nussloch, Germany
Digital camera	Leica DC300F- Digital camera systems for optimum image quality at low light intensity	Leica Microsystems, Nussloch, Germany
Drying chamber		Memmert GmbH & Co KG, Schwabach, Germany
Microtome	Leica RM2165- fully motorized rotary microtome	Leica Microsystems, Nussloch, Germany
Paraffin elongation bath	Leica HI 1210- Water bath for paraffin sections	Leica Microsystems, Nussloch, Germany
Paraffin embedding station	Leica EG1140H-Modular tissue embedding station	Leica Microsystems, Nussloch, Germany
Stereomicroscope	Leica DMLA Compound microscope	Leica Microsystems, Nussloch, Germany
Software	Stepanizer stereology tool for manual stereological assessment of digital images	www.stepanizer.com
Software	QWin V3- Processing and analysis software for quantitative microscopy	Leica Microsystems, Nussloch, Germany
Vacuum-tissue infiltration machine	Leica TP 1050ß Tissue processor	Leica Microsystems, Nussloch, Germany

3.1.5. Cardiomyocyte studies

Table 10. Substances, devices and instruments

Article	Trade Name/ Description	Company
Calcium chloride ($CaCl_2$)		Merck KGaA Darmstadt, Germany
Calcium chloride dehydrate ($CaCl_2$ x 2 H_2O)		Sigma-Aldrich, Seelze, Germany
(±)-Carnitine hydrochloride		Sigma-Aldrich, Seelze, Germany
Cell-edge detection system		SI Scientific Instruments GmbH, Munich, Germany
Centrifuge	Heraeus Megafuge 2.0R - Medium Bench Centrifuge	Heraeus Instruments GmbH, Hanau, Germany
Collagenase	Collagenase Type II, CLS II	Biochrom GmbH, Berlin, Germany
Creatine monohydrate		Sigma-Aldrich, Seelze, Germany
Cytosine- β-D-arabinofuranoside		Sigma-Aldrich, Seelze, Germany
Desiccator		Carl Roth GmbH & Co, Karlsruhe, Germany
DL-isopropyl arterenol		Serva Electrophoresis GmbH, Heidelberg, Germany
Falcon tube, 15 ml, 50 ml		Greiner bio-One, Frickenhausen,Germany
Fetal calf serum		PAA Laboratories GmbH, Cölbe, Germany
Fura-2-AM	Intracellular calcium indicator	Thermo Scientific, N. Meridian Road, USA
Glass pipette		Greiner bio-One, Frickenhausen,Germany
Glucose monohydrate		Merck KGaA, Darmstadt, Germany
HEPES (4-(2-hydroxyethyl)-1-piperazine ethane sulfonic acid)		Sigma-Aldrich, St. Louis, USA
Imaging system	IonOptix imaging system	IonOptix Corp., USA
Isoprenaline		Serva Electrophoresis GmbH, Heidelberg, Germany
Laminin		Roche Diagnostics GmbH, Mannheim, Germany

Line camera		SI Scientific Instruments GmbH, Munich, Germany
Magnesium sulphate ($MgSO_4$)		Merck KGaA, Darmstadt, Germany
Magnesium sulfate heptahydrate ($MgSO_4$ x 7 H_2O)		Merck KGaA, Darmstadt, Germany
Mechanical tissue chopper	McIlwain™	Hugo Sachs Elektronik - Harvard Apparatus GmbH, March, Germany
Medium 199 (w/o sodium bicarbonate, w L-glutamine, w Earle´s salts)	Medium M199 powder medium	Biochrom GmbH, Berlin, Germany
Microscope	Olympus IX-71-Inverted fluorescence microscope	Olympus, Hamburg, Germany
MitoSOX	Red mitochondrial superoxide indicator for live-cell imaging	Invitrogen, Carlsbad, USA
Monopotassium phosphate (KH_2PO_4)		Merck KGaA, Darmstadt, Germany
Nylon mesh		NeoLab, Heidelberg, Germany
Observation monitor		Philips GmbH, Herrsching, Germany
Oscilloscope	Goldstar OS-9020A	Gold Star Co, Seoul, Korea
Penicillin-Streptomycin (5,000 U/mL)		Gibco, Life Technologies GmbH, Darmstadt, Germany
Phase contrast microscope		Nikon, Düsseldorf, Germany
KCl		Merck KGaA, Darmstadt, Germany
Scalpel	Feather® Disposal Scalpel	Pfm Medical AG, Cologne, Germany
NaCl		Merck KGaA, Darmstadt, Germany
Sodium pyruvate		Sigma-Aldrich, Seelze, Germany
Tempol (4-Hydroxy-TEMPO)		Sigma-Aldrich, Seelze, Germany
Tweezer	Dumont tweezer (from Dumoxel, Nr. 7, bent, peak intensity 0.03 mm)	Dumont, Montignez, Switzerland
Taurine (2-aminoethanesulfonic acid)		Sigma-Aldrich, Seelze, Germany

3.1.6. Immunoblotting

Table 11. Substances, devices and instruments

Article	Trade name/ Description	Company
Absorbance reader	Elx808 Absorbance microplate reader	Bio Tek, Bad Friedrichshall, Germany
Autoradiography film		Kodak BioMax Light Film, Rochester, USA
Buffer	protein sample preparation buffer (Laemmli buffer: 25 mM Tris, 192 mM Glycin and 0.1% SDS)	Self-made
DC (detergent compatible) Protein Assay		Bio-Rad Laboratories, Munich, Germany
ECL (enhanced chemiluminescence) detection reagent	Amersham ECL Western Blotting Detection Reagent	GE Healthcare Life Sciences, Little Chalfont, UK
Gel	NuPAGE Bis-Tris Gel (10%), protein precast gel	Life Technologies, Darmstadt, Germany
Homogenizer	Precelly®24-Tissue homogenizer	PeqLab, Erlangen, Germany
phenylmethane sulfonyl fluoride (PMSF)		Sigma-Aldrich, St. Louis, USA
Protease inhibitor	cOmplete	Roche Applied Science, Penzberg, Germany
Protease inhibitor	Sodium-Orthovanadate	Sigma-Aldrich, St. Louis, USA
Protein standard	Precision Plus Protein™ Dual Color standards	Bio-Rad Laboratories, Munich, Germany
Scanner	CanoScan 5000F	Canon, Tokyo, Japan
sodium dodecyl sulphate (SDS)		Bio-Rad Laboratories, Munich, Germanysds
Software	AlphaEaseFC software	Alpha Innotec, San Leandro, USA
Western blot membrane	Nitrocellulose membrane	Pall Corporation, Pensacola, USA
Western blot membrane	PVDF membrane	ImmobilonTM-P, Millipore Corp, Bedford, USA

Table 12. Primary antibodies

Antibody	Cat. Nr.	Company
α-tubulin antibody (B-7)	sc-5286	Santa Cruz Biotechnology, Santa Cruz, USA
Glyceraldehyde 3-phosphate dehydrogenase (GAPDH)	CB1001	Calbiochem, Darmstadt, Germany
Mitofusin-2 (N-terminal)	M6319	Sigma Aldrich, Munich, Germany
NCX (H-300)	sc-32881	Santa Cruz Biotechnology, Santa Cruz, USA
Phospholamban (FL-52)	sc- 30142	Santa Cruz Biotechnology, Santa Cruz, USA
p-phospholamban (phospho S16 + T17)	ab62170	Abcam, Cambridge, UK
SERCA2 (C-20)	sc-8094	Santa Cruz Biotechnology, Santa Cruz, USA
UCP3	PA1-055	Thermo Fischer Scientific Inc, USA

Table 13. Secondary antibodies

Antibody	Cat. Nr.	Company
Goat anti-mouse IgG (H+L)	GAM-APHRP	Affinity Biologicals Inc, Canada
Peroxidase AffiniPure donkey anti-goat IgG (H+L)	705-035-147	Jackson ImmunoResearch, USA
Sheep anti-rabbit IgG (H+L)	SAR-APHRP	Affinity Biologicals Inc, Canada

3.1.7. Respiration measurements

Table 14. Substances and devices

Adenosine diphosphate (ADP)		Calbiochem, Darmstadt, Germany
Antimycin A		Sigma-Aldrich, Seelze, Germany
Adenosine 5′-triphosphate (ATP) disodium salt hydrate		Sigma-Aldrich, Seelze, Germany
Bovine serum albumin (BSA)	Essentially fatty acid free (fraction V)	Sigma-Aldrich, Seelze, Germany
Catalase	Lyophilized powder, 2,000-5,000 units/mg protein	Sigma-Alrdrich, Seelze, Germany
Dithiothreitol (DTT)	Reducing agent	Sigma-Alrdrich, Seelze, Germany
DL-Octanoyl-carnitine-hydrochloride		Tocris Bioscience, Bristol, UK
Ethylene glycol-bis (β-aminoethyl ether (EGTA)		Sigma-Aldrich, Seelze, Germany
Glutamate		Sigma-Aldrich, Seelze, Germany
HEPES (4-(2-hydroxyethyl)-1-piperazine ethanesulfonic acid)		Sigma-Aldrich, Seelze, Germany
Imidazole		Fluka (Sigma-Alrdrich), Steinheim, Germany
K-Lactobionate		Sigma-Alrdrich, Seelze, Germany
L-Glutamic acid		Sigma-Aldrich, Seelze, Germany
L-Malic acid		Sigma-Aldrich, Seelze, Germany
Magnesium sulphate ($MgSO_4$)		Merck KGaA, Darmstadt, Germany
4-Morpholineethanesulfonic acid (MES) hydrate		Sigma-Alrdrich, Seelze, Germany
Magnesium sulfate hexahydrate ($MgCl_2$ x 6 H_2O)		Sigma-Alrdrich, Seelze, Germany
Monopotassium phosphate (KH_2PO_4)		Merck KGaA, Darmstadt, Germany
Oxygraph-2K		Oroboros instruments, Innsbruck, Austria
Phosphocreatine disodium salt hydrate		Sigma-Alrdrich, Seelze, Germany
Pyruvic acid		Sigma-Aldrich Seelze, Germany
Saponin		Sigma-Aldrich Seelze, Germany

Software	DataLab software	Oroboros Instruments, Innsbruck, Austria
Succinate disodium salt, hexahydrate		Sigma-Aldrich Seelze, Germany
Sucrose		Carl Roth GmbH & Co, Karlsruhe, Germany
Taurine		Sigma-Alrdrich, Seelze, Germany

3.1.8. RNA analysis

Table 15. Substances, devices and instruments

iScript cDNA Synthesis Kit		Bio-Rad, Berkeley, USA
iTaq SYBR Green supermix with ROX		Bio-Rad, Hercules, USA
NanoDrop		PeqLab, Erlangen, Germany
Real-time PCR system	Mx3000P QPCR Systems	Agilent Technologies, Santa Clara, USA
Rneasy Micro kit		Qiagen, Hilden, Germany
SYBR Safe DNA Gel Stain		Invitrogen, Carlsbad, USA

3.2. Methods

3.2.1. PAB

This model induces a pulmonary stenosis and is used as a model of pressure overload-induced RVH and right heart failure [162]. Thin fragile walls of the pulmonary trunk are as limiting factor for making this model [53]. Furthermore, inability of the RV to withstand stress during pulmonary artery manipulation should be considered as a limiting factor [53].

3.2.1.1. Anesthesia

Prior to endotracheal intubation, the mice were placed inside a transparent chamber and a gas mixture of 3-4% isoflurane rest O_2 was introduced into the chamber to initiate anesthesia.

3.2.1.2. Endotracheal intubation

Intubation set up was prepared as described here. An endotracheal tube was prepared from the plastic part of a shortened intravenous catheter (20G x 1¼"). A blunted needle was inserted to this endotracheal tube in order to make it hard enough for the intubation process. The needle part was used to facilitate the introduction of the tracheal tube into the direction of the larynx and the epiglottis region. A surgical stereomicroscope (Leica MS5) was used for intubation and surgery procedures. A power light with easily bending horns was provided to illuminate the

larynx and operation region during intubation and operation. For intubation, the anesthetized mouse should be hanged on the blunted needle part of the intravenous catheter (14G x 2"). This needle part was connected to a 50 ml syringe, both were fixed on a retort stand using a clamp.

The anesthetized mouse was taken out of the anesthesia chamber and suspended on the intubation set up by its superior incisor teeth. The ventral area of neck was trans illuminated by light source to make the intubation procedure possible. A curved forceps was used to firmly hold the tongue and slightly move it upwards. The lower jaw was kept open by a straight forceps in a way that vocal cords and trachea could be visualized. Then, the tracheal tube was gently inserted into the trachea, passing the vocal cords. The needle part was removed out of the trachea while the plastic part was kept in place.

Application of a small drop of lidocaine on tip of the tracheal tube helped to reduce the gag reflex.

3.2.1.3. Ventilation

After intubation, the mouse was supine located on a plate. A modified Y shape connector linked the tracheal tube to a ventilator. Continuous inhalation of 1.5-2.5% isoflurane supplemented with 100% O_2 provided maintenance of anesthesia. The tidal volume was adjusted as 10 µl per gram of body weight (BW) and ventilation frequency to 150 strokes per minute. Positive end-expiratory pressure equal to 1 cm of water column was adjusted in order to avoid the collapse of alveoli during mechanical expiration.

3.2.1.4. Surgical procedure

Half an hour before starting the operation, a dose of analgesic buprenorphine hydrochloride (Temgesic®, 0.1 mg/kg) was given subcutaneously. The mouse was positioned and fixed by strands of surgical tapes (Durapore®) on its right side with the chest rotated and exposed to the operating person. The surgical plate was located in a shallow double layer plastic box. In this plastic box, the temperature could be kept around 40°C by circulating warm water in order to maintain the body temperature of the mouse. To prevent dryness of the cornea, sterile ophthalmic ointment (Bepanthen®) was applied on the eyes.

Before starting the surgery, onset of deep anesthesia was confirmed by loss of the pedal withdrawal reflex. A subcutaneous injection of 0.3 to 0.5 ml of NaCl solution was provided to compensate for the fluid loss during operation process. Chest area was completely shaved and disinfected with a mixture of 50% 2-propanol and 1% povidone-iodine solution

(Braunoderm®). The second intercostal space is the proper approach to obtain the target vessels. By using a surgical scalpel, a 1 cm long incision was made on the skin of the left thoracic region of the mouse. The chest muscles were kept back with a few self-made retractors prepared from dulled 20G needles. Intercostal muscles in the second intercostal space were incised and the incision was also kept open carefully with the help of self-made retractors. In order to visualize the main pulmonary trunk the pericardium was mobilized with the help of a forceps. Careful dissection of the pulmonary trunk from the ascending aorta and left atrium was carried out by a blunt forceps until making a tunnel under the pulmonary trunk. Afterwards, a small titanium hemoclip (Weck Hemoclip® Traditional) was positioned around the pulmonary artery to induce constriction with a width of 0.35 mm which corresponds to a stenosis of 65-70% [163]. Subsequently, interrupted suturing technique with non-absorbable sterile surgical suture (6-0 Prolene) was used to close the chest area around adjacent ribs. The same thread and continuous suturing technique was used for closure of the skin incision. The wound was treated with a mixture of 50% 2-propanol and 1% povidone-iodine solution. After surgery, the mice received 100 µl of a 5% glucose solution subcutaneously. After recovery from anesthesia and gaining back all reflexes, the animal was extubated. The mice were then transferred to a standard rodent cage with free access to food and water in a room of a temperature of 25°C for a few hours until transfer to the animal facility. Depending on clinical findings, one dose or a few doses of buprenorphine hydrochloride (0.1 mg/kg) was given subcutaneously.

Control mice were subjected to sham operation which includes all surgical steps except stenosis induction by means of the hemoclip.

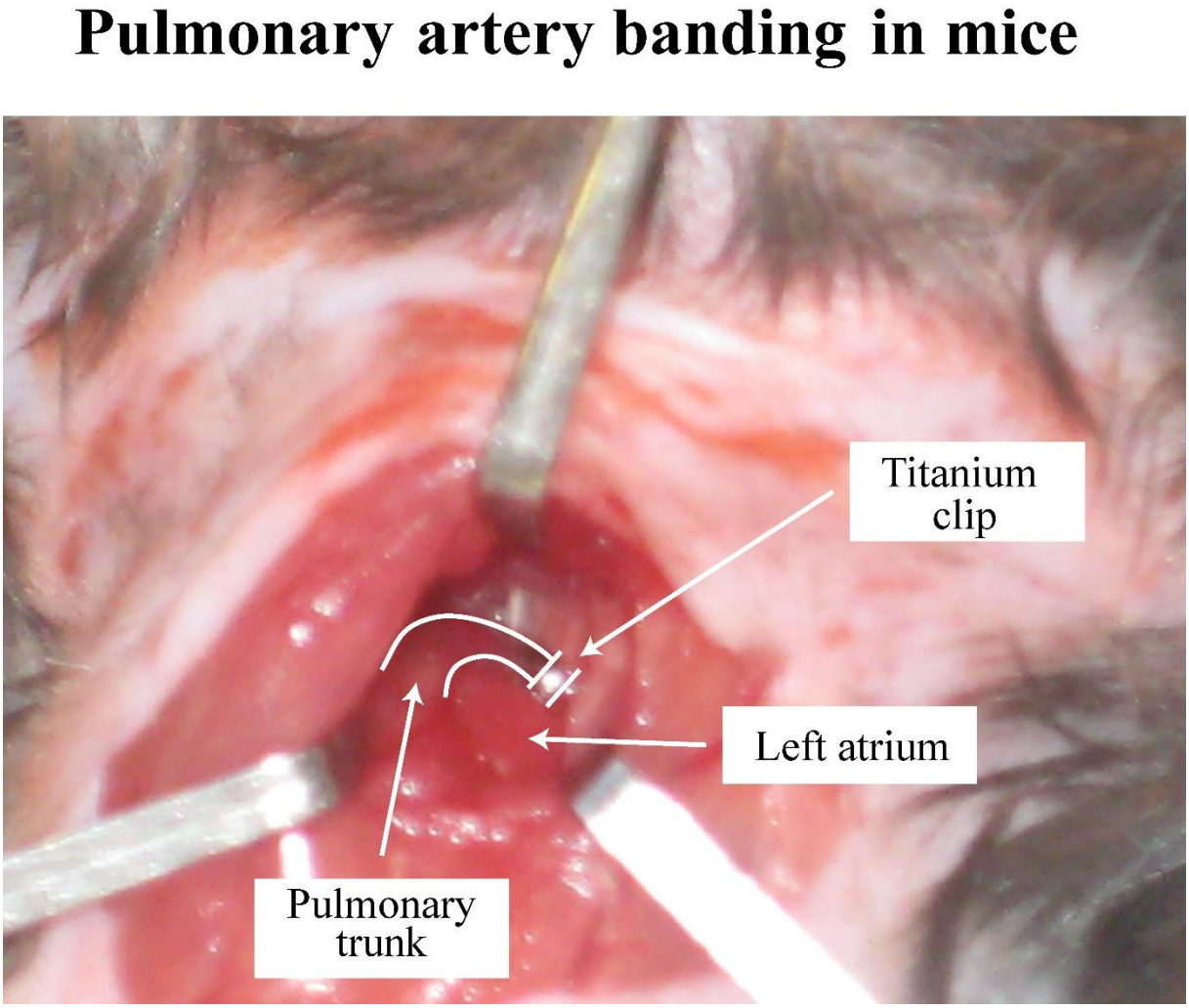

Figure 3. Pulmonary artery banding in mice

Careful dissection of the pulmonary trunk from the ascending aorta and left atrium provides enough space around the pulmonary trunk. Using a clip applier, a hemoclip will be positioned around the pulmonary artery to induce constriction with a width of 0.35 mm which corresponds to a stenosis of 65-70%**.**

3.2.1.5. Animal groups

Both UCP2 KO and C57BL/6J mice were divided into two groups receiving either PAB or sham operation. Experimental time period was 22 days together. In this model, only males were chosen for the experiment.

3.2.1.6. Experimental design

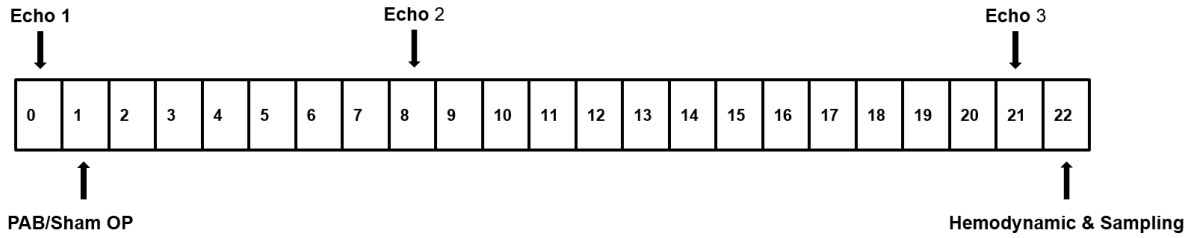

Echocardiography (Echo) was performed one day before the pulmonary artery banding (PAB)/Sham operation (OP) as well as 7 and 20 days after the OP. In vivo hemodynamic measurements and sampling were done 21 days after OP.

3.2.2. Echocardiography

3.2.2.1. Echocardiographic procedure

Echocardiography is a non-invasive and inexpensive imaging tool capable of repeatable evaluation of the cardiovascular system in laboratory animals. Echocardiography was performed using a commercially available Vevo® 2100 high-resolution imaging system equipped with a 40-MHz linear-array transducer. Echocardiography was performed one day before the operation as well as 7 and 20 days after the operation. To carry out the ultrasound examination, the animal was first placed in a transparent chamber for induction of anesthesia. 3-4% isoflurane in 100% O_2 at a flow rate of 2 L/min was used to initiate anesthesia. Afterwards, the animal was carefully placed in supine position on a heating plate with all limbs taped to ECG electrodes for HR monitoring. Subsequently, the snout was placed within a nose cone connected to the anesthetic system to maintain a steady-state sedation level by applying 1.0-1.5% isoflurane in 100% O_2. A single channel ECG was recorded during echocardiographic examination. A lubricated rectal thermometer was gently inserted inside the rectum to monitor body temperature and keep it at 37°C. In order to protect the cornea from drying, an ophthalmic ointment dexpanthenol (Bepanthen®) was applied to the eyes. The chest as well as cranial abdominal area were shaved to improve the quality of the echocardiographic images. Afterwards, the chest area was covered with a layer of a bubble free preheated ultrasound gel. Measurement of RV free wall thickness (RVWT) was done in the modified parasternal long-axis view. Right ventricular outflow tract (RVOT) dimension was measured from the RVOT view at the level of the aortic valve. For assessment of right ventricular performance, the RV myocardial performance index (MPI) and tricuspid annular plane systolic excursion (TAPSE) were measured. The apical four chamber view was used for evaluation of TPASE in a way that

the M-mode cursor was placed at the junction of the tricuspid valve plane and the RV free wall. Also in apical four chamber view, the MPI (also called Tei index) was measured by tissue doppler imaging (TDI) at the lateral part of the fibrous annulus of the tricuspid annulus. MPI was calculated as the sum of isovolumic contraction time (IVCT) and isovolumic relaxation time (IVRT) divided by the ejection time (ET). Aortic velocity time integral was evaluated from the suprasternal view. Pulse wave aortic doppler recordings as well as measurements of the proximal ascending aortic diameter were used for calculation of the aortic stroke volume (SVao).The aortic diameter as measured using M-mode echocardiography at the level of the proximal ascending aorta. The whole echocardiography procedure lasted 25-35 minutes. The echocardiographic parameters were calculated off-line using Vevo® LAB software.

After echocardiography assessment the mouse was carefully cleaned from ultrasound gel and transferred to a standard rodent cage with free access to food and water. The mouse was observed until it completely regained consciousness as well as motor skills. Afterwards, the mouse was brought back to the animal facility.

3.2.2.2. Echocardiographic parameters

Right ventricular internal diameter (RVID)

The RVID describes the inner diameter of the RV. It was appointed as the maximum distance of the free wall of the RV to the septum measured in the apical four-chamber view and in the unit of mm. With the help of RVID, one can determine the degree of dilation of the RV.

Myocardial performance index (MPI) or Tei index

The MPI/Tei index arises from the sum of IVCT and IVRT divided by ET. These values are measured by TDI. The MPI is thus a parameter which characterizes the global function (systolic and diastolic) of the RV. An increase in the MPI is equivalent to a deterioration of the global cardiac function: the ET decreases in proportion to the isovolumetric contraction and relaxation; therefore the window of time in which a blood transport is possible shortens. Even the Tei index is used as a prognostic factor in patients with PH [164, 165].

Cardiac output (CO)

The CO is the volume of blood that is pumped from the heart through the ascending aorta into the bloodstream in one minute. It is calculated from stroke volume (SV) x HR and is expressed in milliliters per minute. The SV can be determined during the echocardiography of the left ventricular outflow tract (LVOT). It is calculated from the diameter of LVOT and the integral

of the flow rate within the aorta during the systole called velocity time integral (VTI). As a formula CO will be calculated: CO = (LVOT x VTI) x HR. A decrease in cardiac-volume means a deterioration of the pumping function of the heart.

Tricuspid annular plane systolic excursion (TAPSE)

TAPSE is the distance traveled by the tricuspid ring between end-diastole and end-systole and is measured in mm. It is a parameter for the longitudinal function of the RV and is correlated with right ventricular ejection fraction (SV/end-diastolic volume x 100). A decrease of the value of TAPSE shows reduced contraction movement and thus restricting the systolic function of the RV. This parameter is used as an important prognostic factor for the survival of patients with PH [164, 165].

3.2.3. Hemodynamic assessment

3.2.3.1. Animal preparation

In vivo hemodynamic measurements were done 21 days after PAB operation. Approximately 15 minutes prior to measurement, the mouse was given heparin (1 IU/g) intraperitoneally. Afterwards, the pressure transducer and tubes of measurement system as well as the catheter were flushed with physiologic saline to be free of bubbles. The HSE-HA PULMODYN W software was started and the recording windows for RVSP and systemic arterial pressure (SAP) were opened. In our experimental work, combination of ketamine hydrochloride (Ketamin 10%®, 40 μg/g) and xylazine (Xylazin 2%, 0.6 μg/g) was administered intraperitoneally. This mixture has the advantage of rapid onset of anesthesia with an adequate duration of anesthesia. After reaching deep anesthesia defined as loss of pedal removal reflex, the mouse was placed on its supine position on a rubber pad located within a flat double-walled plastic shell. Circulation of 40°C water around the plastic shell helped to maintain physiological body temperature. A mixture of 50% 2-propanol and 1% povidone-iodine solution was applied on the neck region for disinfection. Subsequently, a 1-2 cm midline incision from below the mandible to the thoracic inlet was made on the skin and the mandibular glands and muscle layer beneath were pulled aside in a fine way until the trachea was visible. With the help of a curved forceps, a piece of thread was advanced under the trachea and a loose knot was made around it. After making a tiny incision in the trachea, a self-made tracheal tube was inserted and was afterwards connected to the ventilator. To fix the tracheal tube inside the trachea, the knot was tightly stretched. The respiratory frequency and tidal volume were adjusted to 150 breaths per

minute and 10 µl per gram BW subsequently. A column of water provided 1 cm water positive-end expiratory pressure in order to avoid collapse of the alveoli during mechanical inspiration.

3.2.3.2. Preparation of vessels

Fluid filled pressure transducer (APT300) made us capable of direct and continuous measurements of arterial pressure as well as ventricular systolic pressure. Pressures were recorded as analog signals through the fluid-filled pressure transducer. These analog signals were amplified and converted into digital signals with help of a transformer.

The left carotid artery was exposed carefully by dissecting omohyoid muscle longitudinally by means of a fine, curved and blunt forceps. Also, adjacent vagus nerve was gently separated and pulled aside. Using a thread, two ligatures were made around the exposed vessel. The cranial suture was ligated and totally tied up, while clamped using a tape to cranial region of plastic shell. The caudal ligature was presented loosely. Subsequently, the arterial catheter was positioned next to the artery and calibration value for SAP was set by adjusting the pressure transducer to zero mmHg. At entrance of chest, carotid artery was clamped by means of a vascular clip. Thereafter, a small incision (arteriotomy) proximal to the clip was made; catheter was inserted 2-3 mm in the direction of heart and was secured in place by total ligation of loose ligature. The vascular clip was removed and the catheter was pushed into the ascending aorta for about 11-12 mm until SAP would be recorded [166, 167].

The right jugular vein was exposed after dissecting from surrounding connective tissue. A loose tie on both cranial and caudal ends of the vessel was placed. After the venous catheter was located next to the jugular vein, calibration value for RVSP was set by adjusting the pressure transducer to zero mmHg. This step was followed by making an incision on jugular vein large enough to pass the catheter, between the two ligatures and introducing the catheter. Afterwards, the catheter was pushed approximately 5 mm into the vein and meanwhile the caudal ligature was quickly stretched downwards in order to prevent bleeding. The RVSP corresponds to an intact pulmonary artery systolic pressure [168].

The duration of recording for both SAP and RVSP was 10-15 min.

3.2.3.3. Plasma preparation

After moistening thorax and abdomen area with mixture of 50% 2-propanol and 1% povidone-iodine solution, an incision from umbilicus area towards manubrium sternum was made. Directly below the ribs, skin and muscle layers on both sides of the median line were cut to

open the abdominal cavity. Diaphragm was incised and rib cage was spread apart laterally; fixed with curved 24G needles. LV at apex was punctured by a 1ml self-made heparinized syringe and connected needle (24 G) to take blood. The blood was transferred to an eppendorf tube and centrifuged at 9,500 x g for 15 minutes. Plasma was pipetted into a screw cap tube, snap frozen in liquid nitrogen (-196°C) and stored at -80° C for further analysis.

3.2.3.4. Tissue processing

A piece of thread was directed under the pulmonary artery and aorta, making a loose ligature around them. This was followed by a small incision in RV, through which a cannula for flushing purpose was inserted into the pulmonary artery. The ligature was tightened and an opening was made in LV in order to drain rinsing solution. Afterwards, the lung was flushed from blood through the pulmonary artery with isotonic saline at a pressure of 22 cm water column. When the lung was empty of blood and looked white in appearance, right lung was removed, snap frozen in liquid nitrogen (-196°C) and stored at -80°C for later molecular biology analysis.

Heart was removed out of thoracic cavity. Both atria and surrounding tissues were cut. The heart was divided into RV and LV plus intra-ventricular septum (S). The ratio of RV to BW and the ratio of RV to LV+S weight were calculated to determine the degree of RVH. Weight of both ventricles was measured by laboratory scale.

Calculations are as below:

RV (mg) divided by LV plus S (mg)

RV (mg) divided by BW (g)

Half of the hearts were planned to be used for molecular biology analysis. These hearts were stored in screw cap tubes and snap frozen in liquid nitrogen (-196°C). Remaining hearts were planned to be used for histological analysis. For this purpose, the separated ventricles were stored in histology cassette and kept for 24 hours in formalin. On second day, the fixed ventricles were transferred from formalin into 0.1 M phosphate buffered saline (PBS) and kept for another 24 hours at 4°C. On day 3, they were transferred into 50% ethanol, and on day 4 into 70% ethanol until further use for the histological preparations.

In a few mice, thoracic cavity was opened and mice were euthanized by intracardiac administration of KCl solution (made isotonic with NaCl). This solution induced cardiac arrest at diastolic phase by eliminating the potassium concentration gradient and decreasing the resting membrane [169, 170]. Diastolic arrest of cardiomyocytes fixed all cells in round shape.

The taken hearts were split horizontally and transferred to formalin. The next steps were done as described previously for lung and heart tissues.

3.2.4. Histological Studies

3.2.4.1. Embedding and slide preparation

Draining step of ventricles already stored in 70% ethanol was done overnight in automated tissue processing machine through a routine program. Subsequently, tissues were embedded using embedding machine and cooled down on a cooling plate until the wax blocks containing tissues could be drove out of their molds. The histological section was made into 3 µm thick slices, mounted on slides and dried on a hotplate. Sections were incubated at 37°C in heating cabinet.

3.2.4.2. Collagen content measurement

3.2.4.2.1. Sirius Red staining of histology slides

To prepare PicroSirius Red solution 0.2 g Sirius Red was dissolved in 200 ml of picric acid and the resulting solution was filtered through a filter paper to remove solid particles. After that, the pH was adjusted to 2.0.

Sirius Red staining of slides was done according the following protocol:

Table 16. Sirius Red staining protocol

Dewaxing and rehydration of paraffin-embedded tissue sections	
60 Minutes	Incubation at 58°C
3 ×10 Minutes	Xylol
2 × 5 Minutes	Ethanol absolute 99.6%
5 Minutes	Ethanol 96%
5 Minutes	Ethanol 70%
Staining protocol	
60 Minutes	0.1% Picro SiriusRed solution (protected from light)
3 × 2 Minutes	1% acetic acid (for washing)
Rinse off	Aqua dest.
Dehydration of paraffin-embedded tissue sections	
1 Minute	Aqua dest.
2 × 2 Minutes	Ethanol 96%
2 × 5 Minutes	Isopropyl alcohol
3 × 5 Minutes	Xylol
Mounting with Pertex®	

3.2.4.2.2. Analysis of interstitial and perivascular collagen content

The percentage of collagen fibers in the right ventricles was measured using Leica QWin standard analysing software, developed by the Leica Macro Company. The longitudinal sections of the RV were stained with Sirius Red which binds to collagen fibers and gives a red color. The surrounding tissue containing no collagen, was shown in yellow. The sections were counted in meander-shaped movements with the help of 630-fold magnification. Every second image in every second row was analysed so that totally 40-90 pictures were taken depending on the size of the RV. The percentage of collagen content per unit area was transferred. Stained vessels were excluded from the measurement. The total collagen content of the RV was calculated as the average of all taken images.

3.2.4.3. Ratio of capillaries to cardiomyocytes

3.2.4.3.1. Wheat germ agglutinin (WGA) / Isolectin B4-immunostaining

20-fold concentrated tris buffered saline (TBS) was prepared as below:

-122 g Trizma base

-180 g NaCl

-Aqua dest. up to 1000 ml

The solution was diluted 20 times as 1-fold buffer and the pH adjusted to 8.4.

Preparation of slides for immunostaining was done according the following protocol:

Table 17. Immunostaining protocol of wheat germ agglutinin / isolectin B4

Dewaxing and rehydration of paraffin-embedded tissue sections as table 16	
2 × 5 Minutes	TBS (for washing)
30 Minutes	Proteinase K digestion
3 × 5 Minutes	TBS (for washing)
2 Minutes	BSA 10% (for blocking)
4 × 5 Minutes	TBS (for washing)
Overnight	WGA-FITC (1:150) IB4-TRITC (1:150) in TBS DAPI (1:200)
6 × 20 Minutes	TBS (for washing)
1 Minute	Aqua dest.
7 Minutes	In heating incubator at 37°C (for drying)
Mounting with Dako mounting medium	

3.2.4.3.2. Analysis of the number of cardiomyocytes and capillaries

For this purpose, horizontal 3µm-thick sections of RV with a distance of 20 µm were made and tagged with isolectin. This reaction is based on coupling of fluorescent dyes to most of proteins in plants through highly specific bonds to sugar residues which are called lectins. WGA was conjugated with the fluorescent dye fluorescein isothiocyanate (FITC) and would bind to N-acetyl-D-glucosamine residues. At 488 nm excitation wavelength, the cell wall of cardiac myocytes depicted green color assigned to his dye. The isolectin B4 (IB4) from the African plant Griffonia simplicifolia was labelled with tetramethylrhodamine-5 (-6) isothiocyanate (TRITC) and coupled to α-galactosyl residues. It bound to endothelial cells and the capillaries appeared in red at an excitation wavelength of 594 nm. Nuclei were stained with 4 ', 6-diamidino-2-phenylindole dihydrochloride (DAPI), which binds to DNA as intercalating agent. DAPI appears in blue under ultraviolet light. From each section 9-15 images were taken at 630 × magnification and with the help of Leica QWin software. These pictures were then evaluated using the Stepanizer stereology tool, a software freely available on the internet (http://www.stepanizer.com). After counting the number of cardiomyocytes and capillaries, the ratio of whole capillaries to cardiomyocytes per ventricle were analysed. In another calculation, the number of capillaries per of cardiomyocytes were analysed.

3.2.5. Isolation of ventricular cardiomyocytes

The following solutions and buffers were used for preparation of cardiomyocytes:

Calcium stock solution:

$CaCl_2$ 100 mM

Perfusion medium (pH 7.4, carbogen gassed for rat cardiomyocytes):

Glucose monohydrate	11 mM
HEPES	25 mM
KCl	2.6 mM
KH_2PO_4	1.2 mM
$MgSO_4$ x 7 H_2O	1.2 mM
NaCl	110 mM

Collagenase buffer:

$CaCl_2$ 100 mM	12.5 µl
Collagenase	25 mg
Perfusion medium	5 ml

The following solutions were used for culturing isolated cardiomyocytes:

CCT medium (sterile filtered, pH 7.4):

Medium 199	2 packages
Distilled water	10 L
HEPES	36 g
Creatine	5 mM
DL-carnitine	5 mM
Taurine	5 mM
Cytosine- β-D-arabinofuranoside	10 mg

Pre-incubation Medium:

CCT medium (sterile filtrated, pH 7.4)	x ml
FCS (rat cardiomyocytes)/ Laminin (mouse cardiomyocytes)	4% (v/v) / 10 µl/1 ml
Penicillin/ Streptomycin	2% (v/v)

CCT culture medium (for rat cardiomyocytes):

CCT Medium (sterile filtrated, pH 7.4)	x ml
Penicillin/ Streptomycin	2% (v/v)

Zappel buffer (sterile filtered, pH 7.4, for mouse cardiomyocytes):

NaCl	118 mM
KH_2PO_4	1.2 mM
KCl	4.7 mM
Glucose	5 mM
$MgSO_4$	0.8 mM
HEPES	10 mM
$CaCl_2$ dihydrate	2.5 mM
Sodium pyruvate	1.9 mM

3.2.5.1. Isolation of rat ventricular cardiomyocytes

Ventricular heart muscle cells were isolated by Langendorff perfusion system from approximately 200 gram adult male Wistar rats as described previously [171].

3.2.5.1.1. Perfusion system preparation, heart preparation and perfusion

The Langendorff perfusion system was rinsed with 200 ml distilled water. The water was replaced with 20 ml perfusion buffer and allowed to circulate for 5 minutes inside the system. The system was filled with 80 ml bubble-free perfusion buffer, gassed continuously with carbogen (5% CO_2-95% O_2) to obtain a constant pH value and let the system warm up to 37°C.

Rats were put in a small desiccator and deeply anesthetized using 4-5% Isoflurane. After cervical dislocation, chest area was opened, heart and lung were excised and transferred to a petri dish filled with ice cold physiological saline solution. After removal of lung, oesophagus, trachea, thymus, and aorta excluding the aortic arch; the heart was mounted from the aortic part over the cannula provided in Langendorff perfusion apparatus, by help of two forceps. The aorta was fixed with crocodile clip. It is important to do these steps quickly. It was checked that the cannula was not inserted too deeply into the heart; otherwise perfusion via the coronary vessels would be no longer possible. Before fixing the heart with thread to perfusion system, the valve was opened in order to see if vessels are well perfused. After fixing the heart by making a ligature around cannula, perfusion was started in non-recirculating mode with perfusion buffer at flow rate of one drop per second for 5 minutes, this allowed blood to wash away. Approximately 35 ml perfusion buffer was used for this step. Then, the collagenase buffer was added to the top reservoir of the system while a collecting funnel wrapped with parafilm was located under the heart. Perfusion was continued in recirculating mode for 25 minutes more.

3.2.5.1.2. Heart enzymatic digestion and separation of cardiomyocytes from other cell types

When the heart looks smooth, perfusion can be stopped which also depends on the activity and quality of collagenase enzyme. After separation of ventricle from atrium and aorta, ventricle was transferred to another petri dish in order to cut it into small pieces at slitting width of 0.7 mm, using a tissue chopper. Chopping was continued using two scalpels on a watch glass. Chopped tissue was then transferred into a tube containing re-circulated buffer and gently triturated using a sterile 5 ml pipette twice per minute for 5 minutes at 37°C. The cell suspension was filtered through a nylon mesh (mesh size 200 µm) into a falcon and centrifuged at 400 rpm for 3 minutes. The pellet contained myocytes while the supernatant contained small non-myocytes such as endothelial cells and fibroblasts. The pellet was resuspended in perfusate in which the final concentration of $CaCl_2$ was increased stepwise to 200 µM and 400 µM. The resuspended pellet was centrifuged at 400 rpm for 2 minutes. Later on, the pellet was

resuspended in 12 ml of final concentration of 1 mM $CaCl_2$ in perfusion buffer and spinned at 300 rpm for 1 minute. After removing supernatant, the pellet was resuspended in CCT medium containing 2% penicillin/streptomycin and cells were transferred to culture dishes pre-coated overnight with 4% (v/v) fetal calf serum; modified accordingly [172].

3.2.5.1.3. Culture of cardiomyocytes

After 1-2 hour(s) being kept in pre-incubation medium in 37°C under CO_2 free condition, cells were ready to be washed once with CCT culture medium to remove damaged cells and leave a homogenous population of myocytes. This results in 90% living, intact, rod-shaped cells. Finally, cells were plated at a density of 4-7 × 10^4 elongated cells per 35 mm culture dish. In each culture a density of rod-shaped, living cells ranged from 40 to 60% was plated; modified accordingly [172].

3.2.5.2. Isolation of mouse ventricular cardiomyocytes

Ventricular heart muscle cells were isolated from male C57BL/6J and $UCP2^{-/-}$ mice by Langendorff perfusion system as described previously [171, 173].

Perfusion system preparation, heart preparation and perfusion for mouse cardiomyocytes are similar to what already for rat ventricular isolation is explained. The perfusion buffer for mouse cardiomyocyte should not be carbogen gassed, while the rat cardiomyocytes were carbogen gassed.

When the heart looks smooth enough, perfusion can be stopped. Ventricle was separated from atrium and aorta, chopped into small pieces at width of 0.7 mm with a tissue chopper and later on with scalpels. Chopped tissue was transferred into a tube containing circulated buffer and gently triturated with a 5 ml pipette twice per minute for 5 minutes at 37°C. After filtering through a nylon mesh, suspension was centrifuged at 400 rpm for 1 minute. Pellet was resuspended in perfusion medium including 100 mM $CaCl_2$ (final concentration 125 µM) and centrifuged at 300 rpm for 1 minute. Perfusion medium containing 100 mM $CaCl_2$ with final concentrations of 250 µM and 500 µM were used to resuspend the pellets every time after centrifugation was done at 300 rpm for 1 minute. After last centrifugation, pellet was resuspended in final concentration of 1 mM of $CaCl_2$ in perfusion medium and the pellet which contains rod-shaped cardiomyocytes was plated on culture dishes pre-coated with laminin (1g/l) which allows pre-treatment of cells shortly (1 hour) before cell plating. Cells can be washed with CCT medium to remove round and non- attached cells at least 1 hour after being kept in 37°C incubator without CO_2, modified accordingly [172].

3.2.6. Cell treatment

Only cells showing rod-shape morphology and having no signs of sarcolemmal blebs were used for analysis. In this project, cells were studied either under basal condition or after application of 10 nM isoprenaline (ISO). ISO was used to stimulate β-adrenoceptors and all treated and un-treated cells were incubated at 37°C, with 95% humidity after ISO was added to them.

3.2.7. Electrical stimulation of cardiomyocytes

A self-made plate cover with 2 rectangular electrodes was used for this purpose.

It was made such that when the cover was placed on the plate, electrodes were situated into the cell culture medium. Electrodes were connected to the electrical stimulator which generated stimulation. Cells were stimulated via these two electrodes with biphasic electrical stimuli composed of two equal but opposite rectangular 50-V stimuli of 5 millisecond duration. Cardiomyocytes were exposed to 2 Hz stimulation. Contraction signals were recorded every 15 seconds. The mean of these 4 measurements were used to define the mean shortening of each cell.

The culture dishes containing cells in CCT culture medium (for rat myocytes) or Zappel buffer (for mouse myocytes) were mounted on the stage of an inverted microscope. As already explained, a special self-made cap with 2 rectangular AgCl electrodes was used for cardiomyocytes stimulation. Cell culture dishes were covered by this cap and cells were stimulated with biphasic electrical stimuli. Each cell was stimulated at 2 Hz for 1 minute. Every 15 seconds, cell shortening, contraction velocity and relaxation velocity were measured using a line camera. The average of all four measurements per every minute and their mean provided us a frequency to define the contractility of the specific cell. Length of the cell was measured at a rate of 500 Hz via a line camera. Cells were allowed to contract at room temperature and analysed using a cell-edge detection system. Cells not responding to the given specific stimulation frequency were excluded from analysis.

3.2.8. Determination of parameters of cell contraction

Indexes of mechanical properties of isolated cardiomyocytes were assessed by cell-edge detection system which measures changes in myocyte length in response to electrical stimulation. The system consists of a phase contrast microscope, black and white linear camera and a software. This system enables cell visualizing, detection of its edges and calculation of the cell length differences between systole and diastole.

For observing cell contraction with line camera, the camera was moved to provide the image zone, where it was able to cover cell edges in horizontal position. At the end, it would provide a picture with the cell going to be screened. Additionally, the culture dish was moved so that the specific experimental cell was exactly in the proper place in the image zone. The line camera was turned until both cell ends were covered by the line camera. The image from the line camera was converted into electrical signals, presented on an oscillograph. The deflection time on the horizontal amplifier was adjusted to 0.1 millisecond per cm and the vertical amplifier was regulated at 5 millivolts per division (mV/div). Detectable brightness by line camera was represented on the oscillograph as varying y-deflections. Amplitudes representing cell borders could be identified by their horizontal movement. It was thus possible to observe the cell contraction on the oscillograph.

The oscillograph operated as a bi-channel oscillograph while against the second channel a strong stress or tension of the interface rested. The oscillograph presented a horizontal line at a certain height on the screen, if it was readable. This line was shown at the height of zero when non-readable. The video camera was used for recording phase-contrast micrographs. The contractions of every single cell were determined from consecutive frozen video frames magnifying the cell's picture up to 500-fold on a video monitor screen. The software program CELL provided a graph on the basis of cell length at different times, representing a curve of cell length dependent on time. Cell shortening was recognized by the software at the beginning of cell contraction. Cells were constantly paced, and four contractions were recorded every 15 seconds. The average of these recordings was used as one data point.

1: Load free cell shortening expressed as shortening amplitude normalized to diastolic cell lengths (dL/L%)

2: The contraction velocity expressed as micrometres per second

3: The relaxation velocity expressed as micrometres per second

3.2.9. Calcium transient quantification

3.2.9.1. Cell preparation

In order to explain the potential effects of a calcium receptor stimulation on cell shortening, cytosolic Ca^{2+} concentration was measured with fluorescent indicator Fura-2-AM as already described [174]. Isolated cardiomyocytes were loaded with Fura-2-AM at 37°C. Cells attached to FCS-coated glass coverslips were incubated for 30 minutes in medium 199 with

acetoxymethyl ester of Fura-2 (2.5 µM). Later on, cells were washed twice with medium 199 for 30 minutes to allow hydrolysis of the acetoxymethyl esters within the cell. The fluorescence signal from dye-loaded cells was 20-30 times higher than background fluorescence.

3.2.9.2. Measurement of intracellular Ca^{2+}

Cell loaded coverslips were introduced into a gas-tight, temperature-controlled (37°C) and transparent perfusion chamber while positioned in the light path of an Olympus IX71 inverted microscope. Fura-2-AM was excited with 340 and 380 nm wavelengths at 37°C. Emission of light at 500-520 nm wavelength from an area of 10 x10 µm within a single fluorescent cell was collected by an imaging system (ION Optix Corp, MA). The data were analysed as the ratio of light emitted at 340 nm to 380 nm wavelengths. Calcium transients of beating cells were determined while cells were submitted to field stimulation at 1 Hz.

3.2.10. Superoxide release assessment by MitoSOX

MitoSOX Red mitochondrial superoxide indicator was used to detect mitochondrial superoxide as described previously for PASMCs [175]. Cardiomyocytes seeded on coverslips were incubated at 37°C without CO_2 in 5 µM MitoSOX diluted in Zappel buffer for 15 minutes. Once in the mitochondria, MitoSOX Red reagent was oxidized by superoxide and exhibited red fluorescence. MitoSOX was excited at 510 nm and fluorescence was measured at 580 nm. Emission waves were recorded at 510 nm. ISO (10 nM) was added after 2 minutes of steady state.

3.2.11. Tempol studies with rat cardiomyocytes

After cell isolation as described above, rat cardiomyocytes were cultured and incubated with tempol (4-hydroxy-2, 2, 6, 6-tetramethylpiperidin-1-oxyl) with final concentration of 1 mM per dish for 24 hours. The cells were washed with CCT medium and used for further investigations.

3.2.12. Protein extraction

Protein extracts were prepared from isolated cardiomyocytes as well as RV and LV tissues.

3.2.12.1. Protein extraction from cardiomyocytes

Isolated cardiomyocytes were scrapped off from culture dishes and treated with lysis buffer as already explained [176]. Protein concentration was measured and protein samples were used for western blot or stored at -20°C.

Lysis buffer (1ml, pH 6.7):

DDT (500 nM)	100 µl
Lysis buffer (self-made, 50 mM Tris/HCL)	885 µl
Phosphatase inhibitor	10 µl
Protease inhibitor	5 µl

After preparation, add 2% (w/v) sodium dodecyl sulphate (SDS) to it under the safety hood.

3.2.12.2. Protein extraction from heart tissues

RV and LV tissues were transferred into 2 ml screw cap tubes containing 150 µl ice cold lysis buffer and ceramic beads. The tissues were homogenized for 2 x 30 seconds in the Precellys®24 homogenizer. The samples were then centrifuged for 5 minutes at 10,000 rpm, allowed to stay on ice for 15 minutes and the supernatant was then transferred into eppendorf tubes. Protein concentration was measured and protein samples were used for western blot or stored at -20°C.

Lysis buffer:

Ripa buffer	1000 µl
cOmplete	40 µl
PMSF (100 mM)	1 µl
Sodium-Orthovanadate (200 mM)	5 µl

3.2.13. Protein concentration measurement

The determination of protein concentration was performed using the DC protein assay, according to the principle of the Lowry assay which is a colorimetric assay. Prior to concentration measurement, samples were diluted 1:10 in Ripa buffer. As a reference, a standard series (from 0.2 mg/ml to 1.6 mg/ml) was prepared from bovine serum albumin (BSA). Pure Ripa buffer was used as blank. 5 µl of the blank, the standards and protein samples were pipetted into a 96-well microplate. This was followed by adding 25 µl of a reagent mixture (1 ml of reagent A plus 20 µl reagent S) and 200 µl of reagent B to each well. Afterwards, the plate was placed in the absorbance reader Elx808 which measured the absorbance at 750 nm. The standard curve and protein concentration were calculated by means of software.

3.2.14. Western blot analysis

3.2.14.1. Western blot with extracted cells

20 µl of Laemmli buffer was added to 100 µl of each sample. After heating for 5 minutes at 95°C, protein samples were loaded on NuPAGE Bis-Tris precast gels (Life Technologies) and transferred onto nitrocellulose membrane. Nonspecific proteins were blocked with 2% (w/v) BSA and membranes were subsequently incubated at room temperature for 2 hours with primary antibodies including anti-SERCA2(C-20) (1:200), anti-phospholamban (FL-52) (1:200), anti-p-phospholamban (phospho S16 + T17) (1:1000), anti-NCX (H-300) (1:200), anti-Mitofusin-2 (N-terminal) (1:200) detecting calcium handling proteins and anti–GAPDH (1:4000) as loading control. After washing thrice with TBS-T buffer (Tris Buffered Saline + 0.1% Tween-20), the membranes were re-incubated with secondary, horseradish peroxidise (HRP) conjugated antibodies including donkey anti-goat (1:2000), goat anti-mouse (1:2000), and sheep anti-rabbit (1:2000) for 1 hour at room temperature. After washing thrice, detection of bands' density was done by enhanced chemiluminescence (ECL).

3.2.14.2. Western blot with extracted tissues

Anti-UCP3 (1:1000) and anti-α-tubulin (loading control, 1:5000) antibodies were used to detect the specific proteins in tissue homogenates. Extracted protein from RV and LV was separated on a 12% SDS polyacrylamide gel and subsequently after separation were transferred onto a 0.45 µm polyvinylidene fluoride (PVDF) membrane using semidry transferring equipment. The unspecific sites were blocked with 6% non-fat dry milk in TBS-T buffer for 1 hour and the membranes were incubated overnight at 4°C with respective antibodies in 6% non-fat dry milk. Every incubation was preceded by five washes with TBS-T buffer for 10 minutes. The anti-rabbit and anti-mouse IgG secondary antibody coupled to HRP were used in dilution of 1:5000 for 1 hour at room temperature. Every incubation step was preceded by three washes with TBS-T buffer for 10 minutes. Visualisation of immunoreactive sites was carried out by ECL. Membranes were exposed to autoradiography film. Scanning of the films was done by a scanner. AlphaEaseFC software was applied for analysis of the bands as well as densitometry.

3.2.15. Determination of mitochondrial respiration in permeabilized muscle fibers

3.2.15.1. Heart preparation

After opening chest cavity heart was excised, aorta and pulmonary artery were removed, and later RV and LV were separated. Heart was cut lengthwise into small pieces and transferred

into a petri dish containing ice cold medium called BIOPS. BIOPS is a relaxing and biopsy preservation solution which biopsies can be kept in it for several hours at 0°C. Using a pair of sharp forceps all connecting tissues were removed while the petridish containing biopsies was kept still on ice. A period of approximately five minutes was enough in order to prepare samples by partially teasing apart and stretching them out, while tissues still remained connected in a mesh-like framework. A change from red to pale colour was observed in the separated fibers bundles, which would be a marker for evaluating the degree of separation.

BIOPS medium (pH 7.1):

ATP	5.77 mM
Ca-EGTA buffer	10 mM
DTT	0.5 mM
Free calcium	0.1 µM
Imidazole	20 mM
K-MES	50 mM
$MgCl_2$ x 6 H_2O	6.56 mM
phosphocreatine	15 mM
Taurine	20 mM

3.2.15.2. Tissue permeabilization

The whole process as already explained causes partial permeabilization of heart fiber bundles, but full permeabilization is possible through incubation in BIOPS medium containing saponin. The fiber bundles were quickly transferred into petri dish containing 2 ml of ice cold BIOPS including 20 µl saponin stock solution (5 mg/ml, final concentration 50 µg/ml). The petridish was put on a shaker in cold room (on ice) for 30 minutes, letting gentle agitation. Samples were quickly transferred from permeabilization solution into 2 ml of Mir06 which is a mitochondrial respiration medium. Shaking was continued by gentle agitation in cold room (on ice) for 10 minutes more.

Mir06 solution (pH 7.1):

BSA	1 g/l
Catalase	280 u/ml
EGTA	0.5 mM
HEPES	20 mM
KH_2PO_4	10 mM
K-lactobionate	60 mM
$MgCl_2$ x 6 H_2O	3 mM
Sucrose	110 mM
Taurine	20 mM

3.2.15.3. Wet weight of sample

Before using the samples for measurement in Oxygraph-2K chamber, several loosely connected fiber bundles were taken with a sharp pair of forceps (having angular tip), were placed for a few seconds on a filter paper and meanwhile the liquid from the tip of forceps was wiped with another filter paper. Afterwards, the samples were put immediately onto a small plastic surface on the table of a scale which was already tared. The wet weight was measured and the samples were immediately transferred into a petri dish containing ice cold Mir06.

3.2.15.4. Respiration measurement with Oxygraph-2K

The oxygen sensors were calibrated in Mir06 medium at 37°C while stoppers were partially inserted in order to avoid raw signals reaching the limiting value of 10V at high experimental oxygen concentrations. Respiration should be measured at 37°C in Mir06 medium which provides optimal protection of mitochondrial function. The samples were transferred into Oxygraph-2k chamber and immersed with a straight forceps into the medium stirring inside the chamber. The chamber was closed for the oxygen concentration signal to be stable. After that, a standard substrate- inhibitor protocol using pyruvate (5 mM), ADP (1 mM), glutamate (10 mM) and malate (4 mM), octanoylcarnitine (0.25 mM), succinate (10 mM) and antimycin A (5 µM) was applied for measurement of respiration in Mir06 medium. Oxygen consumption was calculated from the recorded data as the time derivative of the oxygen content in the chamber corrected to antimycin A, using DatLab software (Oroboros Instruments, Innsbruck, Austria).

3.2.16. RNA extraction, cDNA synthesis and Real-Time PCR

The isolation of ribonucleic acid (RNA) from tissue homogenates of the RV and LV was performed using the RNeasy Micro Kit (Qiagen). Following the RNA isolation, the concentration of RNA was determined spectrophotometrically by NanoDrop. The concentration measurement was accompanied by measurement of purity of extracted RNA. The preparation of complementary DNA (cDNA) was carried out by reverse transcription using the iScript cDNA Synthesis Kit (Bio-Rad). In each case 500 ng RNA was measured according to protocol "1 × (25°C, 5 min), 1 × (42°C, 30 min) followed by 1 × (85°C, 5 min)" reverse transcription. Afterwards, the total cDNA obtained from the RV and LV tissues was used to carry out real-time polymerase chain reaction (PCR) using a master mix for reverse transcription (RT) PCR (iTaq SYBR Green supermix with ROX, Bio-Rad) and Mx3000P QPCR System (Agilent Technologies). Hypoxanthine phosphoribosyltransferase (HPRT) was

used as housekeeping gene. Oligonucleotide sequence of mouse UCP3 and HPRT primers were designed as:

Species	Primer	Orientation	Sequence	Accessing number
Mouse	UCP3	Sense	TGCTGAAGATGGTGGCTCA	NM_009464
		Antisense	CCCGCAGTACCTGGACTTTC	
Mouse	HPRT	Sense	GCTGACCTGCTGGATTAC	NM_013556
		Antisense	TTGGGGCTGTACTGCTTA	

Abbreviations: UCP3: Uncoupling protein 3; HPRT: Hypoxanthine phosphoribosyltransferase

Used reaction condition was 1× (95°C, 10 min) followed by 45 × (95°C, 5 s; 60°C, 5 s, 72°C, 10 s) and the extension phase was done at 72°C. Measurement of each gene was carried out as duplicate. Confirmation of the desired products formation was done by dissociation curves. Running the products on an agarose gel with SYBR Safe DNA Gel Stain (Invitrogen) was the next step. The calculation of ΔCt values was done by subtracting the Ct values of the target gene from the endogenous control [ΔCt = Ct (endogenous control) – Ct (target)].

4. Results

Data are presented as individual value plots or summary data plots. All data are expressed as mean ± standard error of mean (SEM). The different experimental groups were statistically analysed by either Student's t-test or two-way ANOVA and Bonferroni post-hoc test in case of multiple comparisons. Values of $p < 0.05$ were considered as statistically significant.

4.1. Effect of PAB on the right heart of UCP2$^{-/-}$ mice

4.1.1. Increased RVSP in C57BL/6J (WT) and UCP2$^{-/-}$ mice subjected to PAB

Hemodynamic measurements showed that PAB caused an increase in RVSP of comparable degree in WT and UCP2$^{-/-}$ mice, while it had no effect on SAP three weeks after operation.

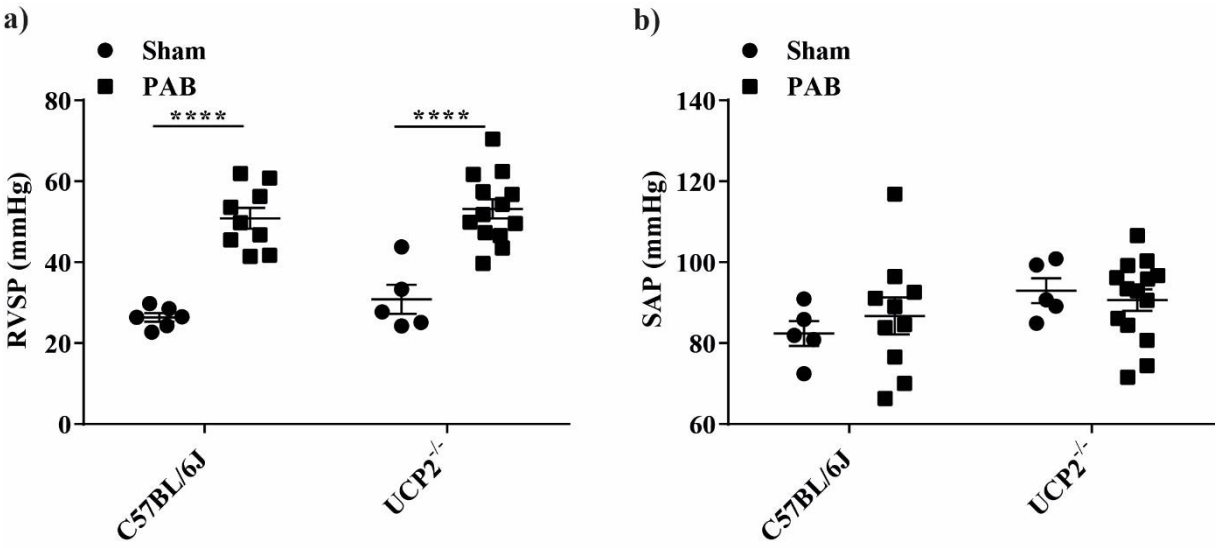

Figure 4. Hemodynamic measurements three weeks after PAB operation

a) Right ventricular systolic pressure (RVSP) in C57BL/6J and UCP2 $^{-/-}$ mice (n = 5-13 each group) and b) systemic arterial pressure (SAP) in C57BL/6J and UCP2 $^{-/-}$ mice (n =5-14 each group) in a model of right ventricular hypertrophy (RVH) induced by pulmonary artery banding (PAB) three weeks after surgery. Control mice were subjected to sham surgery. Values are depicted as mean ± SEM; ****P < 0.0001 compared to corresponding sham mice; analysis by two way ANOVA.

4.1.2. Right heart hypertrophy in C57BL/6J (WT) and UCP2$^{-/-}$ mice subjected to PAB

The ratio of the RV mass to BW and the ratio of RV mass to LV plus S mass was increased in both WT and UCP2 $^{-/-}$ mice to a similar degree after PAB. These data demonstrated induction of right heart hypertrophy in WT and UCP2$^{-/-}$ mice after PAB operation.

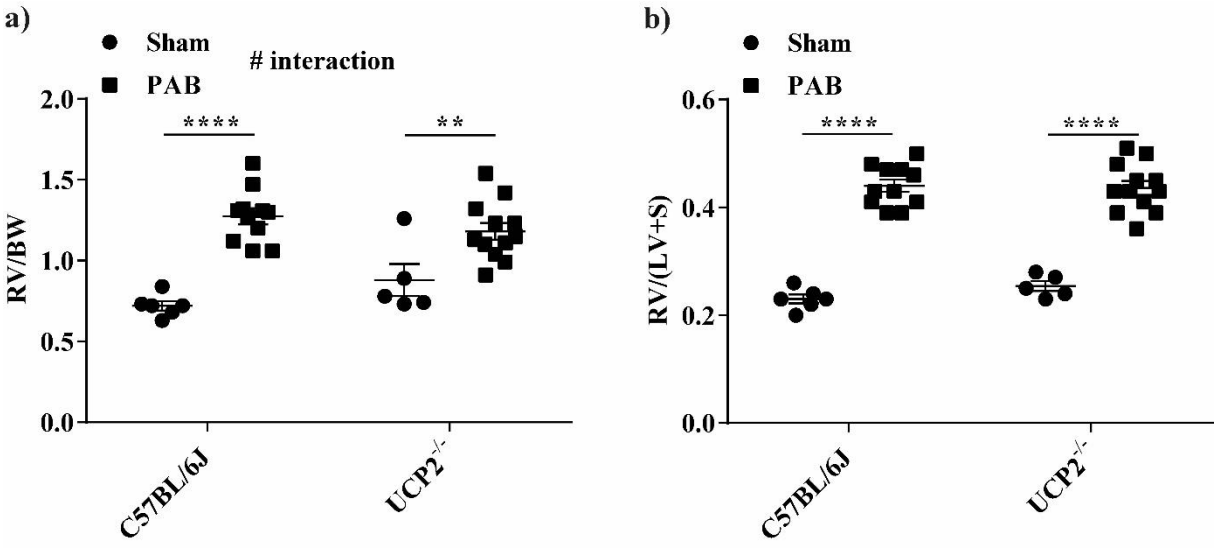

Figure 5. Right heart hypertrophy three weeks after PAB

a) Ratio of right ventricular mass to body weight (RV/BW) and b) ratio of right ventricular mass to left ventricular plus septal mass (RV/LV+S) as measures for right heart hypertrophy in C57BL/6J and UCP2$^{-/-}$ mice (n = 5-12 each group) three weeks after PAB operation. Control mice were subjected to sham operation. Values are depicted as mean ± SEM; **P < 0.01 and ****P < 0.0001 compared to corresponding sham mice; interaction between genotype and treatment was statistically significant for RV/BW; analysis by two way ANOVA.

4.1.3. Preserved RV function in UCP2$^{-/-}$ mice and deteriorated RV function in C57BL/6J (WT) mice after PAB

CO and TAPSE, representing global and right ventricular systolic function, respectively, were lower in UCP2$^{-/-}$ mice which received sham operation compared to sham-operated WT mice (Figures 6a,b). These parameters both decreased in WT mice after PAB compared to corresponding sham mice while they were preserved in UCP2$^{-/-}$ mice (Figures 6a,b). Global right heart function, determined as myocardial performance index (MPI or Tei index) was reduced in sham-operated UCP2$^{-/-}$ mice compared to WT mice subjected to sham operation (Figure 6c). After PAB, this parameter was deteriorated in WT mice whereas it remained preserved in UCP2$^{-/-}$ mice (Figure 6c). In sham-operated mice, RVWT was slightly higher in UCP2$^{-/-}$ mice compared to WT mice (Figures 6d, 7). The sham-operated UCP2$^{-/-}$ mice showed no difference in RVID in comparison to WT mice subjected to sham operation (Figures 6e, 7). PAB resulted in right ventricular dilatation as evidenced by an increase in RVID. However, in UCP2$^{-/-}$ mice, RVID was increased to a significantly lesser extent compared to WT mice. In summary, the echocardiographic data showed preserved right ventricular function in UCP2$^{-/-}$ mice after PAB operation in contrast to WT mice.

* Echocardiography was performed by Dr. Baktybek Kojonazarov and Dr. Akylbek Sydykov, ECCPS, Justus-Liebig-University, Giessen

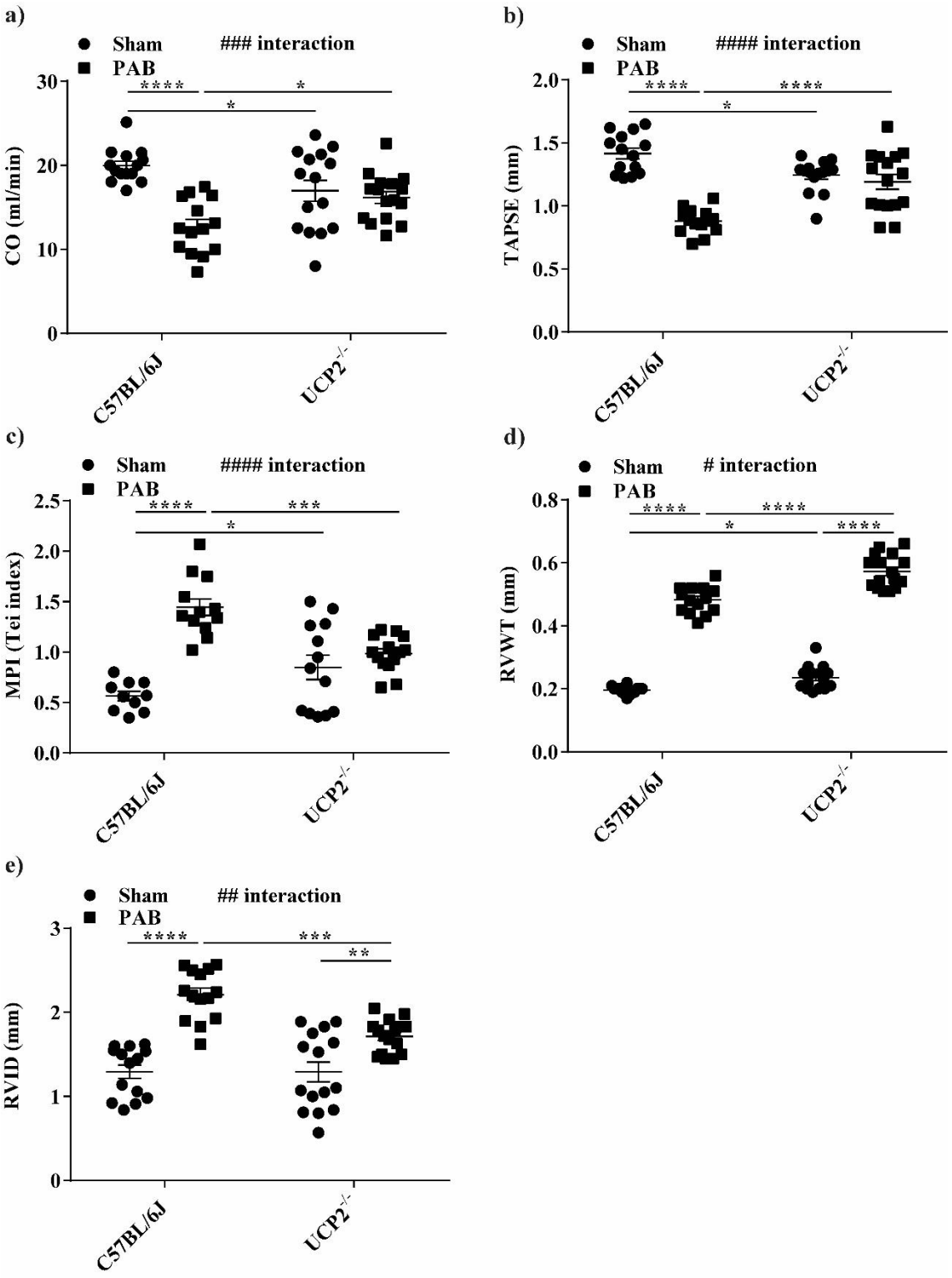

Figure 6. Echocardiographic findings three weeks after PAB

a) Cardiac output (CO), b) tricuspid annular plane systolic excursion (TAPSE), c) myocardial performance index (MPI), d) right ventricular wall thickness (RVWT), e) right ventricular internal diameter (RVID) in C57BL/6J and UCP2$^{-/-}$ mice (n = 4-16 each group) three weeks after PAB or sham operation. Values are depicted as mean ± SEM; *p < 0.05, **p < 0.01, ***p < 0.001 and ****P < 0.0001; interaction between genotype and treatment was statistically significant for CO, TAPSE, MPI, RVWT and RVID; analysis by two way ANOVA.

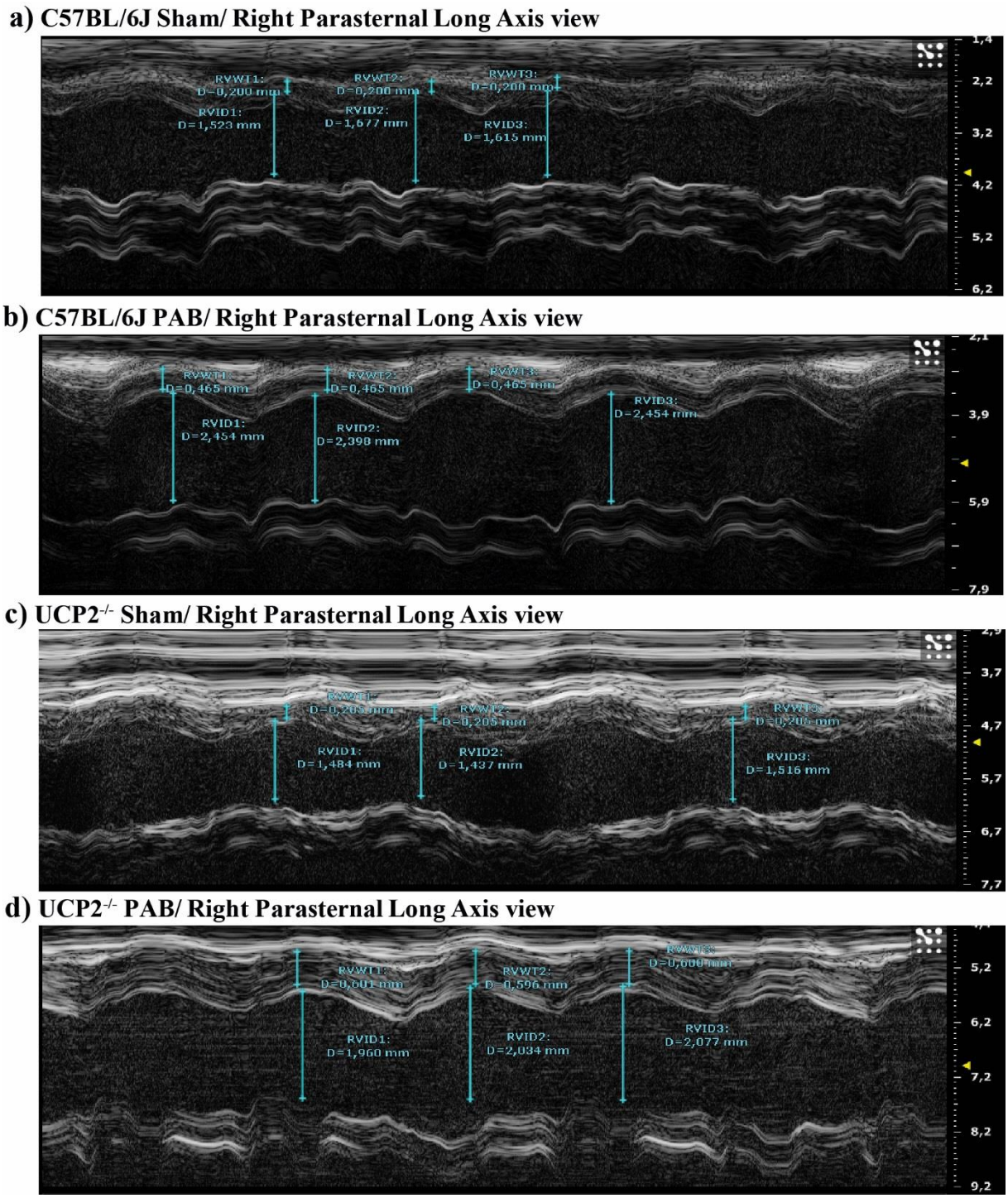

Figure 7. Representative echocardiographic images three weeks after PAB
Echocardiographic images demonstrating right ventricular wall thickness (RVWT) and right ventricular internal diameter (RVID) in the right parasternal long axis view in a) C57BL/6J sham, b) C57BL/6J PAB, c) UCP2 $^{-/-}$ sham and d) UCP2 $^{-/-}$ PAB mice three weeks after PAB or sham operation.

4.1.4. Increased RV collagen content in C57BL/6J (WT) and UCP2$^{-/-}$ mice after PAB

In order to find out the degree of fibrosis in the RV, the relation of the area of collagen fibers to the total area of the RV section was determined. Both WT and UCP2$^{-/-}$ mice showed increased myocardial fibrosis in the RV after PAB as evidenced by an increase in the RV content of collagen fibers (Figures 8a,b). Interestingly, the collagen content in PAB-operated UCP2$^{-/-}$ mice was significantly higher than in PAB-operated WT mice.

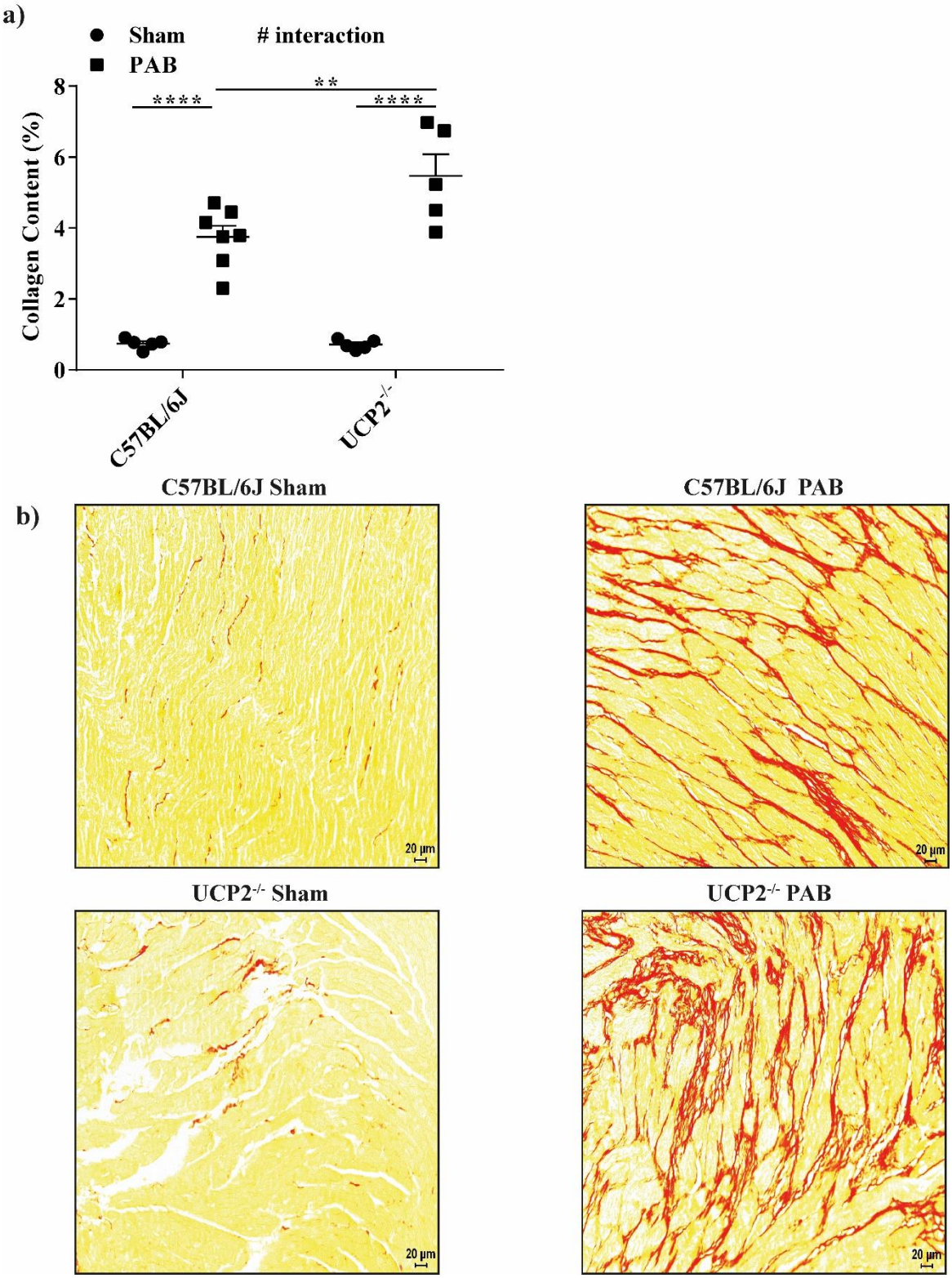

Figure 8. Percent of collagen content in the RV three weeks after PAB

a) Percent of collagen content (n = 5-7 each group) and b) histologic sections of the right ventricle after staining with PicroSirius Red showing the right ventricular fibrosis in C57BL/6J and UCP2$^{-/-}$ three weeks after PAB or sham operation. The surrounding non-collagen-containing tissue is shown in yellow. Values are depicted as mean ± SEM; **p < 0.01 and ****P < 0.0001; interaction between genotype and treatment was statistically significant for collagen content; analysis by two way ANOVA.

4.1.5. Preserved degree of capillarization in C57BL/6J (WT) and UCP2$^{-/-}$ mice subjected to PAB

The ratio of the number of capillaries to cardiomyocytes (Cap/Card) provides information on the oxygen supply of the heart muscle. Although the WT and UCP2$^{-/-}$ mice showed no difference in Cap/Card ratio after PAB (Figures 9a,c), the ratio of capillaries to CSA of cardiomyocyte was decreased in both groups of mice (Figure 9b). However, there was no difference between WT and UCP2$^{-/-}$ mice.

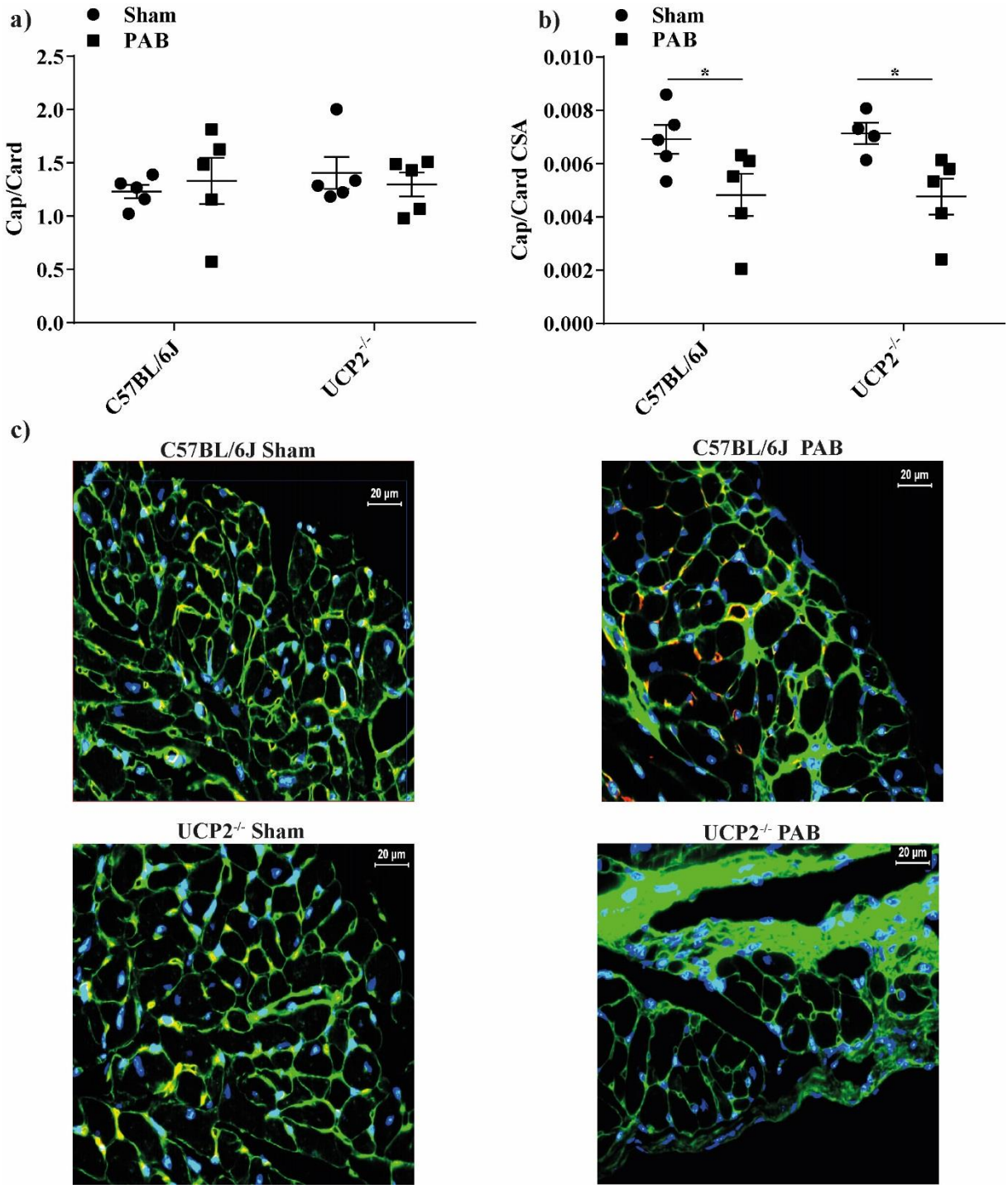

Figure 9. Ratio of capillaries to cardiomyocytes in the RV three weeks after PAB

a) The ratio of capillaries to cardiomyocytes (Cap/Card), b) number of capillaries per cross sectional area (CSA) of cardiomyocytes in right ventricular sections (n = 5 each group), and c) representative picture showing right ventricular capillarization in C57BL/6J and UCP2$^{-/-}$ mice three weeks after PAB or sham operation. Values are depicted as mean ± SEM; *p < 0.05; analysis by two way ANOVA.

4.2. Effects of PAB on isolated cardiomyocytes

4.2.1. Functional studies in isolated cardiomyocytes

4.2.1.1. Improved fractional shortening of cardiomyocytes isolated from the RV of UCP2$^{-/-}$ mice after PAB compared to C57BL/6J (WT) mice

Cardiomyocytes isolated from the RV of both WT and UCP2$^{-/-}$ mice showed an enhanced ratio of cell length shortening to diastolic cell length expressed as percent (dL/L%) under non-stimulated conditions three weeks after PAB operation compared to sham mice (Figures 10a,c). However, in non-stimulated cardiomyocytes isolated from the RV of UCP2$^{-/-}$ mice subjected to PAB operation, factional cell shortening showed a higher value compared to cardiomyocytes from WT mice after PAB operation (Figures 10a,c). Stimulation with ISO led to a significant increase in fractional cell shortening of cardiomyocytes isolated from the RV of UCP2$^{-/-}$ mice after PAB operation, but not of cardiomyocytes from WT mice subjected to PAB operation (Figures 10b,c). Stimulated cardiomyocytes from the RV of WT mice showed no significant difference in fractional shortening to those from UCP2$^{-/-}$ mice after sham or PAB operation (Figures 10b,c). Interestingly, we found increased cell shortening in the cardiomyocytes isolated from the LV of sham- and PAB-operated UCP2$^{-/-}$ mice compared to WT mice under non-stimulated conditions (Figures 11a,c). However, after stimulation with ISO, cell shortening was increased in the cardiac myocytes from the LV of PAB-operated mice, but did not differ between genotypes (Figures 11b,c).

* Cell shortening measurement was performed by AG Schlüter, Physiology Institute, Justus-Liebig-University, Giessen

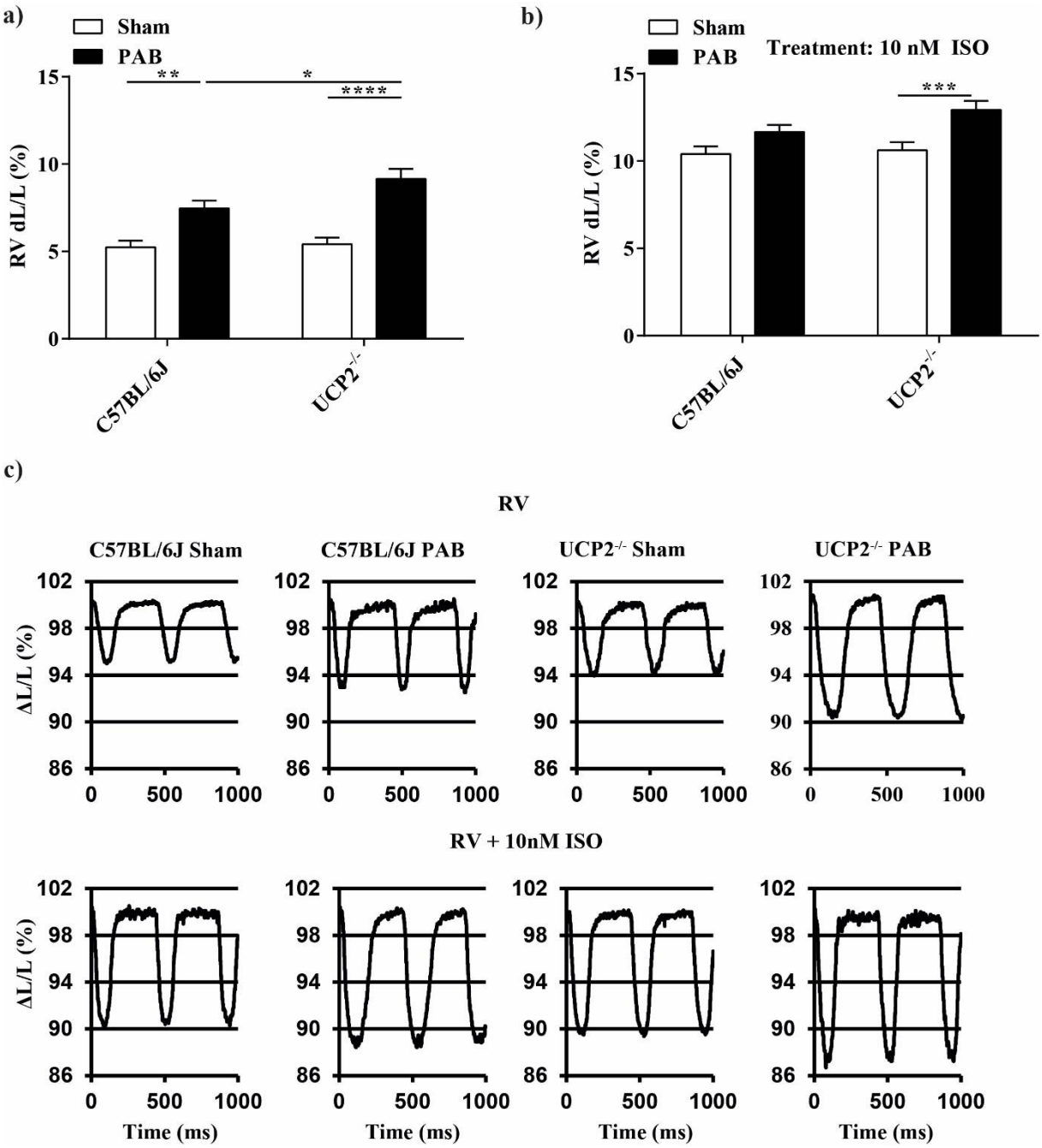

Figure 10. Fractional shortening of cardiomyocytes isolated from the RV three weeks after PAB

Ratio of cell length shortening to diastolic cell length (dL/L) as percent (%) in cardiomyocytes isolated from the right ventricle (RV) a) under basal condition (n = 29-35 cells each group, from at least 3 isolations), and b) after stimulation with 10 nmol/L isoprenaline (ISO) (n = 36 cells each group, from at least 3 isolations). c) Single-cell recordings of cell shortening at 2 Hz stimulation. Values are depicted as mean ± SEM; *p < 0.05, **p < 0.01, ***p < 0.001 and ****p < 0.0001; analysis by two way ANOVA.

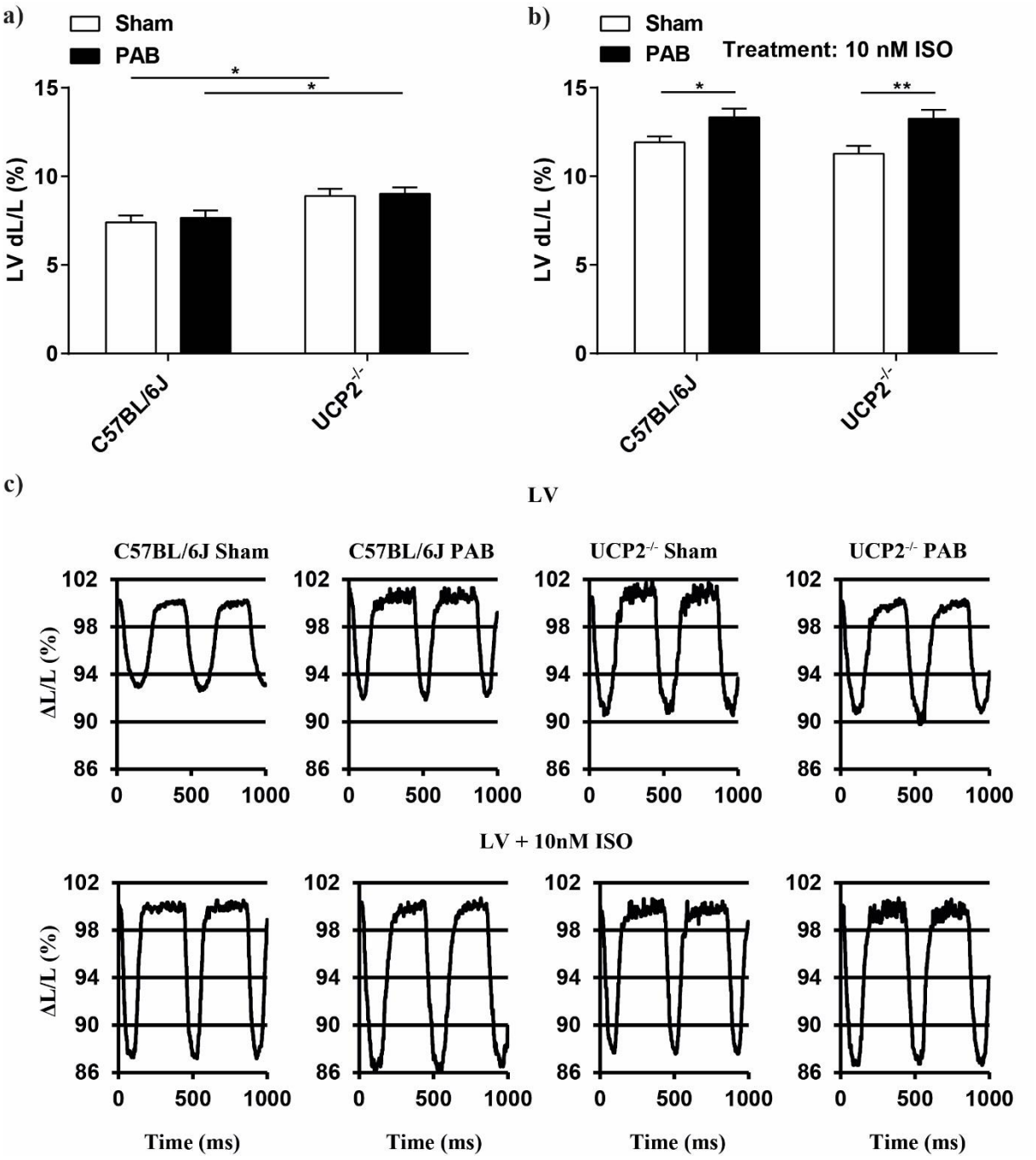

Figure 11. Fractional shortening of cardiomyocytes isolated from the LV three weeks after PAB

Ratio of cell length shortening to diastolic cell length (dL/L) as percent (%) in cardiomyocytes isolated from the left ventricle (LV) a) under basal condition (n = 52 cells each group, from at least 3 isolations), and b) after stimulation with 10 nmol/L isoprenaline (ISO) (n = 52 cells each group, from at least 3 isolations). c) Single-cell recordings of cell shortening at 2 Hz stimulation. Values are depicted as mean ± SEM; *p< 0.05 and **p < 0.01; analysis by two way ANOVA.

4.2.1.2. Improved contraction velocity of cardiomyocytes isolated from the RV of UCP2$^{-/-}$ mice after PAB compared to C57BL/6J (WT) mice

Under non-stimulated conditions, the RV cardiomyocyte contraction velocity was increased after PAB compared to sham in both strains (Figure 12a), albeit to a higher degree in RV cardiomyocytes from UCP2$^{-/-}$ mice after stimulation with ISO (Figure 12b). PAB had no significant effect on the contraction velocity of unstimulated LV cardiomyocyte (Figure 12c). Stimulation with ISO resulted in a higher increase of the contraction velocity of UCP2$^{-/-}$ sham cardiomyocytes compared to sham WT cardiomyocytes isolated from LV (Figure 12d). In contrast, the ISO-stimulated contraction velocity was significantly increased in cardiomyocytes from PAB-operated WT mice and not in those from PAB-operated UCP2$^{-/-}$ mice (Figure 12d).

* Contraction velocity measurement was performed by AG Schlüter, Physiology Institute, Justus-Liebig-University, Giessen

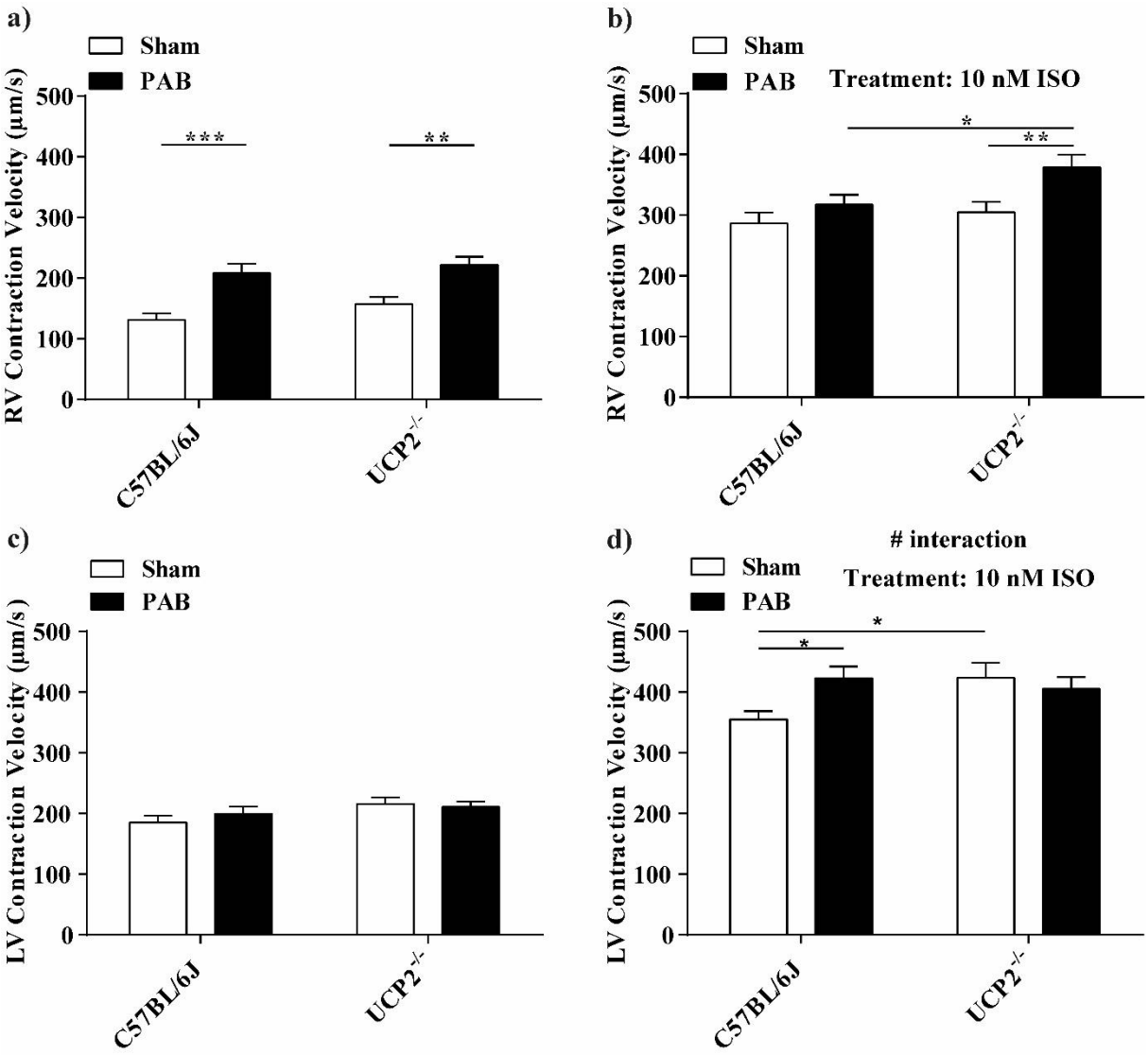

Figure 12. Contraction velocity of cardiomyocytes isolated from the RV and LV three weeks after PAB

Contraction velocity in a) cardiomyocytes isolated from the right ventricle (RV) under basal conditions (n = 30-36 cells each group, from at least 3 isolations), b) cardiomyocytes isolated from the RV after stimulation with 10 nmol/L isoprenaline (ISO) (n = 36 cells each group, from at least 3 isolations), c) cardiomyocyte isolated from the left ventricle (LV) under basal condition (n = 52 cells each group, from at least 3 isolations), and d) cardiomyocytes isolated from the LV after stimulation with 10 nmol/L ISO (n = 52 cells each group, from at least 3 isolations). Values are depicted as mean ± SEM; *p < 0.05, **p < 0.01 and ***p < 0.001; interaction between genotype and treatment was statistically significant for LV Contraction Velocity after stimulation with ISO; analysis by two way ANOVA.

4.2.1.3. Improved relaxation velocity of cardiomyocytes isolated from the RV of UCP2$^{-/-}$ mice after PAB compared to C57BL/6J (WT) mice

Under non-stimulated conditions, RV cardiomyocyte relaxation velocity was increased after PAB compared to sham in both strains (Figure 13a), albeit to a higher degree in RV cardiomyocytes from UCP2$^{-/-}$ mice after stimulation with ISO (Figure 13b). The relaxation velocity of non-stimulated LV cardiomyocytes showed no significant effect of PAB (Figure 13c), In contrast, the ISO-stimulated relaxation velocity was significantly increased in cardiomyocytes from sham-operated UCP2$^{-/-}$ mice compared to those from sham-operated WT mice (Figure 13d).

* Relaxation velocity measurement was performed by AG Schlüter, Physiology Institute, Justus-Liebig-University, Giessen

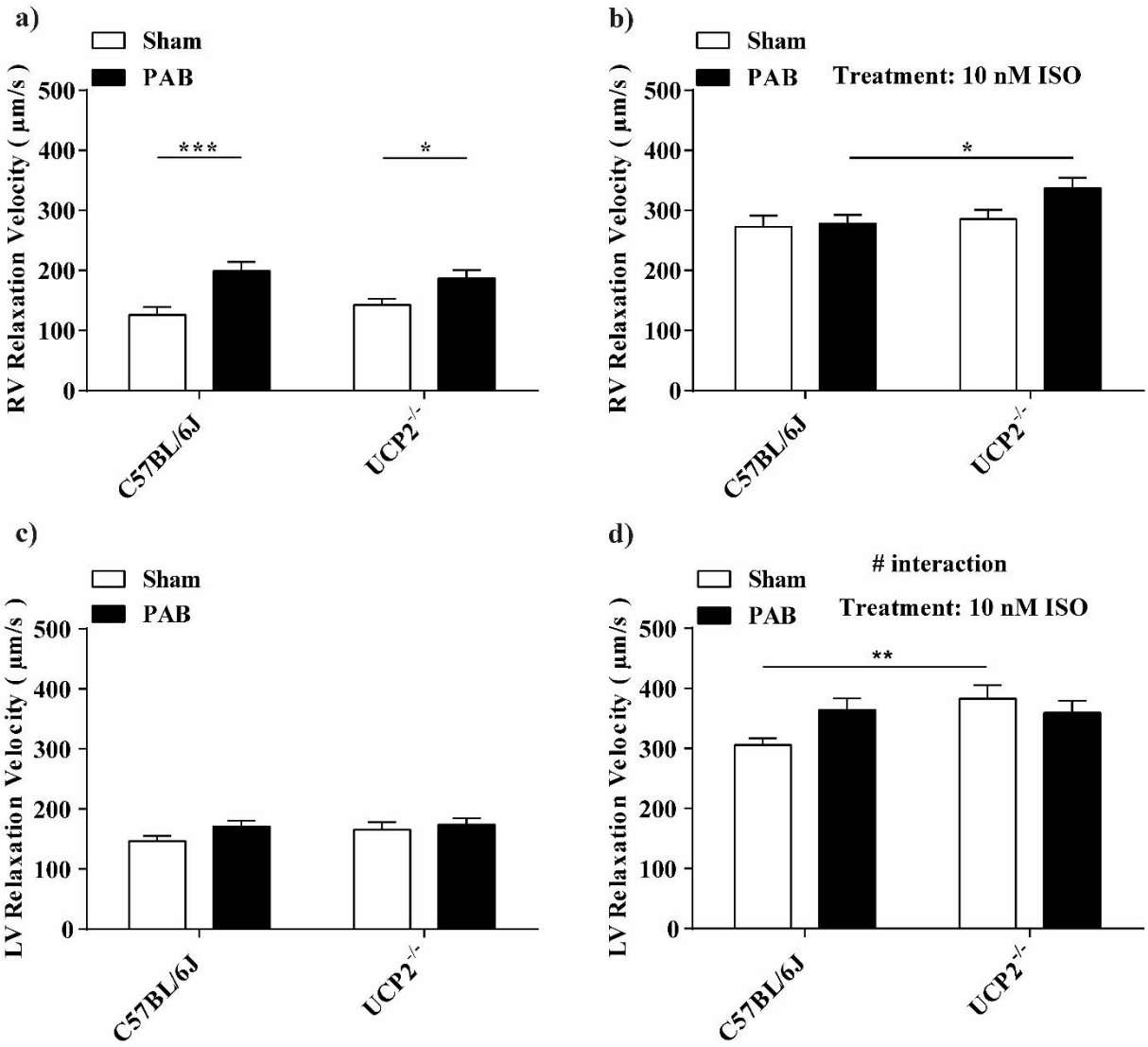

Figure 13. Relaxation velocity of cardiomyocytes isolated from the RV and LV three weeks after PAB

Relaxation velocity in a) cardiomyocyte isolated from the right ventricle (RV) under basal conditions (n = 30-36 cells each group, from at least 3 isolations), b) cardiomyocytes isolated from the RV after stimulation with 10 nmol/L isoprenaline (ISO) (n = 36 cells each group, from at least 3 isolations), c) cardiomyocyte isolated from the left ventricle (LV) under basal condition (n = 52 cells each group, from at least 3 isolations), and d) cardiomyocytes isolated from the LV after stimulation with 10 nmol/L ISO (n = 52 cells each group, from at least 3 isolations). Values are depicted as mean ± SEM; *p < 0.05, **p < 0.01 and ***p < 0.001; interaction between genotype and treatment was statistically significant for LV Relaxation Velocity after stimulation with ISO; analysis by two way ANOVA.

4.2.2. Calcium dynamics in isolated cardiomyocytes

4.2.2.1. Increased calcium transients in cardiomyocytes from UCP2$^{-/-}$ mice after PAB compared to C57BL/6J (WT) mice

To further investigate, if changes in contraction and relaxation were related to alterations in cellular calcium handling in these mice, we measured calcium transients in isolated cardiomyocytes. $[Ca^{2+}]_i$ transients measured by Fura-2-AM were increased in cardiomyocytes isolated from the RV of PAB-operated UCP2$^{-/-}$ mice compared to those from PAB-operated WT mice (Figures 14a,c). No significant differences between UCP2$^{-/-}$ and WT mice subjected to PAB operation were noted in calcium transients of isolated cardiomyocytes from the LV (Figures14b,c).

* Calcium transient measurement was performed by AG Schlüter, Physiology Institute, Justus-Liebig-University, Giessen

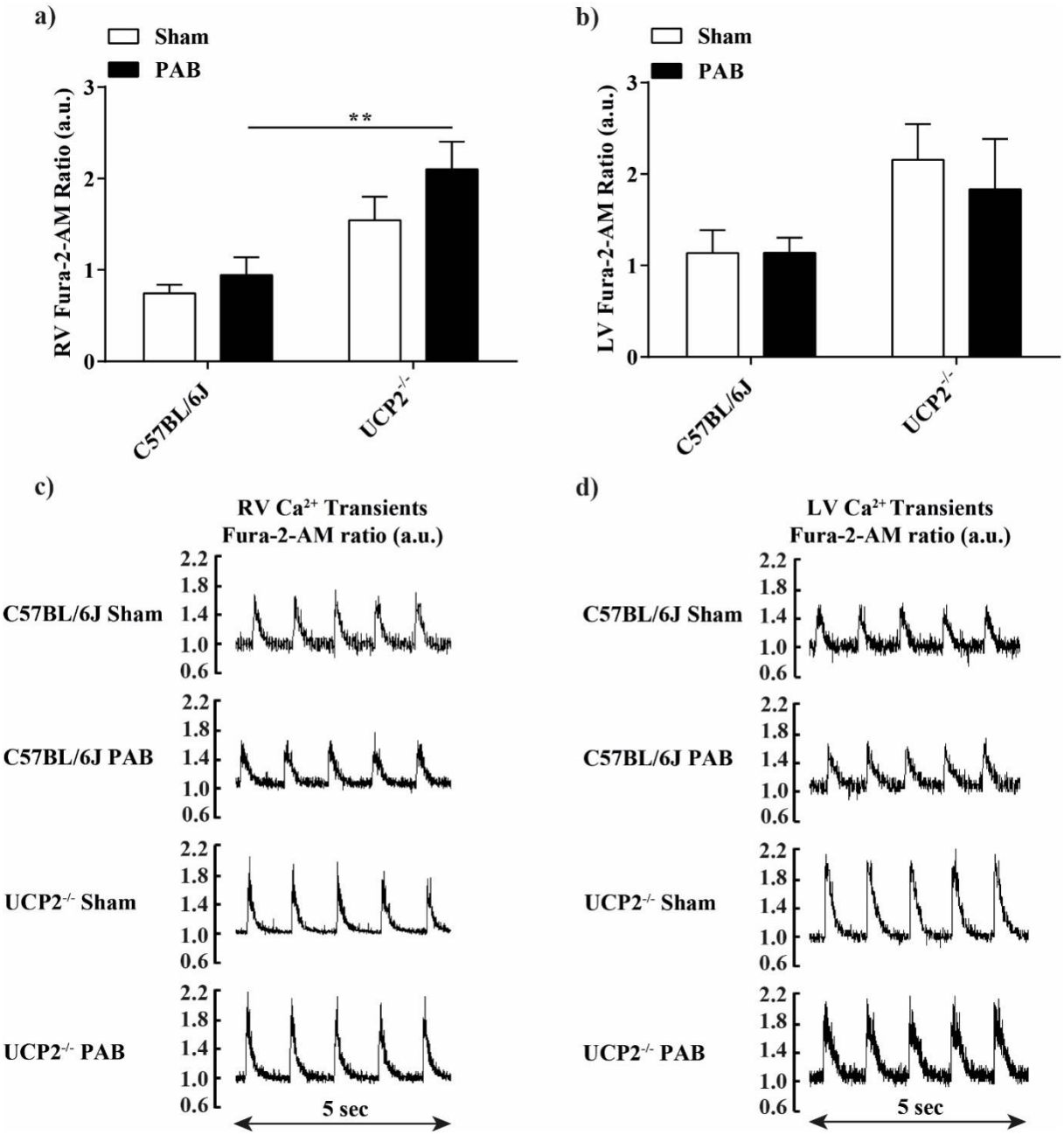

Figure 14. Calcium transients in cardiomyocytes isolated from the RV and LV three weeks after PAB

Quantitative analysis of Fura-2-AM fluorescence intensity (expressed in arbitrary units (a.u.)) indicating intracellular calcium ($[Ca^{2+}]_i$) transients in cardiomyocytes isolated from a) the right ventricle (RV) (n = 11-25 cells each group, from at least 3 isolations), and b) the left ventricle (LV) (n = 13-16 cells each group, from at least 3 isolations). Representative Ca^{2+} concentration traces during 5 seconds in individual cardiomyocytes isolated from c) the RV, and d) the LV. Values are depicted as mean ± SEM; **p < 0.01; analysis by two way ANOVA.

4.2.2.2. Decreased time of calcium to reach 50% of the basal value in cardiomyocytes from UCP2$^{-/-}$ mice after PAB compared to C57BL/6J (WT) mice

The time of calcium to reach again 50% of its basal value after maximal calcium increase was measured in order to understand the relationship between cardiomyocyte relaxation and calcium handling. Cardiomyocytes isolated from the RV of UCP2$^{-/-}$ mice reached faster 50% of their basal calcium level, compared to WT cardiomyocytes after PAB operation, but also after sham operation (Figure 15a). In cardiomyocytes isolated from the LV of PAB-operated UCP2$^{-/-}$ and PAB-operated WT mice, no significant change was observed in the time of calcium to reach 50% of its basal value (Figure 15b).

* Measurement of Ca^{2+} Time-to-Basal 50% was performed by AG Schlüter, Physiology Institute, Justus-Liebig-University, Giessen

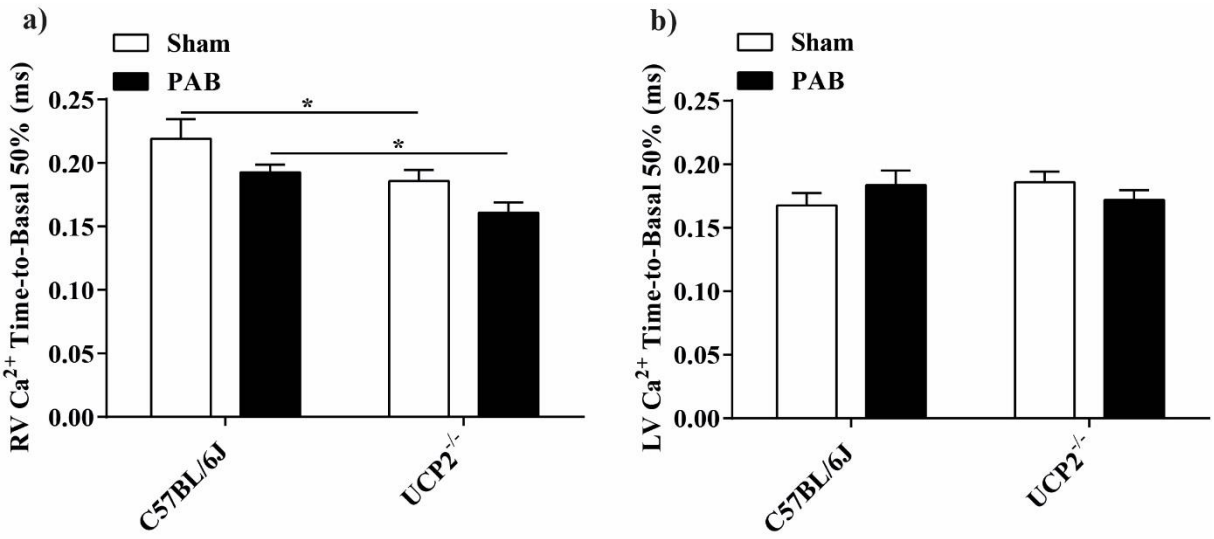

Figure 15. The time of calcium to reach 50% of basal level in cardiomyocytes isolated from the RV and LV three weeks after PAB

The time for the intracellular calcium ($[Ca^{2+}]_i$) to reach 50% of its basal level (Ca^{2+} Time-to-Basal 50%) in a) cardiomyocytes isolated from the right ventricle (RV), and b) cardiomyocytes isolated from the left ventricle (LV) (n = 11-25 cells each group, from at least 3 isolations). Values are depicted as mean ± SEM; *p < 0.05; analysis by two way ANOVA.

4.2.3. Expression of calcium handling proteins in cardiomyocytes from UCP2$^{-/-}$ mice after PAB compared to C57BL/6J (WT) mice

To determine the source of intracellular calcium ($[Ca^{2+}]_i$) alterations, we examined the expression of regulatory proteins of cardiac calcium handling: The sarcoplasmic/endoplasmic reticulum calcium ATPase 2a (SERCA2a), phospholamban (PLB), phosphorylated phospholamban (pPLB) and the Na^+-Ca^{2+} exchanger (NCX) which are major determinants of diastolic calcium clearance.

We also examined the expression of Mitofusin-2 (MFN2), a mitochondrial protein involved in SR-mitochondrial tethering, thereby regulating SR calcium handling.

* Measurement of calcium handling proteins' expression was performed by AG Schlüter, Physiology Institute, Justus-Liebig-University, Giessen

4.2.3.1. Increased SERCA2a expression in RV cardiomyocytes from UCP2$^{-/-}$ mice after PAB compared to C57BL/6J (WT) mice

Western blot analysis of protein extracts from cardiomyocytes isolated from the RV demonstrated an increase in the protein level of SERCA2a in cardiomyocytes from UCP2$^{-/-}$ mice subjected to PAB operation compared to the corresponding cardiomyocytes from sham-operated UCP2$^{-/-}$ and PAB-operated WT mice (Figures 16a,c). No significant difference was observed between PAB-operated UCP2$^{-/-}$ and PAB-operated WT mice in the protein level of SERCA2a from LV cardiomyocytes (Figures 16b,d).

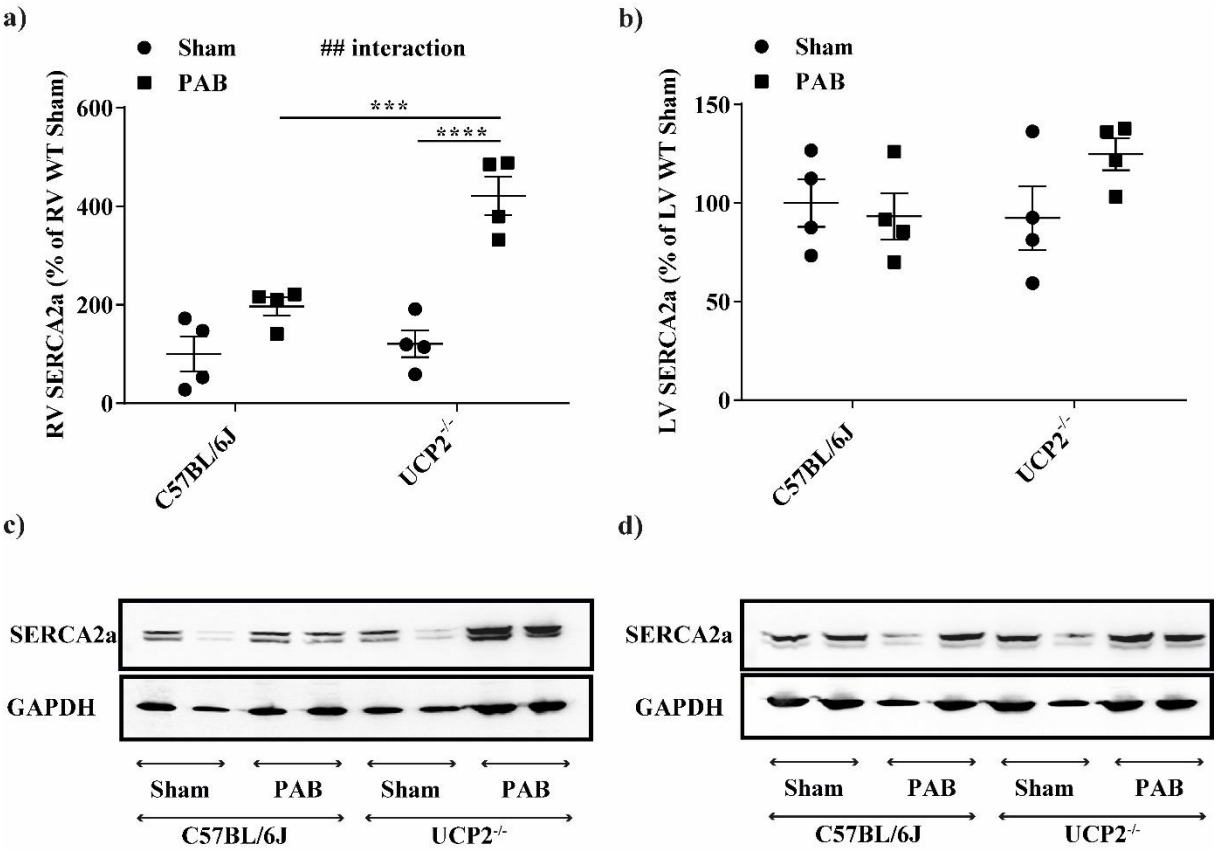

Figure 16. Expression of SERCA2a in cardiomyocytes isolated from the RV and LV three weeks after PAB

Sarcoplasmic/endoplasmic reticulum calcium ATPase 2a (SERCA2a) protein expression level in cardiomyocytes determined by western blot in a) the right ventricle (RV), and b) the left ventricle (LV) (n = 4 each group). Data are given in percent (%) of the average value of the RV or LV of WT sham-operated mice. Densitometric analysis for SERCA2a expression was performed and values were normalized to glycerinaldehyd-3 phosphate-dehydrogenase (GAPDH) expression. Representative western blot of c) the RV, and d) the LV. Values are depicted as mean ± SEM; ***$p < 0.001$ and ****$p < 0.0001$; interaction between genotype and treatment was statistically significant for RV SERCA2a protein expression; analysis by two way ANOVA.

4.2.3.2. Unchanged NCX expression in cardiomyocytes from UCP2$^{-/-}$ mice after PAB compared to C57BL/6J (WT) mice

Western blot analysis of protein extracts from cardiomyocytes isolated from the RV and LV demonstrated no change in the protein level of NCX between UCP2$^{-/-}$ and WT mice subjected to PAB operation compared to the corresponding sham-operated mice (Figures 17a-d).

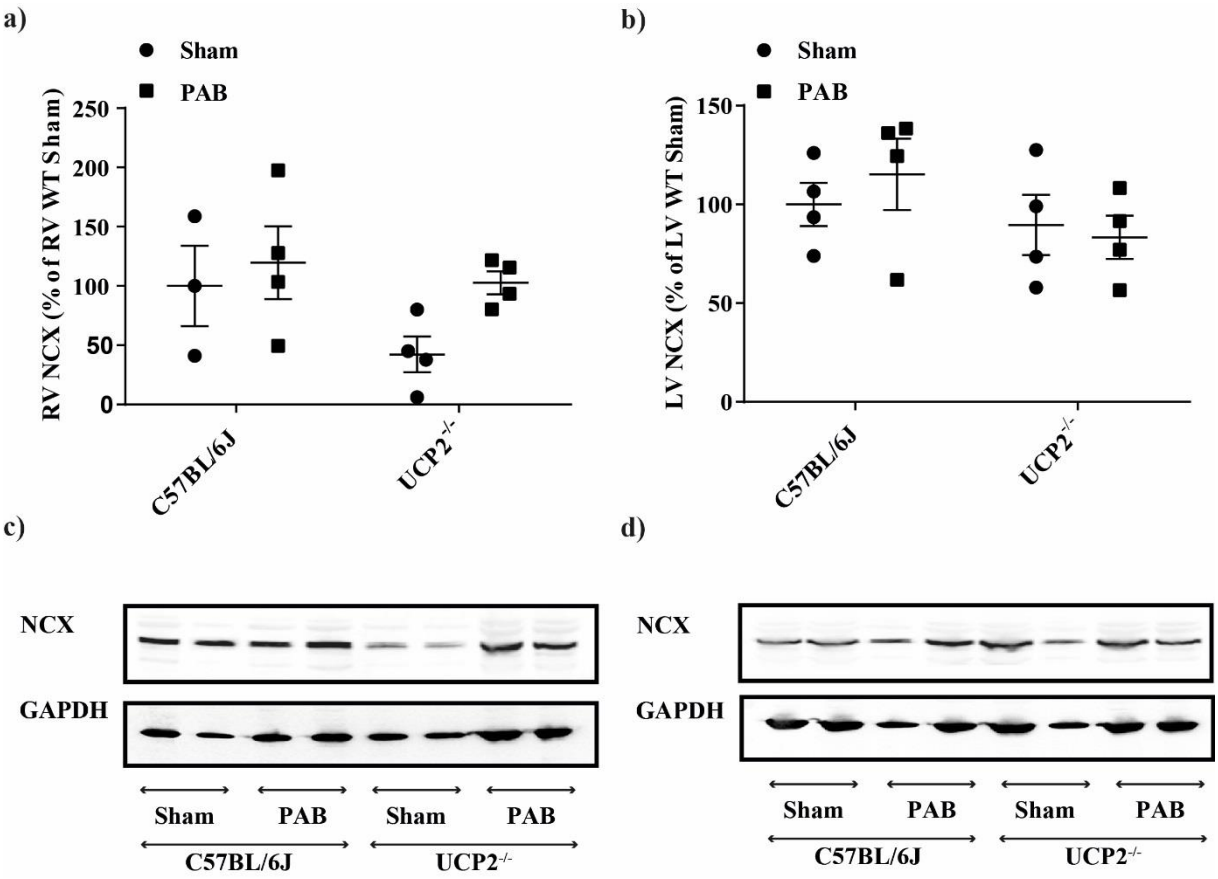

Figure 17. Expression of NCX in cardiomyocytes isolated from the RV and LV three weeks after PAB

Na^+-Ca^{2+} exchanger (NCX) protein expression level in cardiomyocytes determined by western blot in a) the right ventricle (RV), and b) the left ventricle (LV) (n = 4 each group). Data are given in percent (%) of the average value of the RV or LV of WT sham-operated mice. Densitometric analysis of NCX expression was performed and values were normalized to glycerinaldehyd-3 phosphate-dehydrogenase (GAPDH) expression. Representative western blot of c) the RV, and d) the LV. Values are depicted as mean ± SEM; analysis by two way ANOVA.

4.2.3.3. Increased MFN2 expression in RV cardiomyocytes from UCP2$^{-/-}$ mice after PAB compared to C57BL/6J (WT) mice

MFN2 is an SR-mitochondria tether in the heart which connects the SR and mitochondria thereby promoting calcium exchange between both cell organelles. Expression of MFN2 was increased in cardiomyocytes isolated from the RV of UCP2$^{-/-}$ mice subjected to PAB operation (Figures 18a,c). No significant difference was observed in the protein level of MFN2 in LV cardiomyocytes from PAB-operated UCP2$^{-/-}$ and PAB-operated WT mice (Figures 18b,d).

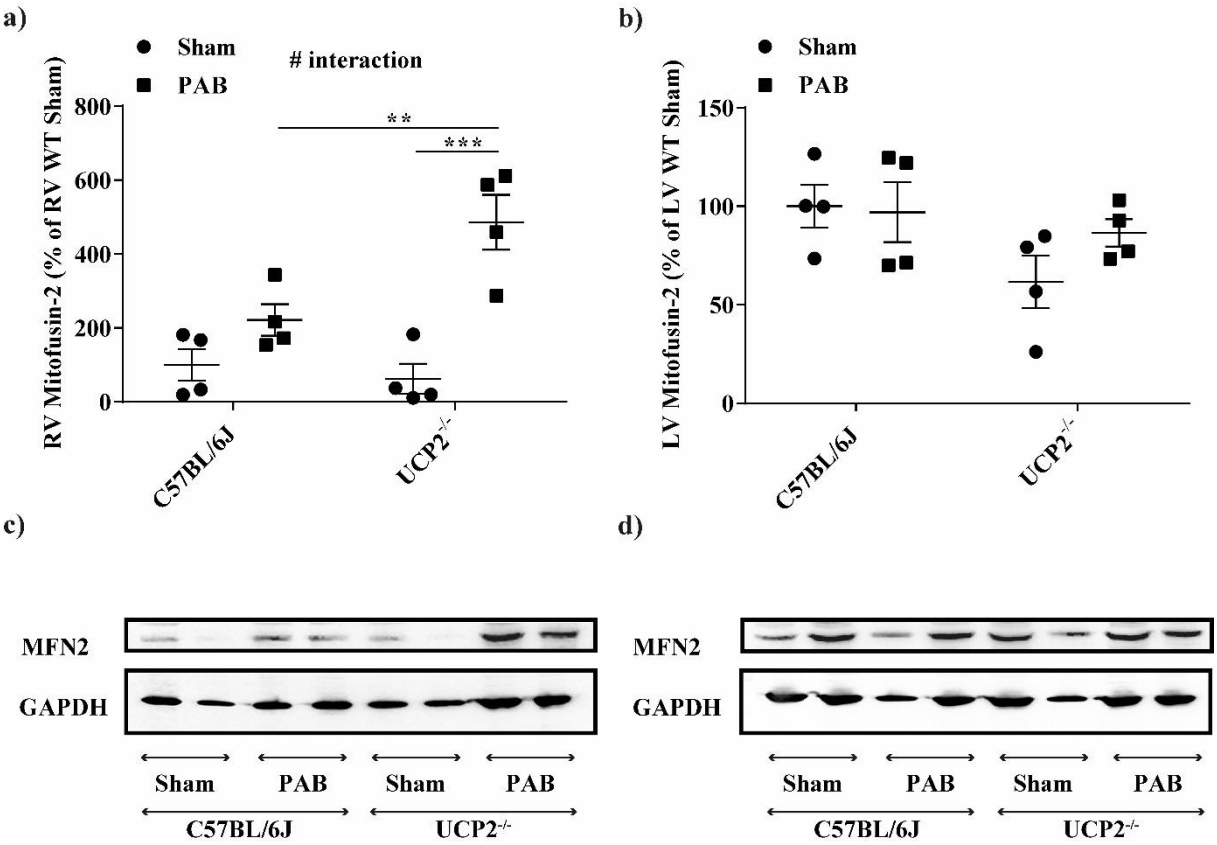

Figure 18. Expression of MFN2 in cardiomyocytes isolated from the RV and LV three weeks after PAB

Mitofusin-2 (MFN2) protein expression level in cardiomyocytes determined by western blot in a) the right ventricle (RV), and b) the left ventricle (LV) (n = 4 each group). Data are given in percent (%) of the average value of the RV or LV of WT sham-operated mice. Densitometric analysis for MFN2 expression was performed and values were normalized to glycerinaldehyd-3 phosphate-dehydrogenase (GAPDH) expression. Representative western blot of c) the RV, and d) the LV. Values are depicted as mean ± SEM; **p < 0.01 and ***p < 0.001; interaction between genotype and treatment was statistically significant for RV MFN2 protein expression; analysis by two way ANOVA.

4.2.3.4. Increased PLB expression in RV cardiomyocytes from UCP2$^{-/-}$ mice after PAB compared to C57BL/6J (WT) mice

Expression of PLB showed a significant increase in cardiomyocytes isolated from the RV of UCP2$^{-/-}$ mice after PAB operation (Figures 19a,e). In cardiomyocytes isolated from the LV, no significant change was observed between WT and UCP2$^{-/-}$ mice after PAB operation (Figures 19b,f). Amount of phosphorylated PLB compared to total PLB was unchanged between PAB- and sham-operated mice (Figures 19c-d, e-f).

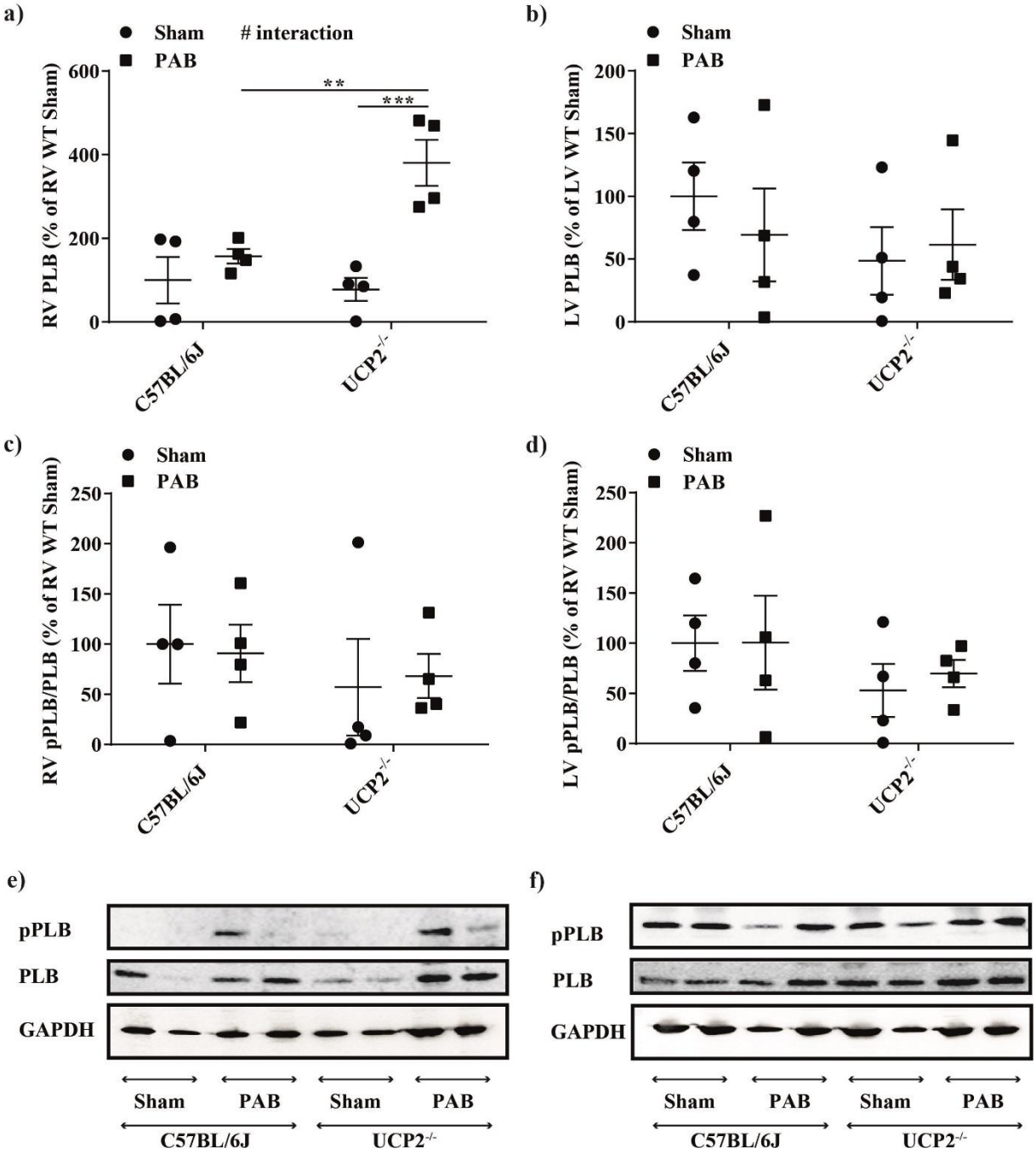

Figure 19. Expression of PLB and amount of pPLB in cardiomyocytes isolated from the RV and LV three weeks after PAB

Phospholamban (PLB) protein expression level in cardiomyocytes determined by western blot in a) the RV and b) the LV (n = 4 each group). Amount of phosphorylated phospholamban (pPLB) to total phospholamban (PLB) in cardiomyocytes determined by western blot in c) the right ventricle (RV) and d) the left ventricle (LV) (n = 4 each group). Densitometric analysis for PLB expression was performed and values were normalized to glycerinaldehyd-3 phosphate-dehydrogenase (GAPDH) expression. Amount of pPLB was normalized to amount of PLB protein. Representative western blot of e) the RV and f) the LV. Values are depicted as mean ± SEM; **$p < 0.01$ and ***$p < 0.001$; interaction between genotype and treatment was statistically significant for RV PLB protein expression; analysis by two way ANOVA.

4.2.4. The role of mitochondrial ROS and respiration

4.2.4.1. Increased mitochondrial superoxide concentration in ISO-stimulated cardiomyocytes isolated from UCP2$^{-/-}$ mice after PAB compared to C57BL/6J (WT) mice

To investigate the role of mitochondrial ROS in cardiomyocyte function after PAB, we measured mitochondrial ROS release in isolated intact cardiomyocytes. Quantification of MitoSOX red fluorescence after stimulation of cardiomyocytes with ISO showed higher mitochondrial superoxide concentration in cardiomyocytes isolated from the RV of UCP2$^{-/-}$ mice after PAB compared to WT cardiomyocytes (Figures 20a,b). Mitochondrial superoxide concentration in cardiomyocytes isolated from the RV of WT mice showed a decline after PAB compared to the sham group (Figures 20a,b). No significant change was observed in cardiomyocytes isolated from the LV of WT and UCP2$^{-/-}$ mice after PAB (Figures 21a,b).

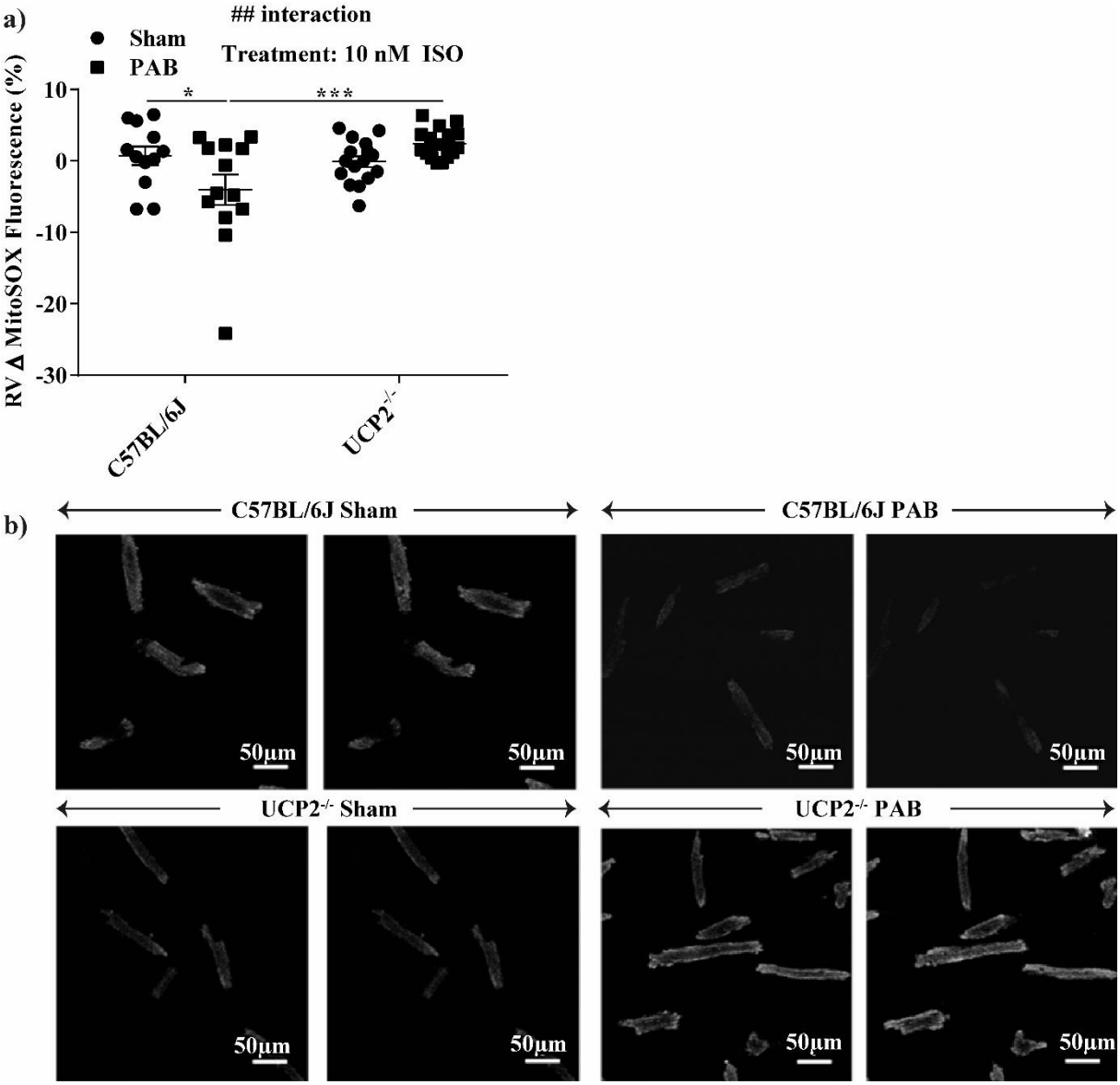

Figure 20. Mitochondrial superoxide release in cardiomyocytes isolated from the RV three weeks after PAB

a) Superoxide analysis as percent (%) of MitoSOX red fluorescence alteration (ΔMitoSOX) after stimulation with 10 nmol/L isoprenaline (ISO) compared to baseline in cardiomyocytes isolated from the right ventricle (RV) (n = 12-18 cells each group, from at least 3 isolations). b) Representative images of MitoSOX staining in cardiomyocytes after stimulation with 10 nmol/L ISO. Values are depicted as mean ± SEM; *p < 0.05 and ***p < 0.001; interaction between genotype and treatment was statistically significant for RV ΔMitoSOX fluorescence (%); analysis by two way ANOVA.

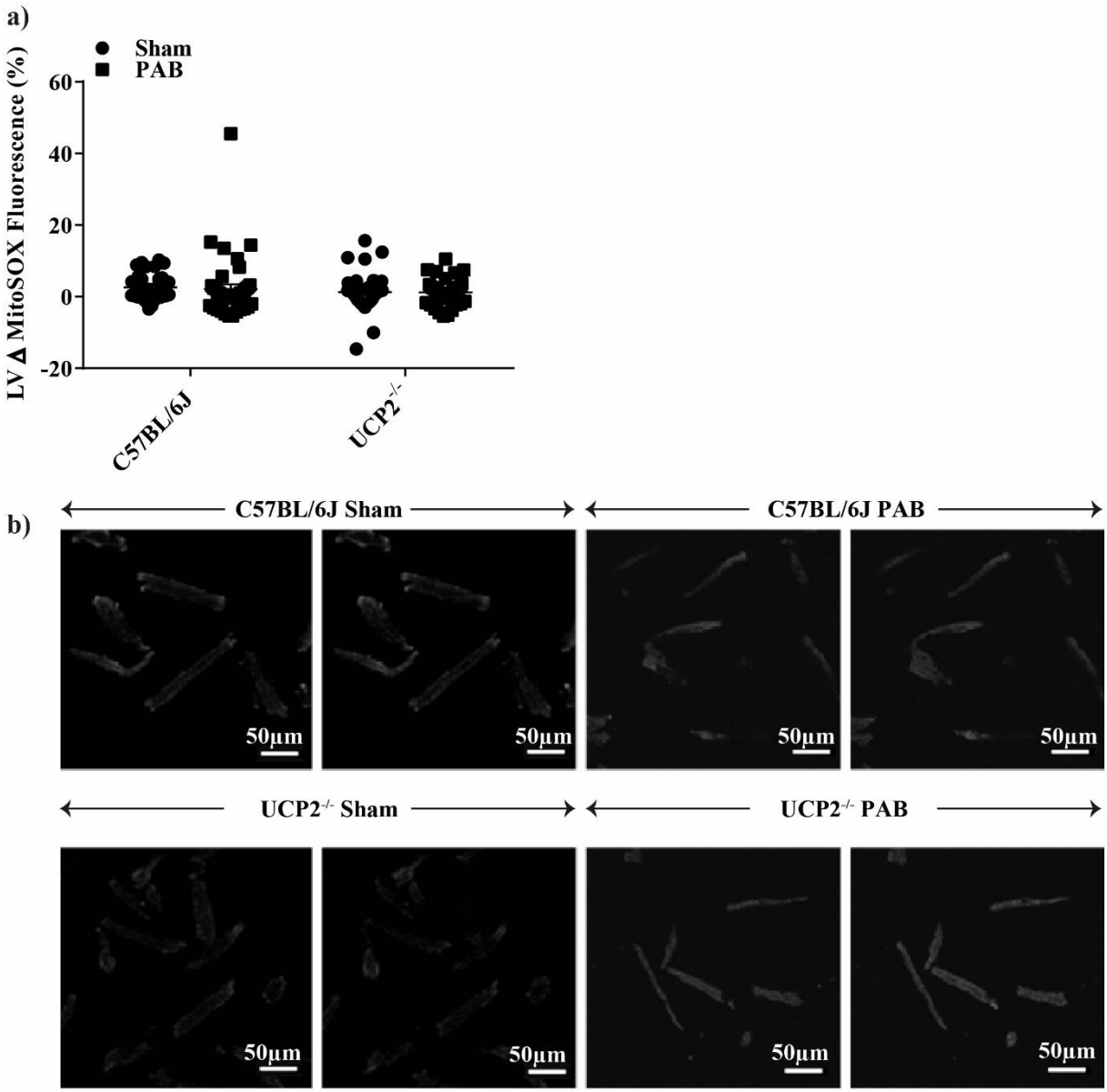

Figure 21. Mitochondrial superoxide release in cardiomyocytes isolated from the LV three weeks after PAB

a) Superoxide analysis as percent (%) of MitoSOX fluorescence alteration (ΔMitoSOX) after stimulation with 10 nmol/L isoprenaline (ISO) compared to baseline in cardiomyocytes isolated from the left ventricle (LV) without ISO stimulation (n = 40-55 cells each group, from at least 3 isolations). b) Representative images of MitoSOX staining in cardiomyocytes after stimulation with 10 nmol/L ISO. Values are depicted as mean ± SEM; analysis by two way ANOVA.

4.2.4.2. Impaired cardiomyocyte function after ROS inhibition

In order to prove the relevance of ROS for cardiomyocyte function, we measured cardiomyocyte contraction in presence of the superoxide scavenger tempol in isolated and cultured rat cardiomyocytes. Fractional shorting was decreased and the time to 50% of peak contraction value was increased in the presence of tempol (Figures 22a,b), while contraction and relaxation velocity were unchanged (Figures 22c,d).

* Tempol studies were performed by AG Schlüter, Physiology Institute, Justus-Liebig-University, Giessen

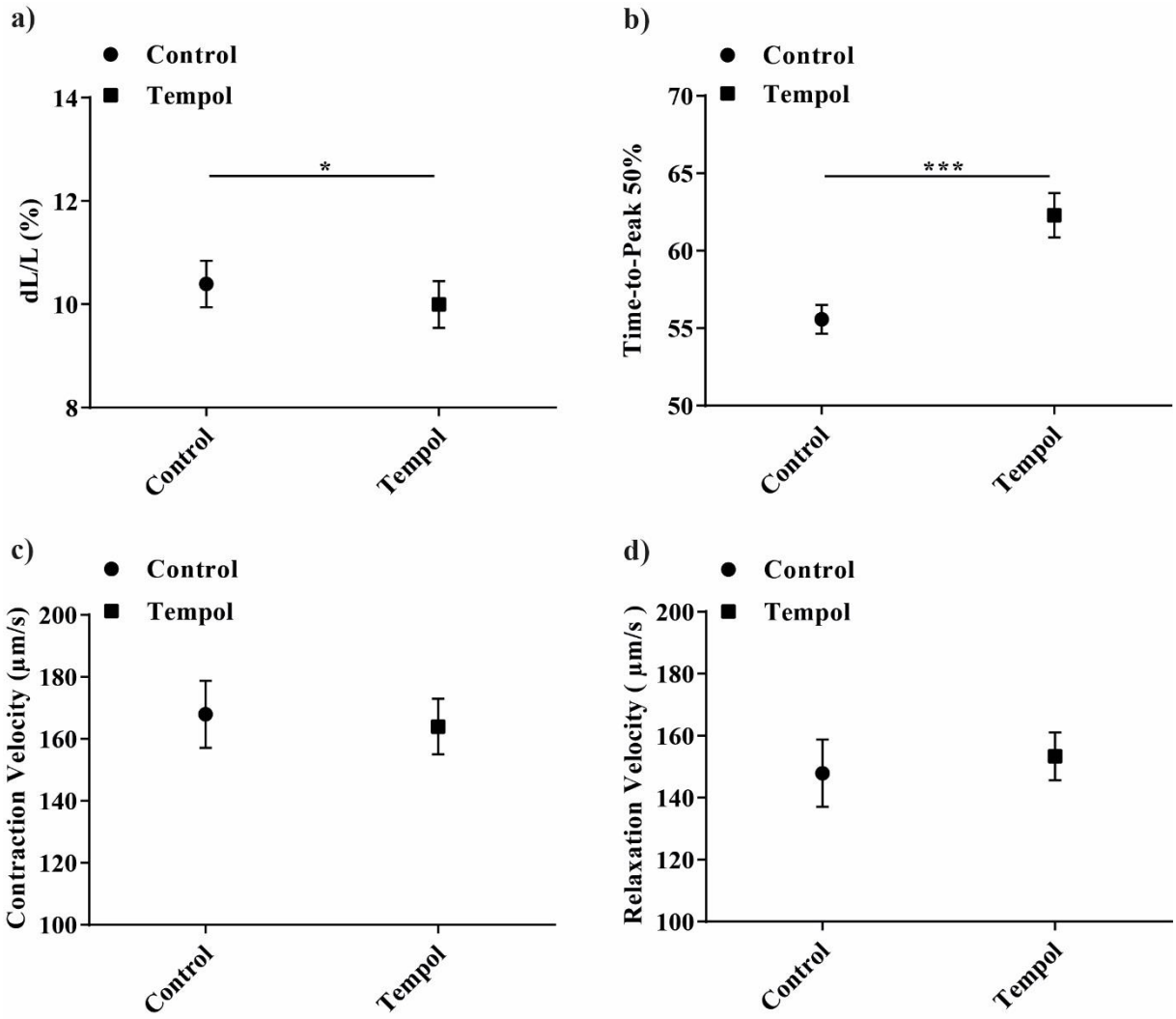

Figure 22. Cardiomyocyte function in the presence of tempol

Ratio of cell length shortening to diastolic cell length (dL/L) as percent (%) in isolated and cultured rat cardiomyocytes after treatment with 1 mmol/L tempol for 24 hrs (n = 45 cells each group, from at least 3 isolations), b) calcium time to 50% of peak in cardiomyocytes (n = 36 cells each group, from at least 3 isolations), c) contraction velocity (n = 45 cells each group, from at least 3 isolations), and d) relaxation velocity (n = 45 cells each group, from at least 3 isolations) in µm/s. Values are depicted as mean ± SEM;*$p < 0.05$ and ***$p < 0.001$; analysis by Student's t-Test.

4.2.4.3. Unchanged mitochondrial respiration in permeabilized muscle fibers independent of the genotype and treatment

Respiration of cardiac muscle fibers is shown in the presence of the mitochondrial substrates/inhibitors: pyruvate, ADP, malate/glutamate, octanoylcarnitine, succinate and Antimycin A. No significant alteration was observed in any group, neither in the RV nor the LV (Figures 23a,b).

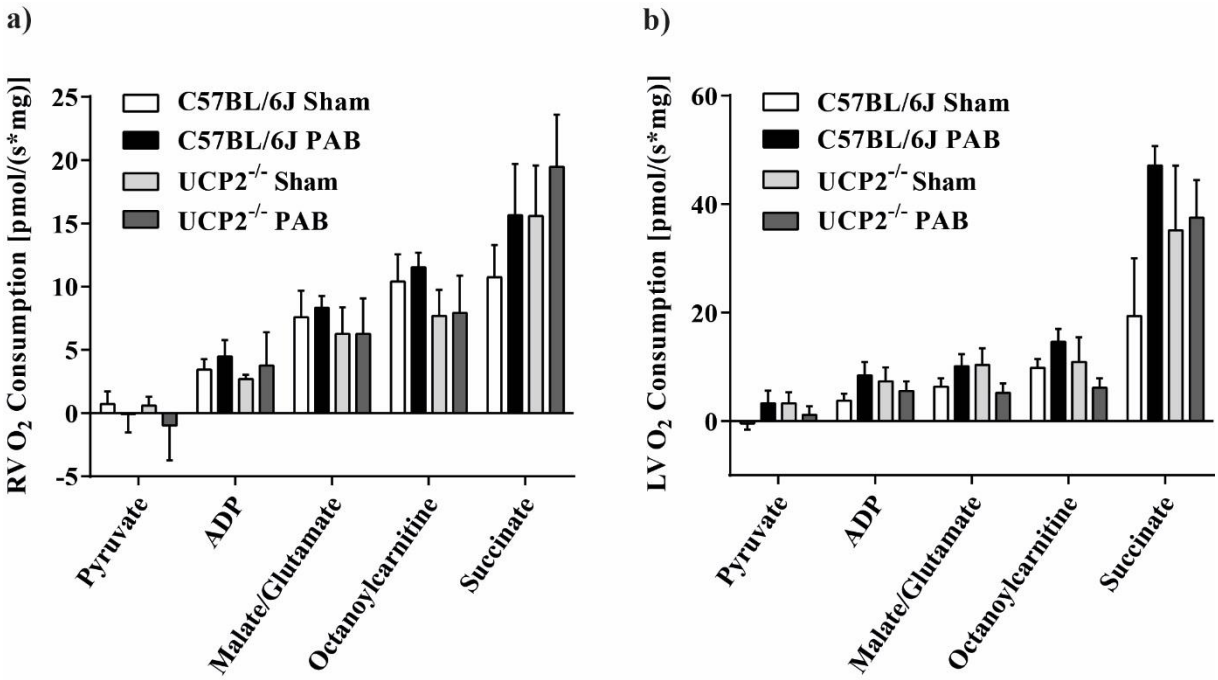

Figure 23. Respiratory data from cardiac muscle fibers of the RV and LV three weeks after PAB

Oxygen consumption in permeabilized muscle fibers from a) the right ventricle (RV), and b) the left ventricle (LV) after treatment with pyruvate, ADP, malate/glutamate, octanoylcarnitine, and succinate corrected for oxygen consumption in presence of antimycin A (n = 3-6 each group). Values are depicted as mean ± SEM; analysis by two way ANOVA.

4.3. Expression of UCP3 in C57BL/6J (WT) and UCP2$^{-/-}$ mice

In order to understand if there is a relation between UCP2 and UCP3 expression, UCP3 gene and protein expression was investigated in WT and UCP2$^{-/-}$ mice. Downregulation of UCP2 was not associated with compensatory upregulation of UCP3.

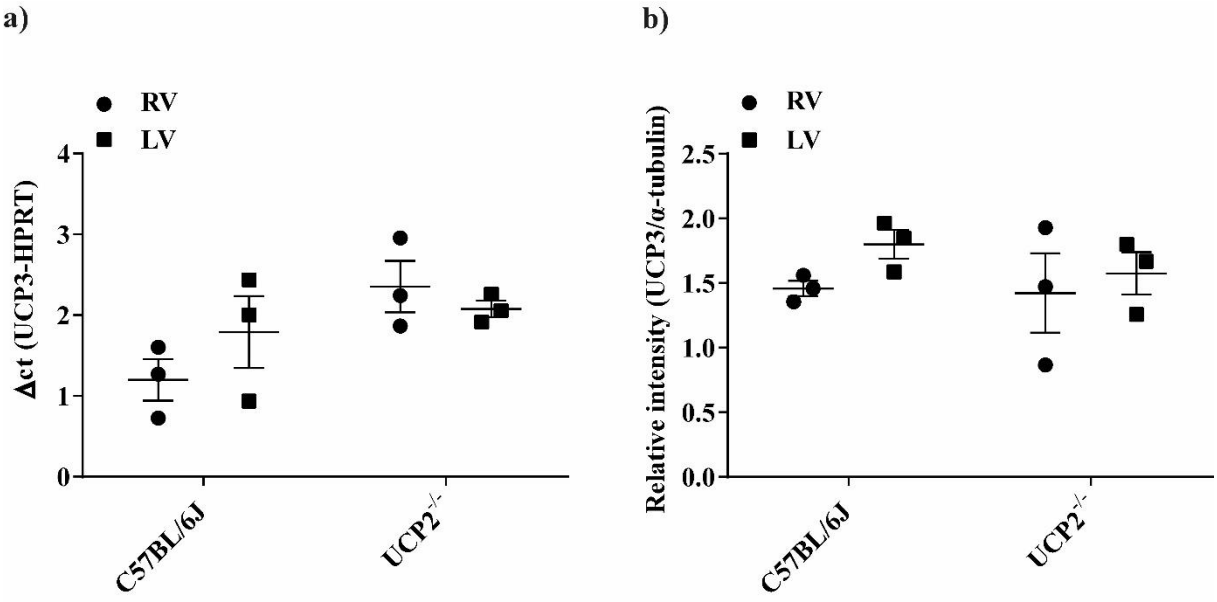

Figure 24. Relative UCP3 gene and protein regulation in the RV and LV

Uncoupling protein 3 (UCP3) mRNA expression in the right ventricle (RV) and left ventricle (LV) (n = 3 each group) compared to expression of the house-keeping gene hypoxanthine phosphoribosyltransferase (HPRT), b) UCP3 protein expression in the RV and LV homogenates compared to expression of α-tubulin (n = 3 each group). Values are depicted as mean ± SEM. Analysis by two way ANOVA.

5. Discussion

Since physicians recognized the risks of PH and associated RVF 30 years ago, research focusing on the right heart has become more important. RVF is a common result of severe PH and the major cause of death in pulmonary vascular hypertensive diseases [1, 177]. Additionally, it has been shown that patients suffering from the left heart insufficiency have worse prognosis, if RV function is also compromised [1]. Although RV dysfunction plays an important prognostic role in PH patients, there are relatively few data on the mechanisms of chronic RV dysfunction and failure despite considerable research efforts [9, 178, 179]. Compared to treatment options for LV dysfunction, there is a lack of therapeutic options specifically targeting RV function.

Here we demonstrate for the first time, that the lack of the mitochondrial protein UCP2 has a protective effect on pressure overload-induced RV dysfunction. This conclusion is based on our findings that RV systolic and global function was preserved *in vivo* in $UCP2^{-/-}$ mice after PAB operation, compared to WT mice. *In vitro* experiments with cardiomyocytes isolated from $UCP2^{-/-}$ mice demonstrated better contraction and relaxation properties compared to cardiomyocytes isolated from WT mice after PAB.

Lack of UCP2 improved RV function and cardiomyocyte performance after PAB operation

UCP2 is an inner membrane mitochondrial carrier protein expressed in the mammalian heart under normal conditions. The exact molecular function of UCP2 is unknown, but it has been postulated to cover a number of cellular processes including regulation of mitochondrial calcium, attenuation of ROS release, uncoupling function, elevated fatty acid oxidation, increased glutamine oxidation and negative regulation of pyruvate uptake for respiration [104, 105, 118, 180, 181].

The role of UCP2 in mitochondrial Ca^{2+} regulation and the exact mechanism by which mitochondrial Ca^{2+} controls E-C coupling in the heart are still obscure. It has been shown that UCP2 overexpression in neonatal cardiomyocytes impaired E-C coupling by decreasing $[Ca^{2+}]_m$ uptake, altering beat-to-beat $[Ca^{2+}]_c$ handling, and thus interfering with calcium-induced calcium release from the SR [182]. Conversely, a trend towards a diminished peak $[Ca^{2+}]_c$ transient was observed in isolated cardiomyocytes from UCP2 deficient mice which results in reduction of mitochondrial Ca^{2+} transients in cardiomyocytes [117]. Elevated UCP2 expression has also been shown to protect neonatal rat ventricular cardiomyocytes from cell death by attenuating mitochondrial Ca^{2+} overload which is an important trigger of apoptosis [183]. However, the essential role of UCP2 for mitochondrial Ca^{2+} uptake has recently been challenged [117, 180]. The work of Motloch et al supports the concept, that cardiac UCP2

through interaction with other components of the calcium signalling complex indirectly modulates Ca^{2+} transport across the IMM [117]. The claim that UCP2 has regulatory function in Ca^{2+} uptake, but does not directly participate in calcium flux across the mitochondrial membrane, could be substantiated as the mitochondria in UCP2 KO mice are still able to take up Ca^{2+} normally [184]. These findings support a modulating role for UCP2 in mitochondrial Ca^{2+} uptake, Ca^{2+} handling and Ca^{2+} dynamic in the heart, although the molecular mechanism remains unclear.

Regulation of ATP synthesis has also been postulated as another possible function of UCP2 [181, 185]. As energy balance plays a crucial role in heart function, many studies focused on this aspect of UCP2. In heart failure, increased UCP2 levels led to less efficient ATP synthesis and thus further promoting the progression of heart failure due to increased uncoupling [185]. In a mouse model of aortic regurgitation, UCP2-induced ATP deficiency has been shown as a predominant cause of heart failure [186]. Moreover, upregulated UCP2 expression in pressure overload-induced heart failure by constriction of the abdominal aorta in rats was associated with decreased ATP levels [187]. However in another study, elevated UCP2 expression resulted in no significant alteration of total cellular ATP levels [182]. Contrary to these findings, deficiency of UCP2 attenuated right heart hypertrophy in the murine model of TAC which supports the hypothesis that UCP2 suppression was protective probably due to decreased myocyte apoptosis and increased ATP production [188].

The beneficial role of UCP2 via decreasing cellular ROS has been proposed by several studies. The respiratory chain generates ROS which are well known to induce cytosolic and mitochondrial Ca^{2+} signalling, followed by the deterioration of mitochondrial function [189]. In the failing heart, increased oxidative stress produces mitochondrial damage, which results in a further production of ROS from multiple sources and this finally creates a vicious cycle of oxidative stress and energetic decline [189]. Of note, UCP2 affects ROS production by dissipating the electrochemical gradient. It was shown that UCP2 plays a protective role in heart failure as UCP2 overexpression attenuated the detrimental effects of ROS on cardiomyocyte cell death and left heart function via inhibition of mitochondrial death pathway [183]. In this work, Teshima et al showed that overexpression of UCP2 resulted in an attenuated degree of superoxide generation following prolonged exposure to H_2O_2, and thus decreased apoptosis in rat neonatal cardiac myocytes [183]. Another study also demonstrated that increased UCP2 expression protects LV cardiomyocytes against oxidative stress and ischemia reperfusion injury through modulating ROS generation [190]. The importance of UCP2 in protecting against exogenous oxidant stress and the doxorubicin-induced cardiotoxicity was also reported by

Bugger et al [191]. In contrast, we demonstrate that ISO-stimulated cardiomyocytes from PAB $UCP2^{-/-}$ mice have increased mitochondrial superoxide concentration compared to WT mice which was associated with preserved RV function. The observed increase in mitochondrial superoxide production induced by β-adrenergic stimulation might be a direct effect of activation of the cAMP–PKA signalling pathway or it could be a consequence of the increased Ca^{2+} transients in the presence of β-adrenergic stimulation [192]. Therefore, UCP2 can potentially play a major role in the failing heart, based on the fact that the failing heart is challenged by enhanced oxidative stress. It is still a matter of debate under which conditions and by which mechanism, UCP2 and the regulation of ROS levels would be protective in the development of heart failure. Moreover, ROS may activate proliferative pathways and thus promote adaptive RVH [193].

In summary, the above studies show that UCP2 may have either deleterious or protective effects on right heart function during development of right heart hypertrophy and failure. The reported decreased ATP production due to overexpression of UCP2 may promote the transition from heart hypertrophy to failure [186, 187]. Calcium studies show controversial findings, but the protective effects in UCP2 deficient mice may be based on improved mitochondrial calcium buffering which results in diminished intracellular diastolic calcium content and more efficient E-C coupling. However, UCP2, which is involved in a negative feedback loop to inhibit mitochondrial ROS production, also may be beneficial in heart failure as it allows the RV to maintain in a fully compensated state. In our study, the sustained RV function in UCP2 deficient mice after PAB is in line with the findings showing beneficial effects of decreased UCP2 expression. Our finding suggest that deficiency of UCP2 might be protective by preserving cardiac function in the setting of PAB-induced RVH.

The observed discrepancies in the studies may be partly explained by the differences in animal models of heart hypertrophy/failure in combination with species-specific UCP2 expression pattern [194]. Furthermore, studies focussing on either adaptive or maladaptive forms of heart hypertrophy might be responsible for some of these controversies. The differences in the embryological origin of the RV and LV may result in controversial findings with regard to studies comparing RV and LV [194].

The expression level and effect of UCP2 may be influenced by the stage of heart failure, severity of disease, and animal model. Furthermore, UCP2 function might be species-specific. Particularly, increased UCP2 expression appears to occur mostly in end stage of left heart failure [194]. Chronic left heart failure resulted in elevated myocardial UCP2 expression has

been linked to myocardial energy deficiency [195]. In hypoxia-induced RVH, increased UCP2 mRNA expression suggested a probable role for UCP2 in right heart remodelling as well as contractile function [92]. Furthermore, elevated cardiomyocyte apoptosis is observed only prior to UCP2 upregulation in a model of pressure overload-induced LVH which proposes regulatory effect of UCP2 in the stage of transition from cardiac hypertrophy to cardiac failure [196]. In rats with severe aortic regurgitation, UCP2 was initially decreased, but later in the course of the disease increased significantly compared to sham-operated rats [186]. In our study, the functional improvements in UCP2 KO mice are observed 3 weeks after operation which is shown an optimal time point for development of right heart hypertrophy in the PAB model. In summary, different animal models and species as well as the stage of heart failure differentially alter the expression of UCP2 in the heart.

The clinical utility of TAPSE and RV Tei index for evaluation of RV function and in the prediction of an adverse outcome in cardiac failure has been shown as a helpful approach in animal studies and therefore were analysed in this study too. Our finding showed increased RVH in both WT and $UCP2^{-/-}$ mice after PAB operation. However, RV longitudinal systolic function, represented by TAPSE, and RV global function represented by Tei index, were preserved in UCP2 deficient mice. Furthermore, RV inner diameter in our findings was less increased in UCP2 deficient mice after PAB operation compared to WT mice indicating less RV dilation in $UCP2^{-/-}$ mice. Our findings provide evidence that $UCP2^{-/-}$ mice have better functional adaptation to increased pressure overload compared to WT mice, thus protecting the $UCP2^{-/-}$ mice from progression towards RVF.

Interestingly, in line with our previously published work, parameters of RV function in $UCP2^{-/-}$ mice were slightly decreased under basal condition compared to WT mice [119]. Such modification in RV function may be caused by long-term maladaptation to slightly increased RV afterload, as $UCP2^{-/-}$ mice exhibit mild PH under basal condition [119]. Moreover, effects of UCP2 on RV function may depend on the type and magnitude of the pressure overload and stage of heart hypertrophy, so that UCP2 may play a beneficial role in milder PH induced by CH exposure and it has deleterious effects in severe pressure overload induced by PAB.

Due to the observed improvement in RV function independently from cardiomyocyte hypertrophy (indicated by unchanged heart ratio), we focused in our research on functional assessment of cardiomyocytes. Our study showed that PAB operation could cause an increase in fractional shortening in RV-isolated cardiomyocytes from both WT and KO mice under basal condition. This increase was even more in RV- isolated cardiomyocytes from UCP2 deficient

mice after PAB operation compared to sham-operated mice under stimulation with ISO. In WT mice, fractional shortening of myocytes remained unchanged under stimulation after PAB operation which shows that WT cardiomyocytes could not further augment this parameter of cell contractility. We could conclude that after PAB operation UCP2 deficiency potentiated the β-adrenoceptor-dependent cell shortening. In cardiomyocytes isolated from the LV, UCP2 deficient mice showed increased fractional shortening after sham and PAB operation compared to WT mice. This effect suggests that UCP2 deficiency also plays an important role for LV function, as has been shown in previous studies [188]. We could also demonstrate increased contraction velocity and relaxation velocity in cardiomyocytes isolated from the RV of $UCP2^{-/-}$ mice after PAB operation compared to cardiomyocytes isolated from the RV of WT mice after PAB operation under stimulation with ISO. PAB operation by itself resulted in an increased contraction velocity and relaxation in myocytes from RV under basal condition while after stimulation with ISO, PAB conferred no further augmentation for WT animals most probably because their myofibrils are already at maximum contraction rate with ISO. In UCP2 deficient mice under stimulation, the contraction velocity and relaxation velocity of cardiomyocytes from RV could be augmented by PAB operation as probably the myofibrils still did not reach their maximum contraction rate with ISO or the $UCP2^{-/-}$ cardiomyocytes show different response to β-adrenergic stimulation. The underlying mechanisms could be increased Ca^{2+} storage, Ca^{2+} release, and Ca^{2+} re-uptake by SR in $UCP2^{-/-}$ cardiomyocytes after PAB operation or e.g. different density of β-adrenoceptors. No effect of PAB on basal contraction velocity and relaxation velocity is observed in cardiac myocytes from the LV. PAB revealed augmented contraction velocity in LV-isolated myocytes from WT mice after stimulation. Cells from $UCP2^{-/-}$ mice showed augmented contraction velocity and relaxation velocity after β-adrenergic stimulation in both sham and PAB conditions which was almost equivalent to cells from WT mice.

The contractile profile of the myocytes was increased in RV-isolated cardiomyocytes from WT mice after PAB operation while the CO which represents the global heart function is decreased in these mice. The CO is determined by the pulmonary PVR and RV contractility. Despite the increased contraction of the isolated cardiomyocytes which can cause increased RV contractility, obviously the increased afterload of the RV could not be compensated. This would be described as a "decoupled" state which claims that the right ventriculo-arterial decoupling limits the CO adaptation to increased afterload [197]. As several components are involved in regulation of calcium flux in myocytes, further investigation of a few major calcium signalling components was done in this study.

Discussion

Improved intracellular systolic calcium increase and diastolic calcium decrease in myocytes from UCP2$^{-/-}$ after PAB operation correlated to altered SERCA2a expression

First we set out to test whether increased contraction and relaxation of UCP2$^{-/-}$ cardiomyocytes were correlated with altered calcium flux. In the absence of myofilament properties alteration, the main determinant for reduced cardiac contraction of the LV is decreased cytosolic calcium release from the SR Ca^{2+} into the cytoplasm mediated by the cardiac RyR channels [198]. As SR Ca^{2+} load is a key factor in determining the amount of SR Ca^{2+} release, besides the disturbed SR calcium release via RyR_2 channels, low SR calcium content itself can be the underlying cause of deteriorated E-C coupling and subsequent failed myocyte contraction. Treatment of mice with ryanodine, an inhibitor of the SR Ca^{2+} release, resulted in cardiac hypertrophy and contractile dysfunction in mice [199]. A hallmark feature of altered systolic performance in the failing left heart is reduced SR Ca^{2+} load and impaired SR function [151]. In cardiac failure, the inability to increase contractility during physiologic stress is consistently associated with reduced SR Ca^{2+} load [200]. Decrease in SR Ca^{2+} content and release has been shown in end-stage failing LV human myocardium [201]. In failing human hearts, both $[Ca^{2+}]_i$ transients and SR Ca^{2+} release are significantly reduced. Thus altered Ca^{2+} homeostasis is the result of the decreased capacity of the SR to accumulate Ca^{2+} [201]. Furthermore, reduced peak systolic Ca^{2+}, increased Ca^{2+} transient duration and prolonged Ca^{2+} transient decay time have also been shown in myocytes isolated from failing left hearts [202, 203]. These observations indicate that decreased systolic Ca^{2+} transient amplitude secondary to reduced SR Ca^{2+} load is responsible for decreased cardiac contractility and reduced CO [202, 203].

Our findings demonstrated the $[Ca^{2+}]_i$ transients were increased in RV cardiomyocytes from UCP2$^{-/-}$ mice after PAB operation. Increased $[Ca^{2+}]_i$ transient depicts the elevated $[Ca^{2+}]_i$ released from internal Ca^{2+} stores and/or elevated Ca^{2+} entered to the cardiomyocyte which is in accordance with increased contractile velocity in these myocytes. The shortened time of Ca^{2+} to reach 50% of its basal value in the RV cardiomyocytes from UCP2$^{-/-}$ mice after PAB operation also demonstrates the faster removal of Ca^{2+} from cytosol to SR by calcium channels mostly SERCA2a or RyR which is in accordance with relaxation velocity results in these cardiomyocytes. A tendency to increased $[Ca^{2+}]_i$ transients was also observed in RV cardiomyocytes from WT mice after PAB operation which was not significant. A tendency to increased contraction velocity was observed in these cardiomyocytes while the relaxation velocity did not show a tendency to increase.

One of the factors determining SR calcium content is calcium reuptake into the SR via the PLB regulated SERCA2a protein. SERCA2a activity determines the rate of calcium extrusion from

the cytosol and diastolic function [198]. The reduced SR Ca^{2+} content in LVF may be due to decreased Ca^{2+} pumping by SERCA2a or increased SR Ca^{2+} leak via RyR_2 channels [204]. In left heart failure, decreased and prolonged calcium transients, declined calcium load of the SR with concomitant diastolic calcium overload of the cytosol as well as reduced SERCA2a protein levels have been identified as pivotal mechanisms in progression of heart failure [205, 206]. Furthermore, downregulated SERCA2a and hypophosphorylated PLB were shown associated with impaired SR Ca^{2+} reuptake that in concert with leaky RyR_2 channels to deplete SR Ca^{2+} load contribute to development of heart failure [207]. In a MCT model of compensated right heart hypertrophy, it was proposed that increased levels of SERCA2a and decreased levels of total PLB, which inhibits SERCA2a, contributed to enhanced RV systolic function [208]. However, contrary to the above studies Kogler et al in another MCT- pressure overload study found that both SERCA2a and PLB were downregulated [209]. Decreased levels of SERCA2a were shown correlated to the degree of pressure overload and severity of RV dysfunction in a PAB model of RVF; while PLB remained unchanged [136]. In a feline model of pressure overload, severe compensated hypertrophy and heart failure secondary to pressure overload were accompanied by a significant decrease in SERCA abundance and activity which resulted in impaired contractile reserve and reduced ability to load the SR with Ca^{2+} [200]. Moreover, depletion of SERCA2 protein and subsequent decrease in its overall activity below a critical threshold, were shown to contribute to the onset and progression of heart failure [210]. In our PAB model, the protein level of SERCA2a and PLB were increased in cardiomyocytes isolated from the RV in $UCP2^{-/-}$ mice. No difference was observed in the protein level of SERCA2a and PLB in cardiomyocytes isolated from the LV. Moreover, no difference was seen in the ratio of pPLB to PLB in cardiomyocytes isolated from both RV and LV after PAB operation. SERCA2a plays an important role for sustained cardiomyocyte function and its increased expression in myocytes isolated from $UCP2^{-/-}$ mice after PAB operation is in line with enhanced cardiac contraction and relaxation observed in these cells. Paralleled by increased SERCA2a expression, the expression of PLB as SERCA2a-associated protein should have been elevated in order to make the inhibitory interaction of PLB on SERCA2a possible. The phosphorylated form of PLB lacks the inhibitory effect on SERCA2a and the unchanged ratio of pPLB to PLB makes the inhibitory effect of PLB on SERCA2a possible. Thus, $UCP2^{-/-}$ has an effect on SERCA2a on the expression level, but not on functional level via the ratio of pPLB/PLB.

Novel approaches, utilizing SERCA2a gene therapy to directly target calcium physiology in heart failure pathologies have recently been highlighted. In animal models of LVF, gene transfer of SERCA2a improved cardiac hemodynamics and cardiac contractility, and thus

resulted in increased survival [211-214]. Moreover, SERCA2a gene transfer restored the oxygen consumption of the LV to the normal level which signifies an improvement in cardiac energy utilization [212]. However, overexpression of SERCA2a in rats increased the occurrence of fatal ventricular tachyarrhythmia following infarct, which may be caused by adverse electrical remodelling due to reduced NCX expression and function triggered by elevated SR Ca^{2+} load [215]. Altogether, these findings suggest that targeting SERCA2a therapeutically in cardiac failure might be beneficial under certain conditions.

Based on the current state of research, similar pathomechanisms may underly the dysfunctional calcium handling in right and left heart failure, although the adaption process may differ. Moreover, no regional differences between cardiomyocytes isolated from the RV and the LV could be detected in regard to SR calcium uptake and expression of components of the calcium handling system [216]. Interestingly, we found unaltered expression level of SERCA2a in the cardiomyocytes from LV after PAB operation and no difference was observed between WT and $UCP2^{-/-}$ mice, although the cardiomyocytes from LV in $UCP2^{-/-}$ mice already showed increased dl/L% after PAB operation. This discrepancy cannot be explained and needs to be further investigated.

In line with our findings, downregulation of genes involved in the maintenance of Ca^{2+} homeostasis has been shown in RV myocardium of rats with right heart failure, whereas no changes in the expression levels of these genes were found in LV myocardium [209].

In accordance with the previously described pivotal role of SERCA2a in left heart failure and the potential to improve cardiac function by overexpression of SERCA2a [206], in this study we observed increased cytosolic calcium transients and faster removal of calcium in $UCP2^{-/-}$ cardiomyocytes after PAB operation compared to WT cardiomyocytes. These findings helped us to identify increased SERCA2a protein level as underlying mechanism contributing to cardiac functional alterations, indicating a similar mechanism as in left heart dysfunction. As SERCA2a and the plasmalemmal protein NCX compete for the transport of $[Ca^{2+}]_i$ and thus determine the amount of Ca^{2+} available for release by the SR upon the next contraction, we also investigated the NCX protein expression, but could find no changes. Increased NCX function can compete with SERCA2a during $[Ca^{2+}]_i$ decline, extruding more Ca^{2+} from the cell and depleting the SR. Our finding of unchanged NCX could be interpreted that the regulation of NCX expression in this experimental model is not sensitive to pressure overload and Ca^{2+} homeostasis is regulated by intracellular sources, but not Ca^{2+} influx through the plasmalemmal membrane. This interpretation is in line with the observation that in LV cells of mice and rats,

calcium is removed by SERCA ten times more effectively than by NCX [198]. Of note, NCX function is dependent not only on its expression, but also on local Na^+ and Ca^{2+} levels and action potential configuration – all of which are altered differently depending on the underlying pathophysiology [217]. Furthermore, cardiac wall stress is a major determinant for the expression of the SERCA whereas NCX may be expressed independently from it [218]. Patients with end stage of heart failure showed higher expression of NCX protein and mRNA [219, 220]. However, as no significant correlation between NCX mRNA and the clinical stage of heart failure was observed in humans, NCX mRNA level seems not suitable as a marker for myocardial dysfunction [221]. Interestingly, in patients with cardiac failure, impaired diastolic function was associated with decreased SERCA2a and unchanged NCX, whereas increased expression of the NCX was associated with preserved diastolic function. One can speculate that an increase in protein levels of NCX protein represents an important mechanism regulating diastolic calcium elimination and diastolic function in the failing human myocardium [222]. Decreased NCX to SERCA ratio in a feline LV failure model resulted in improved basal myocyte contractility and decreased rest decay which supports the hypothesis that contractile myocyte behaviour is influenced by the balanced SERCA and the NCX activity [223]. In our study, the expression level of NCX remained unchanged after PAB operation in cardiomyocytes from both WT and UCP2 deficient mice. The expression and function of the NCX in hypertrophy and heart failure are still controversial. It should be mentioned that heart failure is a complex and heterogenous disease and relative contributions of SERCA2a and NCX probably vary in different disease models, origins and stages of heart failure.

SR calcium dynamics may be altered by increased physically tethering of the SR and mitochondria via increased expression of the mitochondrial protein MFN2 which thereby creates putative microdomains that forces mitochondrial uptake of calcium released by the SR [224, 225]. In this study we could observe increased MFN2 expression in cardiomyoctes from $UCP2^{-/-}$ mice after PAB operation. In accordance to our observation, MFN2 deficient mice displayed slight heart hypertrophy and dysfunction [101]. Downregulated MFN2 expression was demonstrated in hypertrophied intact hearts and cultured myocytes and indicates that MFN2 expression levels are dependent of both the etiology and the time course of hypertrophy [152]. However, we can only speculate that these alterations are induced directly by UCP2 and lead to improved calcium handling and are not caused secondarily to improved calcium handling.

Discussion

UCP2 deficiency may regulate calcium dynamics and SERCA2a expression by increased ROS release

We further investigated by which mechanism genetic suppression of UCP2 would result in increased cardiomyocytes' calcium dynamics and SERCA2a protein expression. SERCA2a expression can be regulated by calcium and ROS sensitive pathways, e.g. via the p38-MAPK pathway and GATA [26, 134]. In this regard we could show that 1) $UCP2^{-/-}$ cardiomyocytes exhibited elevated mitochondrial superoxide concentration during ISO stimulation after PAB operation in comparison to WT cardiomyocytes and 2) inhibition of ROS production by the SOD-mimetic tempol decreased cardiomyocyte contraction and relaxation. Thus, increased ROS release from $UCP2^{-/-}$ mice after PAB may directly increase SERCA2a expression via ROS sensitive pathways and/or improve acutely calcium dynamics, which in turn can increase SERCA2a expression via calcium sensitive pathways. In this regard, it has also been shown that calcium signalling pathway activated by depleted SR/ER calcium and via activating transcription factor 6 (ATF6) modulation might lead to SERCA2a upregulation as a compensatory response which explains the elevated SERCA2a expression via calcium sensitive pathways [226]. Although the consensus is that defective Ca^{2+} sequestration by the SR is a major hallmark in the failing myocardium, there exist significant controversial reports about the molecular mechanisms including SERCA2a expression in different animal models and heart failure patients [227].Unfortunately, due to the limitation of sustaining primary isolated cardiomyocytes in culture, investigating long term effects of ROS inhibition on SERCA2a expression in adult mouse cardiomyocytes was not possible.

It is likely that redox regulation of other Ca^{2+} handling components including RyR_2 and PKA also contributes to altered Ca^{2+} handling and thereby elevated SERCA2a expression and would be a point of interest in future research. In more detail, ROS may promote cardiomyocyte contraction by activation of SERCA2a via oxidatively activated PKs, e.g. PKA, which its activation progressively removes the inhibitory influence of PLB on SERCA2a [228, 229] or by elevated SR calcium release via direct activation of RyR2 channels [228, 230] or by indirect activation via CICR by ROS promoted activation of LTCC [192]. It has been demonstrated that ROS may inhibit SR calcium reuptake by decreasing the activity of SERCA2a via direct interaction with its redox sensitive cysteine residues [231]. The differential actions of ROS may depend on the ROS concentration and localization. It is shown that low concentrations of ROS increased systolic calcium release of the SR in cardiomyocytes, while excessive ROS production reduced SR calcium release [143]. Also, $[Ca^{2+}]_c$ levels and $[Ca^{2+}]_c$ transients of rat cardiomyocytes increased markedly in response to high concentration of ROS in

cardiomyocytes isolated from rats [232]. The reciprocal interactions between Ca^{2+} and ROS signalling systems is also dependent on the type of target proteins, the ROS species, the dose as well as time point [233]. Our results concentrating on the beneficial effects of ROS are in line with a recent study in LV cardiomyocytes demonstrating that mitochondrial ROS increased calcium transient amplitude and myocyte contraction after acute stimulation with ISO and that this effect can be inhibited by ROS scavengers [234]. Animal models of right heart hypertrophy demonstrated low or even decreased level of ROS in compensated right heart hypertrophy, while excessive ROS production promotes the transition to decompensation by influencing HIF-1α stabilization [36]. Interestingly, it was demonstrated that a NOX4-dependent protective pathway, with HIF-1α being a major driver of this process, is one of the potent redox-sensitive protective pathways that is activated during chronic pressure overload [235].

Besides ROS, $UCP2^{-/-}$ may increase mitochondrial respiration via an increased pyruvate oxidation and thus promote the energy status of the cardiomyocytes. On the other hand, loss of UCP2 may decrease utilization of FA for respiration [181]. It was shown that UCP2 activity decreased the contribution of glucose to mitochondrial oxidative metabolism and elevated oxidation of alternative substrates such as FAs [118]. Also UCP2 KO cells displayed a metabolic switch from FA oxidation to glucose metabolism indicating that UCP2 promotes mitochondrial FA oxidation while mitochondrial catabolism of pyruvate is limited [111]. A metabolic switch from mitochondrial pyruvate oxidation to anaerobic glycolysis has been also shown to promote RV failure [236] while decreased mitochondrial FA oxidation have been linked to late stages of LV failure [194]. Furthermore, dysfunctional RV hypertrophy, in the setting of severe PAH, is characterized by a metabolic switch from aerobic to anaerobic metabolism [1]. Thus, promoting glucose oxidation in disfavour of FA oxidation by $UCP2^{-/-}$ might delay RVF. However, the rate of FA oxidation was preserved or even increased in physiological/adaptive LVH, but it declined during the progression to decompensated heart failure [125]. Similar results have been reported for the non-dysfunctional, mechanically-induced RV hypertrophy in rats with PAB, which exhibited high rates of FA oxidation [77]. However, in skinned muscle fibers isolated from the right heart from $UCP2^{-/-}$ mice, we could not detect any differences in pyruvate or octanoylcarnitine stimulated respiration after PAB operation. We also could not observe decreased respiration after PAB operation in WT mice compared to sham-operated mice, which has been already described in intact cardiomyocytes [236].

UCP2 gene mutations, resulting in increased UCP2 expression or function, transcriptional, translational and protein turn-over alterations, post transcriptional modifications or hormonal,

nutritional and pharmacological regulation may increase the susceptibility for patients to develop RV failure in contrast to patients that can preserve RV function even under increased RV afterload. Polymorphisms of the UCP2 promoter which affect UCP2 expression have been described to occur e.g. in atherosclerosis, diabetic retinopathy and hypertension [237]. Thus, further investigation of decreased UCP2 protein or mRNA expression levels related to recently described genetic polymorphisms may lead to development of novel biomarkers or treatments in humans susceptible for development of RVF. Furthermore underlying regulatory pathways may be exploited to enhance RV function, e.g. by micro-RNAs or targeting the PPAR pathway which regulates UCP2 expression.

Conclusion

6. Conclusion

The decompensated right heart failure is a frequent cause of death as a result of afterload by PH. It arises after mechanisms that lead to RVH and adaptive compensated right heart failure, have been exceeded. The RV is the main determinant of functional state and disease prognosis in PH. However, despite the impact of right heart failure, the pathogenesis is still not well understood.

Experimental evidence presented in this study demonstrate that UCP2 is a novel potential therapeutic target which protects the RV specifically from pressure overload-induced dysfunction and adverse remodelling. As underlying mechanism we demonstrated improved cardiomyocyte contractile phenotype and calcium dynamics, presumably via upregulation of SERCA2a and MFN2 expression. Our observations could confirm that therapeutic strategies that attempt to increase SERCA2a protein expression levels may be useful for the treatment of pressure overload-induced right heart hypertrophy.

However, whether increased SERCA2a expression is a direct consequence of UC2 deficiency or improved Ca^{2+} handling by UCP2 deficiency, remains unclear. Altogether, differences in the model of hypertrophy, extent of degree of hypertrophy and the stage of investigation could account for the discrepancies and inconsistencies between findings of the present thesis and other reports. Also, the reported differences by literature between the knockout UCP2 model and the UCP2 overexpression model could be interpreted that the overexpression systems might potentially produce an artificial biological phenomenon.

Conclusion

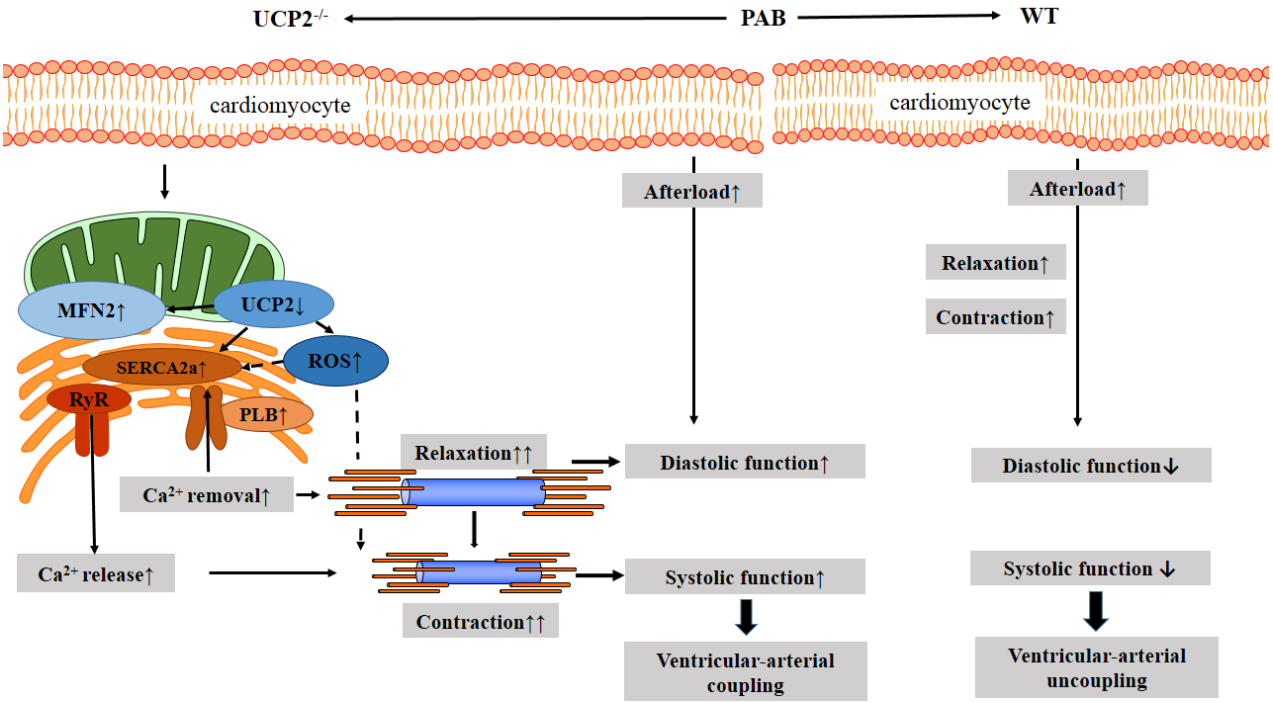

Figure 25. Genetic suppression of UCP2 leads to improved contractility in PAB

UCP2 deficient cardiomyocytes (UCP2 $^{-/-}$) showed increased expression of sarco(endo)plasmic reticulum Ca^{2+}-ATPase (SERCA2a), phospholamban (PLB) and mitofusin-2 (MFN2) after PAB. These alterations may cause improved removal of Ca^{2+} from the cytosol during diastole and subsequently enhanced release of calcium from the SR during systole. This improved Ca^{2+} handling in UCP2$^{-/-}$ cardiomyocytes may result in the observed improvement of relaxation and contraction of cardiac myofibrils after PAB and help to maintain CO in UCP2 $^{-/-}$ mice despite increased afterload. In WT mice, although the contractility of cardiomyocytes is increased after PAB, this increase may not be sufficient to overcome the increased afterload and result in a decrease of CO, a phenomenon also described as “ventricular-arterial uncoupling”.

Summary

7. Summary

RVF occurs when mechanisms compensating an increased RV afterload e.g. caused by PH, pulmonary vascular stenosis, etc. are exhausted. We hypothesized that transition from compensation to decompensation of the RV may be promoted by changes in cardiomyocytes' calcium dynamics, release of ROS and metabolism. Therefore, we investigated the role of mitochondrial uncoupling protein 2 (UCP2) in a murine model of RV hypertrophy and failure.

Pressure overload was induced by PAB in UCP2 deficient mice ($UCP2^{-/-}$) and in C57BL/6J mice. Three weeks after PAB or sham operation, right heart hypertrophy and function were determined by invasive hemodynamics and echocardiography. Contraction and relaxation of cardiomyocytes isolated from these mice, as well as cellular calcium dynamics and mitochondrial superoxide release were measured by fluorescence microscopy. Expression of the cardiac calcium handling proteins SERCA2a, PLB and the NCX, as well as MFN2, which is a mitochondrial protein that has been shown to influence mitochondrial-SR interaction, were determined by immunoblotting. Mitochondrial superoxide release and respiration were determined by the fluorescent dye MitoSOX, and high resolution respirometry, respectively.

Echocardiographic and hemodynamic assessments revealed that:

- PAB induced increased right ventricular systolic pressure (RVSP) in C57BL/6J and $UCP2^{-/-}$ mice
- PAB induced right heart hypertrophy in C57BL/6J and $UCP2^{-/-}$ mice
- PAB induced a decrease of CO and RV dilation as signs of RV decompensation in C57BL/6J mice
- Right ventricular function was preserved after PAB in $UCP2^{-/-}$ mice in contrast to C57BL/6J mice

Functional studies in cardiomyocytes revealed that:

- Cardiomyocytes isolated from the RV of both, C57BL/6J and $UCP2^{-/-}$ mice, showed increased contractility, despite decrease of CO in C57BL/6J mice
- Cardiomyocytes isolated from the RV of $UCP2^{-/-}$ mice showed further improved function after PAB compared to C57BL/6J mice
- Cardiomyocytes isolated from the RV of $UCP2^{-/-}$ mice showed improved contraction and relaxation after PAB compared to C57BL/6J mice

Summary

Analysis of calcium dynamics in isolated cardiomyocytes revealed that:

- Calcium transients were increased in cardiomyocytes from UCP2$^{-/-}$ mice after PAB compared to C57BL/6J mice
- The time of calcium to reach 50% of the basal value was decreased in cardiomyocytes from UCP2$^{-/-}$ mice after PAB compared to C57BL/6J mice

Expression of calcium handling proteins in cardiomyocytes revealed that:

- SERCA2a expression was increased in RV cardiomyocytes from UCP2$^{-/-}$ mice after PAB compared to C57BL/6J mice
- MFN2 expression was increased in RV cardiomyocytes from UCP2$^{-/-}$ mice after PAB compared to C57BL/6J mice
- NCX expression and PLB expression were unchanged in cardiomyocytes from UCP2$^{-/-}$ mice after PAB compared to C57BL/6J mice

ROS studies in cardiomyocytes and mitochondrial respiration in muscle fibers revealed that:

- Isolated cardiomyocytes from UCP2$^{-/-}$ mice after PAB showed increased mitochondrial superoxide concentration under stimulation compared to C57BL/6J mice
- ROS inhibition by superoxide scavenger tempol decreased cardiomyocyte function and contractility
- Mitochondrial respiration in permeabilized muscle fibers remained unchanged independent of genotype and treatment

We conclude that UCP2 deficiency may protect from pressure overload-induced RV dysfunction via improved cardiomyocyte calcium dynamics due to increased SERCA2a expression. Regulation of calcium dynamics due to increased SERCA2a may be regulated by increased ROS release. Therefore, UCP2 deletion and SERCA2a may be considered as novel therapeutic targets to inhibit transition from compensated RV hypertrophy to RVF.

8. Zusammenfassung

Zu einem Versagen des rechten Ventrikels (RV) kommt es, wenn das rechte Herz nicht länger in der Lage ist eine gesteigerte RV Nachlast, wie sie z.B. durch eine pulmonale Hypertonie oder eine pulmonal-vaskuläre Stenose verursacht wird, zu kompensieren.

Das Ziel dieser Arbeit war es, zu überprüfen, welche Mechanismen für den Übergang von einer kompensierten zu einer dekompensierten Rechtsherzfunktion verantwortlich sind. Die zugrundeliegende Hypothese war, dass Änderungen in der Kalziumdynamik von Kardiomyozyten oder/und die Freisetzung reaktiver Sauerstoffspezies (ROS) und des zellulären Metabolismus verantwortlich für die Dekompensation des Herzens sind.

Aufgrund seiner Beteiligung an den oben genannten Mechanismen sollte die Rolle des mitochondrialen entkoppelnden Proteins 2 (*mitochondrial uncoupling protein 2*, UCP2) beim Rechtsherzversagen in einem Mausmodell des pulmonalarteriellen *bandings* (PAB) untersucht werden.

Zur Erzeugung eines erhöhter RV Druckes wurden sowohl UCP2-defiziente ($UCP2^{-/-}$) als auch WT (C57BL/6J) Mäuse einer PAB- oder Sham- (gleicher Eingriff ohne Ligatur der Pulmonalarterie) Operation unterzogen. Drei Wochen nach der jeweiligen Operation wurde mittels hämodynamischer Messungen und Echokardiographie der Grad der Hypertrophie und die Funktion des RV untersucht. Weiterhin wurde unter Zuhilfenahme von Fluoreszenzmikroskopie die Kontraktion und Relaxation isolierter Kardiomyozyten sowie die zelluläre Kalzium-Dynamik und die mitochondriale Superoxid-Freisetzung gemessen. Zusätzlich wurde die Expression von Proteinen, die am Kalziumtransport der Kardiomyozyten beteiligt sind, der *sarco endoplasmatic reticulum calcium ATPase 2a* (SERCA2a), Phospholamban (PLB) und des sarkolemmalen Natrium-Kalzium-Austauschers (NCX), sowie von Mitofusin-2 (MFN2), dass auch die Interaktion von Mitochondrien und SR reguliert, in Kardiomyozyten anhand von Immunoblots quantifiziert. Schließlich wurde noch die Respiration mittels hochauflösende Respirometrie bestimmt.

Die echokardiographischen und hämodynamischen Untersuchungen zeigten, dass

- PAB bei C57BL/6J- und $UCP2^{-/-}$-Mäusen zu einer vergleichbaren Erhöhung des rechtsventrikulären systolischen Druck führte,
- PAB eine rechtsventrikuläre Hypertrophie bei C57BL/6J- und $UCP2^{-/-}$-Mäusen induzierte,

Zusammenfassung

- PAB eine Abnahme des CO und RV Dilatation, als Zeichen der RV Dekompensation in C57BL/6J mice induzierte und
- die rechtsventrikuläre Funktion bei UCP2$^{-/-}$-Mäusen im Gegensatz zu den WT Mäusen erhalten blieb.

Die funktionalen Studien an Kardiomyozyten verdeutlichten, dass

- die Kontraktilität von isolierten Kardiomyozyten sowohl von C57BL/6J, als auch UCP2$^{-/-}$ Mäusen erhöht war, trotz einer Abnahme des CO in C57BL/6J Mäusen,
- die Funktion, Kontraktion und Relaxation der isolierten RV Kardiomyozyten von UCP2$^{-/-}$-Mäusen nach PAB besser war als die der Kardiomyozyten von C57BL/6J-Mäusen.

Die Analyse der Kalzium-Dynamik in isolierten Kardiomyozyten wiesen daraufhin, dass

- die Kalziumströme der Kardiomyozyten von UCP2$^{-/-}$-Mäusen nach PAB gesteigert waren verglichen mit denen von C57BL/6J-Mäusen,
- bei UCP2$^{-/-}$-Mäusen die Halbwertszeit bis zum Erreichen von 50% des Kalzium-Grundwertes kürzer war als die der C57BL/6J-Mäuse.

Die Expression der Kalzium-transportierenden Proteine in den Kardiomyozyten zeigte, dass

- nach PAB die Expression von SERCA2a, MFN2 und PLB in den RV Kardiomyozyten der UCP2$^{-/-}$-Mäuse erhöht war verglichen mit der Expression der C57BL/6J-Mäusen,
- die Expression von NCX in den Kardiomyozyten der UCP2$^{-/-}$- und C57BL/6J-Mäusen nach PAB nicht unterscheidbar war.

Die Untersuchungen zur ROS-Freisetzung in Kardiomyozyten und zur mitochondrialen Respiration in Muskelfasern ergaben, dass

- isolierte Kardiomyozyten der UCP2$^{-/-}$-Mäuse nach PAB bei Stimulation eine erhöhte mitochondriale Superoxid-Konzentration aufwiesen als die der C57BL/6J-Mäuse,
- eine ROS-Inhibition durch den Superoxid-Fänger Tempol die Funktion und Kontraktilität der Kardiomyozyten beeinträchtigte,
- sich die mitochondriale Respiration permeabilisierter Muskelfasern unabhängig von Genotyp und Behandlung nicht veränderte.

Zusammenfassung

Die Ergebnisse dieser Arbeit zeigen, dass eine Deletion des UCP2-vor einer RV Dysfunktion hervorgerufen durch eine erhöhte Nachlast schützt, indem es aufgrund einer gesteigerten SERCA2a-Expression zu einer verbesserten Kalzium-Dynamik der Kardiomyozyten führt. Diese Regulierung der Kalzium-Dynamik wird vermutlich durch eine erhöhte ROS-Freisetzung hervorgerufen. Aus diesen Gründen handelt es sich bei SERCA2a und UCP2 um potentielle neue Ziele für die Therapie der maladativen Rechtsherzhypertrophie.

9. References

1. Voelkel, N.F., et al., *Right ventricular function and failure: report of a National Heart, Lung, and Blood Institute working group on cellular and molecular mechanisms of right heart failure.* Circulation, 2006. **114**(17): p. 1883-91.
2. Buckingham, M., S. Meilhac, and S. Zaffran, *Building the mammalian heart from two sources of myocardial cells.* Nat Rev Genet, 2005. **6**(11): p. 826-35.
3. Arsenijevic, D., et al., *Disruption of the uncoupling protein-2 gene in mice reveals a role in immunity and reactive oxygen species production.* Nat Genet, 2000. **26**(4): p. 435-9.
4. Markel, T.A., et al., *The right heart and its distinct mechanisms of development, function, and failure.* J Surg Res, 2008. **146**(2): p. 304-13.
5. Piao, L., G. Marsboom, and S.L. Archer, *Mitochondrial metabolic adaptation in right ventricular hypertrophy and failure.* J Mol Med (Berl), 2010. **88**(10): p. 1011-20.
6. Pokreisz P, M.G., Janssens S, *Pressure overload-induced right ventricular dysfunction and remodelling in experimental pulmonary hypertension: the right heart revisited.* European Heart Journal Supplements, 2007. **9 (Supplement H)**: p. H75–H84.
7. Cottrill, K.A. and S.Y. Chan, *Metabolic dysfunction in pulmonary hypertension: the expanding relevance of the Warburg effect.* Eur J Clin Invest, 2013. **43**(8): p. 855-65.
8. Guarracino, F., et al., *Right ventricular failure: physiology and assessment.* Minerva Anestesiol, 2005. **71**(6): p. 307-12.
9. Bogaard, H.J., et al., *The right ventricle under pressure: cellular and molecular mechanisms of right-heart failure in pulmonary hypertension.* Chest, 2009. **135**(3): p. 794-804.
10. Pangonyte, D., et al., *Cardiomyocyte remodeling in ischemic heart disease.* Medicina (Kaunas), 2008. **44**(11): p. 848-54.
11. Oka, T. and I. Komuro, *Molecular mechanisms underlying the transition of cardiac hypertrophy to heart failure.* Circ J, 2008. **72 Suppl A**: p. A13-6.
12. Sutendra, G., et al., *A metabolic remodeling in right ventricular hypertrophy is associated with decreased angiogenesis and a transition from a compensated to a decompensated state in pulmonary hypertension.* J Mol Med (Berl), 2013. **91**(11): p. 1315-27.
13. Kapur, N.K., et al., *Biventricular remodeling in murine models of right ventricular pressure overload.* PLoS One, 2013. **8**(7): p. e70802.
14. Vonk-Noordegraaf, A., et al., *Right heart adaptation to pulmonary arterial hypertension: physiology and pathobiology.* J Am Coll Cardiol, 2013. **62**(25 Suppl): p. D22-33.
15. Bishop, J.E., et al., *Increased collagen synthesis and decreased collagen degradation in right ventricular hypertrophy induced by pressure overload.* Cardiovasc Res, 1994. **28**(10): p. 1581-5.
16. Oka, T., et al., *Angiogenesis and cardiac hypertrophy: maintenance of cardiac function and causative roles in heart failure.* Circ Res, 2014. **114**(3): p. 565-71.
17. van Albada, M.E., et al., *Prostacyclin therapy increases right ventricular capillarisation in a model for flow-associated pulmonary hypertension.* Eur J Pharmacol, 2006. **549**(1-3): p. 107-16.
18. Ross, R.S., *Right ventricular hypertension as a cause of precordial pain.* Am Heart J, 1961. **61**: p. 134-5.
19. Gomez, A., et al., *Right ventricular ischemia in patients with primary pulmonary hypertension.* J Am Coll Cardiol, 2001. **38**(4): p. 1137-42.
20. van Wolferen, S.A., et al., *Right coronary artery flow impairment in patients with pulmonary hypertension.* Eur Heart J, 2008. **29**(1): p. 120-7.
21. Sano, M., et al., *p53-induced inhibition of Hif-1 causes cardiac dysfunction during pressure overload.* Nature, 2007. **446**(7134): p. 444-8.
22. Partovian, C., et al., *Heart and lung VEGF mRNA expression in rats with monocrotaline- or hypoxia-induced pulmonary hypertension.* Am J Physiol, 1998. **275**(6 Pt 2): p. H1948-56.
23. Holmstrom, K.M. and T. Finkel, *Cellular mechanisms and physiological consequences of redox-dependent signalling.* Nat Rev Mol Cell Biol, 2014. **15**(6): p. 411-21.
24. Mittal, M., et al., *Hypoxia-dependent regulation of nonphagocytic NADPH oxidase subunit NOX4 in the pulmonary vasculature.* Circ Res, 2007. **101**(3): p. 258-67.

References

25. Afanas'ev, I., *ROS and RNS signaling in heart disorders: could antioxidant treatment be successful?* Oxid Med Cell Longev, 2011. **2011**: p. 293769.
26. Santos, C.X., et al., *Redox signaling in cardiac myocytes.* Free Radic Biol Med, 2011. **50**(7): p. 777-93.
27. Giordano, F.J., *Oxygen, oxidative stress, hypoxia, and heart failure.* J Clin Invest, 2005. **115**(3): p. 500-8.
28. Chen, Q., et al., *Production of reactive oxygen species by mitochondria: central role of complex III.* J Biol Chem, 2003. **278**(38): p. 36027-31.
29. Lenaz, G., *The mitochondrial production of reactive oxygen species: mechanisms and implications in human pathology.* IUBMB Life, 2001. **52**(3-5): p. 159-64.
30. Kushnareva, Y., A.N. Murphy, and A. Andreyev, *Complex I-mediated reactive oxygen species generation: modulation by cytochrome c and NAD(P)+ oxidation-reduction state.* Biochem J, 2002. **368**(Pt 2): p. 545-53.
31. Turrens, J.F., *Mitochondrial formation of reactive oxygen species.* J Physiol, 2003. **552**(Pt 2): p. 335-44.
32. Murphy, M.P., *How mitochondria produce reactive oxygen species.* Biochem J, 2009. **417**(1): p. 1-13.
33. Sena, L.A. and N.S. Chandel, *Physiological roles of mitochondrial reactive oxygen species.* Mol Cell, 2012. **48**(2): p. 158-67.
34. Kwon, S.H., et al., *H(2)O(2) regulates cardiac myocyte phenotype via concentration-dependent activation of distinct kinase pathways.* J Mol Cell Cardiol, 2003. **35**(6): p. 615-21.
35. Takimoto, E., et al., *Oxidant stress from nitric oxide synthase-3 uncoupling stimulates cardiac pathologic remodeling from chronic pressure load.* J Clin Invest, 2005. **115**(5): p. 1221-31.
36. Redout, E.M., et al., *Right-ventricular failure is associated with increased mitochondrial complex II activity and production of reactive oxygen species.* Cardiovasc Res, 2007. **75**(4): p. 770-81.
37. Rawat, D.K., et al., *Increased reactive oxygen species, metabolic maladaptation, and autophagy contribute to pulmonary arterial hypertension-induced ventricular hypertrophy and diastolic heart failure.* Hypertension, 2014. **64**(6): p. 1266-74.
38. Qipshidze, N., et al., *Autophagy mechanism of right ventricular remodeling in murine model of pulmonary artery constriction.* Am J Physiol Heart Circ Physiol, 2012. **302**(3): p. H688-96.
39. Date, M.O., et al., *The antioxidant N-2-mercaptopropionyl glycine attenuates left ventricular hypertrophy in in vivo murine pressure-overload model.* J Am Coll Cardiol, 2002. **39**(5): p. 907-12.
40. Dhalla, A.K., M.F. Hill, and P.K. Singal, *Role of oxidative stress in transition of hypertrophy to heart failure.* J Am Coll Cardiol, 1996. **28**(2): p. 506-14.
41. van Empel, V.P., et al., *EUK-8, a superoxide dismutase and catalase mimetic, reduces cardiac oxidative stress and ameliorates pressure overload-induced heart failure in the harlequin mouse mutant.* J Am Coll Cardiol, 2006. **48**(4): p. 824-32.
42. Voelkel, N.F. and R.M. Tuder, *Hypoxia-induced pulmonary vascular remodeling: a model for what human disease?* J Clin Invest, 2000. **106**(6): p. 733-8.
43. Pak, O., et al., *Animal models of pulmonary hypertension: role in translational research.* Drug Discovery Today: Disease Models, 2010. **7**(3–4): p. 89-97.
44. Maarman, G., et al., *A comprehensive review: the evolution of animal models in pulmonary hypertension research; are we there yet?* Pulm Circ, 2013. **3**(4): p. 739-56.
45. Gomez-Arroyo, J., et al., *A brief overview of mouse models of pulmonary arterial hypertension: problems and prospects.* Am J Physiol Lung Cell Mol Physiol, 2012. **302**(10): p. L977-91.
46. Pugliese, S.C., et al., *The role of inflammation in hypoxic pulmonary hypertension: from cellular mechanisms to clinical phenotypes.* Am J Physiol Lung Cell Mol Physiol, 2015. **308**(3): p. L229-52.
47. Gomez-Arroyo, J.G., et al., *The monocrotaline model of pulmonary hypertension in perspective.* Am J Physiol Lung Cell Mol Physiol, 2012. **302**(4): p. L363-9.
48. Broderick, T.L. and T.M. King, *Upregulation of GLUT-4 in right ventricle of rats with monocrotaline-induced pulmonary hypertension.* Med Sci Monit, 2008. **14**(12): p. Br261-4.

References

49. Hessel, M.H., et al., *Characterization of right ventricular function after monocrotaline-induced pulmonary hypertension in the intact rat.* Am J Physiol Heart Circ Physiol, 2006. **291**(5): p. H2424-30.
50. Kosanovic, D., et al., *Therapeutic efficacy of TBC3711 in monocrotaline-induced pulmonary hypertension.* Respir Res, 2011. **12**: p. 87.
51. Vildbrad, M.D., et al., *Acute effects of levosimendan in experimental models of right ventricular hypertrophy and failure.* Pulm Circ, 2014. **4**(3): p. 511-9.
52. Zhang, W.H., et al., *Up-regulation of hexokinase1 in the right ventricle of monocrotaline induced pulmonary hypertension.* Respir Res, 2014. **15**: p. 119.
53. Tarnavski, O., et al., *Mouse cardiac surgery: comprehensive techniques for the generation of mouse models of human diseases and their application for genomic studies.* Physiol Genomics, 2004. **16**(3): p. 349-60.
54. Sharma, R., *Pulmonary artery banding: Rationale and possible indications in the current era.* Ann Pediatr Cardiol, 2012. **5**(1): p. 40-3.
55. Akhavein, F., et al., *Decreased left ventricular function, myocarditis, and coronary arteriolar medial thickening following monocrotaline administration in adult rats.* J Appl Physiol (1985), 2007. **103**(1): p. 287-95.
56. Bogaard, H.J., et al., *Chronic pulmonary artery pressure elevation is insufficient to explain right heart failure.* Circulation, 2009. **120**(20): p. 1951-60.
57. Hoeper, M.M., et al., *Definitions and diagnosis of pulmonary hypertension.* J Am Coll Cardiol, 2013. **62**(25 Suppl): p. D42-50.
58. Rubin, L.J., *Diagnosis and management of pulmonary arterial hypertension: ACCP evidence-based clinical practice guidelines.* Chest, 2004. **126**(1 Suppl): p. 7s-10s.
59. Lourenco, A.P., et al., *Current pathophysiological concepts and management of pulmonary hypertension.* Int J Cardiol, 2012. **155**(3): p. 350-61.
60. Simonneau, G., et al., *Updated clinical classification of pulmonary hypertension.* J Am Coll Cardiol, 2013. **62**(25 Suppl): p. D34-41.
61. Yuan, J.X. and L.J. Rubin, *Pathogenesis of pulmonary arterial hypertension: the need for multiple hits.* Circulation, 2005. **111**(5): p. 534-8.
62. Galie, N., et al., *Guidelines for the diagnosis and treatment of pulmonary hypertension: the Task Force for the Diagnosis and Treatment of Pulmonary Hypertension of the European Society of Cardiology (ESC) and the European Respiratory Society (ERS), endorsed by the International Society of Heart and Lung Transplantation (ISHLT).* Eur Heart J, 2009. **30**(20): p. 2493-537.
63. Hassoun, P.M., et al., *Inflammation, growth factors, and pulmonary vascular remodeling.* J Am Coll Cardiol, 2009. **54**(1 Suppl): p. S10-9.
64. Delgado, J.F., et al., *Pulmonary vascular remodeling in pulmonary hypertension due to chronic heart failure.* Eur J Heart Fail, 2005. **7**(6): p. 1011-6.
65. Presberg, K.W. and H.E. Dincer, *Pathophysiology of pulmonary hypertension due to lung disease.* Curr Opin Pulm Med, 2003. **9**(2): p. 131-8.
66. Humbert, M., *Pulmonary arterial hypertension and chronic thromboembolic pulmonary hypertension: pathophysiology.* Eur Respir Rev, 2010. **19**(115): p. 59-63.
67. Simonneau, G., et al., *Updated clinical classification of pulmonary hypertension.* J Am Coll Cardiol, 2009. **54**(1 Suppl): p. S43-54.
68. Matthews, J.C. and V. McLaughlin, *Acute right ventricular failure in the setting of acute pulmonary embolism or chronic pulmonary hypertension: a detailed review of the pathophysiology, diagnosis, and management.* Curr Cardiol Rev, 2008. **4**(1): p. 49-59.
69. Rameh, V. and A. Kossaify, *Role of Biomarkers in the Diagnosis, Risk Assessment, and Management of Pulmonary Hypertension.* Biomark Insights, 2016. **11**: p. 85-9.
70. Sakao, S., K. Tatsumi, and N.F. Voelkel, *Reversible or irreversible remodeling in pulmonary arterial hypertension.* Am J Respir Cell Mol Biol, 2010. **43**(6): p. 629-34.
71. Makowski, C.T., R.W. Rissmiller, and W.M. Bullington, *Riociguat: a novel new drug for treatment of pulmonary hypertension.* Pharmacotherapy, 2015. **35**(5): p. 502-19.
72. Piao, L., et al., *The inhibition of pyruvate dehydrogenase kinase improves impaired cardiac function and electrical remodeling in two models of right ventricular hypertrophy: resuscitating the hibernating right ventricle.* J Mol Med (Berl), 2010. **88**(1): p. 47-60.

References

73. Ryan, J., et al., *Mitochondrial dynamics in pulmonary arterial hypertension.* J Mol Med (Berl), 2015. **93**(3): p. 229-42.
74. Gustafsson, A.B. and R.A. Gottlieb, *Heart mitochondria: gates of life and death.* Cardiovasc Res, 2008. **77**(2): p. 334-43.
75. Williams, G.S., et al., *Mitochondrial calcium uptake.* Proc Natl Acad Sci U S A, 2013. **110**(26): p. 10479-86.
76. Frohman, M.A., *Mitochondria as integrators of signal transduction and energy production in cardiac physiology and disease.* J Mol Med (Berl), 2010. **88**(10): p. 967-70.
77. Fang, Y.H., et al., *Therapeutic inhibition of fatty acid oxidation in right ventricular hypertrophy: exploiting Randle's cycle.* J Mol Med (Berl), 2012. **90**(1): p. 31-43.
78. Gomez-Arroyo, J., et al., *Metabolic gene remodeling and mitochondrial dysfunction in failing right ventricular hypertrophy secondary to pulmonary arterial hypertension.* Circ Heart Fail, 2013. **6**(1): p. 136-44.
79. Drake, J.I., et al., *Molecular signature of a right heart failure program in chronic severe pulmonary hypertension.* Am J Respir Cell Mol Biol, 2011. **45**(6): p. 1239-47.
80. van Bilsen, M., F.A. van Nieuwenhoven, and G.J. van der Vusse, *Metabolic remodelling of the failing heart: beneficial or detrimental?* Cardiovasc Res, 2009. **81**(3): p. 420-8.
81. Chandler, M.P., et al., *Moderate severity heart failure does not involve a downregulation of myocardial fatty acid oxidation.* Am J Physiol Heart Circ Physiol, 2004. **287**(4): p. H1538-43.
82. Doenst, T., et al., *Decreased rates of substrate oxidation ex vivo predict the onset of heart failure and contractile dysfunction in rats with pressure overload.* Cardiovasc Res, 2010. **86**(3): p. 461-70.
83. Ingwall, J.S., et al., *Energetic correlates of cardiac failure: changes in the creatine kinase system in the failing myocardium.* Eur Heart J, 1990. **11 Suppl B**: p. 108-15.
84. Neubauer, S., *The failing heart--an engine out of fuel.* N Engl J Med, 2007. **356**(11): p. 1140-51.
85. Vogt, A.M. and W. Kubler, *Heart failure: is there an energy deficit contributing to contractile dysfunction?* Basic Res Cardiol, 1998. **93**(1): p. 1-10.
86. Do, E., et al., *Energy metabolism in normal and hypertrophied right ventricle of the ferret heart.* J Mol Cell Cardiol, 1997. **29**(7): p. 1903-13.
87. Oikawa, M., et al., *Increased [18F]fluorodeoxyglucose accumulation in right ventricular free wall in patients with pulmonary hypertension and the effect of epoprostenol.* J Am Coll Cardiol, 2005. **45**(11): p. 1849-55.
88. Ohira, H., et al., *Shifts in myocardial fatty acid and glucose metabolism in pulmonary arterial hypertension: a potential mechanism for a maladaptive right ventricular response.* Eur Heart J Cardiovasc Imaging, 2016. **17**(12): p. 1424-1431.
89. Kim, Y., et al., *Detection of impaired fatty acid metabolism in right ventricular hypertrophy: assessment by I-123 beta-methyl iodophenyl pentadecanoic acid (BMIPP) myocardial single-photon emission computed tomography.* Ann Nucl Med, 1997. **11**(3): p. 207-12.
90. Daicho, T., et al., *Possible involvement of mitochondrial energy-producing ability in the development of right ventricular failure in monocrotaline-induced pulmonary hypertensive rats.* J Pharmacol Sci, 2009. **111**(1): p. 33-43.
91. Rumsey, W.L., et al., *Adaptation to hypoxia alters energy metabolism in rat heart.* Am J Physiol, 1999. **276**(1 Pt 2): p. H71-80.
92. Zungu, M., et al., *Genomic modulation of mitochondrial respiratory genes in the hypertrophied heart reflects adaptive changes in mitochondrial and contractile function.* Am J Physiol Heart Circ Physiol, 2007. **293**(5): p. H2819-25.
93. Zungu, M., et al., *Expression of mitochondrial regulatory genes parallels respiratory capacity and contractile function in a rat model of hypoxia-induced right ventricular hypertrophy.* Mol Cell Biochem, 2008. **318**(1-2): p. 175-81.
94. Griffiths, E.R., et al., *Electron transport chain dysfunction in neonatal pressure-overload hypertrophy precedes cardiomyocyte apoptosis independent of oxidative stress.* J Thorac Cardiovasc Surg, 2010. **139**(6): p. 1609-17.
95. Lenaz, G., et al., *Role of mitochondria in oxidative stress and aging.* Ann N Y Acad Sci, 2002. **959**: p. 199-213.

References

96. Kajiya, M., et al., *Impaired NO-mediated vasodilation with increased superoxide but robust EDHF function in right ventricular arterial microvessels of pulmonary hypertensive rats.* Am J Physiol Heart Circ Physiol, 2007. **292**(6): p. H2737-44.
97. Guellich, A., et al., *Role of oxidative stress in cardiac dysfunction of PPARalpha-/- mice.* Am J Physiol Heart Circ Physiol, 2007. **293**(1): p. H93-h102.
98. Buermans, H.P., et al., *Microarray analysis reveals pivotal divergent mRNA expression profiles early in the development of either compensated ventricular hypertrophy or heart failure.* Physiol Genomics, 2005. **21**(3): p. 314-23.
99. Redout, E.M., et al., *Antioxidant treatment attenuates pulmonary arterial hypertension-induced heart failure.* Am J Physiol Heart Circ Physiol, 2010. **298**(3): p. H1038-47.
100. Dorn, G.W., 2nd and L. Scorrano, *Two close, too close: sarcoplasmic reticulum-mitochondrial crosstalk and cardiomyocyte fate.* Circ Res, 2010. **107**(6): p. 689-99.
101. Papanicolaou, K.N., et al., *Mitofusin-2 maintains mitochondrial structure and contributes to stress-induced permeability transition in cardiac myocytes.* Mol Cell Biol, 2011. **31**(6): p. 1309-28.
102. Sluse, F.E., et al., *Mitochondrial UCPs: new insights into regulation and impact.* Biochim Biophys Acta, 2006. **1757**(5-6): p. 480-5.
103. Cannon, B., et al., *Uncoupling proteins: a role in protection against reactive oxygen species--or not?* Biochim Biophys Acta, 2006. **1757**(5-6): p. 449-58.
104. Nedergaard, J. and B. Cannon, *The 'novel' 'uncoupling' proteins UCP2 and UCP3: what do they really do? Pros and cons for suggested functions.* Exp Physiol, 2003. **88**(1): p. 65-84.
105. Nedergaard, J., D. Ricquier, and L.P. Kozak, *Uncoupling proteins: current status and therapeutic prospects.* EMBO Rep, 2005. **6**(10): p. 917-21.
106. Rousset, S., et al., *The biology of mitochondrial uncoupling proteins.* Diabetes, 2004. **53 Suppl 1**: p. S130-5.
107. Boss, O., P. Muzzin, and J.P. Giacobino, *The uncoupling proteins, a review.* Eur J Endocrinol, 1998. **139**(1): p. 1-9.
108. Pecqueur, C., et al., *UCP2, a metabolic sensor coupling glucose oxidation to mitochondrial metabolism?* IUBMB Life, 2009. **61**(7): p. 762-7.
109. Ricquier, D. and F. Bouillaud, *Mitochondrial uncoupling proteins: from mitochondria to the regulation of energy balance.* J Physiol, 2000. **529 Pt 1**: p. 3-10.
110. Valouskova, E. and M. Modriansky, *Modulation of UCP2 expression by p38--a link to cardioprotection.* Biomed Pap Med Fac Univ Palacky Olomouc Czech Repub, 2008. **152**(1): p. 3-7.
111. Pecqueur, C., et al., *Uncoupling protein-2 controls proliferation by promoting fatty acid oxidation and limiting glycolysis-derived pyruvate utilization.* Faseb j, 2008. **22**(1): p. 9-18.
112. Rousset, S., et al., *UCP2 is a mitochondrial transporter with an unusual very short half-life.* FEBS Lett, 2007. **581**(3): p. 479-82.
113. Fink, B.D., et al., *UCP2-dependent proton leak in isolated mammalian mitochondria.* J Biol Chem, 2002. **277**(6): p. 3918-25.
114. Krauss, S., C.Y. Zhang, and B.B. Lowell, *The mitochondrial uncoupling-protein homologues.* Nat Rev Mol Cell Biol, 2005. **6**(3): p. 248-61.
115. Brookes, P.S., *Mitochondrial H(+) leak and ROS generation: an odd couple.* Free Radic Biol Med, 2005. **38**(1): p. 12-23.
116. Lopaschuk, G.D., et al., *Myocardial fatty acid metabolism in health and disease.* Physiol Rev, 2010. **90**(1): p. 207-58.
117. Motloch, L.J., et al., *By Regulating Mitochondrial Ca2+-Uptake UCP2 Modulates Intracellular Ca2+*. PLoS One, 2016. **11**(2): p. e0148359.
118. Vozza, A., et al., *UCP2 transports C4 metabolites out of mitochondria, regulating glucose and glutamine oxidation.* Proc Natl Acad Sci U S A, 2014. **111**(3): p. 960-5.
119. Pak, O., et al., *Mitochondrial hyperpolarization in pulmonary vascular remodeling. Mitochondrial uncoupling protein deficiency as disease model.* Am J Respir Cell Mol Biol, 2013. **49**(3): p. 358-67.
120. Echtay, K.S., et al., *Superoxide activates mitochondrial uncoupling protein 2 from the matrix side. Studies using targeted antioxidants.* J Biol Chem, 2002. **277**(49): p. 47129-35.

References

121. Zhang, C.Y., et al., *Genipin inhibits UCP2-mediated proton leak and acutely reverses obesity- and high glucose-induced beta cell dysfunction in isolated pancreatic islets.* Cell Metab, 2006. **3**(6): p. 417-27.
122. Waldeck-Weiermair, M., et al., *The contribution of UCP2 and UCP3 to mitochondrial Ca(2+) uptake is differentially determined by the source of supplied Ca(2+).* Cell Calcium, 2010. **47**(5): p. 433-40.
123. Vidal-Puig, A., et al., *UCP3: an uncoupling protein homologue expressed preferentially and abundantly in skeletal muscle and brown adipose tissue.* Biochem Biophys Res Commun, 1997. **235**(1): p. 79-82.
124. Nagendran, J., et al., *A dynamic and chamber-specific mitochondrial remodeling in right ventricular hypertrophy can be therapeutically targeted.* J Thorac Cardiovasc Surg, 2008. **136**(1): p. 168-78, 178.e1-3.
125. Abel, E.D. and T. Doenst, *Mitochondrial adaptations to physiological vs. pathological cardiac hypertrophy.* Cardiovasc Res, 2011. **90**(2): p. 234-42.
126. Ikeda, Y., M. Hoshijima, and K.R. Chien, *Toward biologically targeted therapy of calcium cycling defects in heart failure.* Physiology (Bethesda), 2008. **23**: p. 6-16.
127. Hasenfuss, G. and B. Pieske, *Calcium cycling in congestive heart failure.* J Mol Cell Cardiol, 2002. **34**(8): p. 951-69.
128. Talukder, M.A., et al., *Is reduced SERCA2a expression detrimental or beneficial to postischemic cardiac function and injury? Evidence from heterozygous SERCA2a knockout mice.* Am J Physiol Heart Circ Physiol, 2008. **294**(3): p. H1426-34.
129. MacLennan, D.H. and E.G. Kranias, *Phospholamban: a crucial regulator of cardiac contractility.* Nat Rev Mol Cell Biol, 2003. **4**(7): p. 566-77.
130. Santo-Domingo, J. and N. Demaurex, *Calcium uptake mechanisms of mitochondria.* Biochim Biophys Acta, 2010. **1797**(6-7): p. 907-12.
131. Kwong, J.Q., et al., *The Mitochondrial Calcium Uniporter Selectively Matches Metabolic Output to Acute Contractile Stress in the Heart.* Cell Rep, 2015. **12**(1): p. 15-22.
132. Griffiths, E.J., D. Balaska, and W.H. Cheng, *The ups and downs of mitochondrial calcium signalling in the heart.* Biochim Biophys Acta, 2010. **1797**(6-7): p. 856-64.
133. Bazil, J.N. and R.K. Dash, *A minimal model for the mitochondrial rapid mode of Ca(2)+ uptake mechanism.* PLoS One, 2011. **6**(6): p. e21324.
134. Zarain-Herzberg, A. and G. Alvarez-Fernandez, *Sarco(endo)plasmic reticulum Ca2+-ATPase-2 gene: structure and transcriptional regulation of the human gene.* ScientificWorldJournal, 2002. **2**: p. 1469-83.
135. Vangheluwe, P., et al., *Modulating sarco(endo)plasmic reticulum Ca2+ ATPase 2 (SERCA2) activity: cell biological implications.* Cell Calcium, 2005. **38**(3-4): p. 291-302.
136. Moon, M.R., et al., *Differential calcium handling in two canine models of right ventricular pressure overload.* J Surg Res, 2012. **178**(2): p. 554-62.
137. Schillinger, W., et al., *Impaired contractile performance of cultured rabbit ventricular myocytes after adenoviral gene transfer of Na(+)-Ca(2+) exchanger.* Circ Res, 2000. **87**(7): p. 581-7.
138. Brookes, P.S., et al., *Calcium, ATP, and ROS: a mitochondrial love-hate triangle.* Am J Physiol Cell Physiol, 2004. **287**(4): p. C817-33.
139. Gill, J.S., W.J. McKenna, and A.J. Camm, *Free radicals irreversibly decrease Ca2+ currents in isolated guinea-pig ventricular myocytes.* Eur J Pharmacol, 1995. **292**(3-4): p. 337-40.
140. Zima, A.V. and L.A. Blatter, *Redox regulation of cardiac calcium channels and transporters.* Cardiovasc Res, 2006. **71**(2): p. 310-21.
141. Terentyev, D., et al., *Redox modification of ryanodine receptors contributes to sarcoplasmic reticulum Ca2+ leak in chronic heart failure.* Circ Res, 2008. **103**(12): p. 1466-72.
142. Donoso, P., et al., *Stimulation of NOX2 in isolated hearts reversibly sensitizes RyR2 channels to activation by cytoplasmic calcium.* J Mol Cell Cardiol, 2014. **68**: p. 38-46.
143. Yan, Y., et al., *Bidirectional regulation of Ca2+ sparks by mitochondria-derived reactive oxygen species in cardiac myocytes.* Cardiovasc Res, 2008. **77**(2): p. 432-41.
144. Prosser, B.L., C.W. Ward, and W.J. Lederer, *X-ROS signaling: rapid mechano-chemo transduction in heart.* Science, 2011. **333**(6048): p. 1440-5.
145. Muller, O.J., et al., *Transgenic rat hearts overexpressing SERCA2a show improved contractility under baseline conditions and pressure overload.* Cardiovasc Res, 2003. **59**(2): p. 380-9.

References

146. Zarain-Herzberg, A., et al., *Decreased expression of cardiac sarcoplasmic reticulum Ca(2+)-pump ATPase in congestive heart failure due to myocardial infarction.* Mol Cell Biochem, 1996. **163-164**: p. 285-90.
147. del Monte, F., et al., *Restoration of contractile function in isolated cardiomyocytes from failing human hearts by gene transfer of SERCA2a.* Circulation, 1999. **100**(23): p. 2308-11.
148. Dash, R., et al., *Gender influences on sarcoplasmic reticulum Ca2+-handling in failing human myocardium.* J Mol Cell Cardiol, 2001. **33**(7): p. 1345-53.
149. Fernandes, A.A., et al., *SERCA-2a is involved in the right ventricular function following myocardial infarction in rats.* Life Sci, 2015. **124**: p. 24-30.
150. Afzal, N. and N.S. Dhalla, *Differential changes in left and right ventricular SR calcium transport in congestive heart failure.* Am J Physiol, 1992. **262**(3 Pt 2): p. H868-74.
151. Hobai, I.A. and B. O'Rourke, *Decreased sarcoplasmic reticulum calcium content is responsible for defective excitation-contraction coupling in canine heart failure.* Circulation, 2001. **103**(11): p. 1577-84.
152. Fang, L., et al., *Down-regulation of mitofusin-2 expression in cardiac hypertrophy in vitro and in vivo.* Life Sciences, 2007. **80**(23): p. 2154-2160.
153. Yu, H., et al., *Mitofusin 2 inhibits angiotensin II-induced myocardial hypertrophy.* J Cardiovasc Pharmacol Ther, 2011. **16**(2): p. 205-11.
154. Morita, H., J. Seidman, and C.E. Seidman, *Genetic causes of human heart failure.* J Clin Invest, 2005. **115**(3): p. 518-26.
155. Schroder, F., et al., *Increased availability and open probability of single L-type calcium channels from failing compared with nonfailing human ventricle.* Circulation, 1998. **98**(10): p. 969-76.
156. Chen, X., et al., *L-type Ca2+ channel density and regulation are altered in failing human ventricular myocytes and recover after support with mechanical assist devices.* Circ Res, 2002. **91**(6): p. 517-24.
157. He, J., et al., *Reduction in density of transverse tubules and L-type Ca(2+) channels in canine tachycardia-induced heart failure.* Cardiovasc Res, 2001. **49**(2): p. 298-307.
158. Gomez, A.M., et al., *Defective excitation-contraction coupling in experimental cardiac hypertrophy and heart failure.* Science, 1997. **276**(5313): p. 800-6.
159. Yamamoto, T., et al., *Abnormal Ca2+ release from cardiac sarcoplasmic reticulum in tachycardia-induced heart failure.* Cardiovasc Res, 1999. **44**(1): p. 146-55.
160. Marx, S.O., et al., *Coupled gating between cardiac calcium release channels (ryanodine receptors).* Circ Res, 2001. **88**(11): p. 1151-8.
161. Eisner, D.A. and A.W. Trafford, *Heart failure and the ryanodine receptor: does Occam's razor rule?* Circ Res, 2002. **91**(11): p. 979-81.
162. Rockman, H.A., et al., *Molecular and physiological alterations in murine ventricular dysfunction.* Proc Natl Acad Sci U S A, 1994. **91**(7): p. 2694-8.
163. Kojonazarov, B., et al., *The peroxisome proliferator-activated receptor beta/delta agonist GW0742 has direct protective effects on right heart hypertrophy.* Pulm Circ, 2013. **3**(4): p. 926-35.
164. Howard, L.S., *Prognostic factors in pulmonary arterial hypertension: assessing the course of the disease.* Eur Respir Rev, 2011. **20**(122): p. 236-42.
165. Vonk Noordegraaf, A. and N. Galie, *The role of the right ventricle in pulmonary arterial hypertension.* Eur Respir Rev, 2011. **20**(122): p. 243-53.
166. Schermuly, R.T., et al., *Chronic sildenafil treatment inhibits monocrotaline-induced pulmonary hypertension in rats.* Am J Respir Crit Care Med, 2004. **169**(1): p. 39-45.
167. Zhao, X., et al., *Arterial Pressure Monitoring in Mice.* Curr Protoc Mouse Biol, 2011. **1**: p. 105-122.
168. Feng, J., et al., *Catheterization of the carotid artery and jugular vein to perform hemodynamic measures, infusions and blood sampling in a conscious rat model.* J Vis Exp, 2015(95).
169. Pal, G.K. and P. Pal, *Textbook Of Practical Physiology*. 2006: Orient Blackswan.
170. Dobson, G.P., et al., *Hyperkalemic cardioplegia for adult and pediatric surgery: end of an era?* Front Physiol, 2013. **4**: p. 228.
171. Schluter, K.D. and D. Schreiber, *Adult ventricular cardiomyocytes: isolation and culture.* Methods Mol Biol, 2005. **290**: p. 305-14.

References

172. Schlueter, K.D. and H.M. Piper, *Isolation and Culture of Adult Ventricular Cardiomyocytes*, in *Practical Methods in Cardiovascular Research*, S. Dhein, F.W. Mohr, and M. Delmar, Editors. 2005, Springer. p. 557-567.
173. Schlüter, K.D. and H.M. Piper, eds. *Isolation and Culture of Adult Ventricular Cardiomyocytes*. Practical Methods in Cardiovascular Research, ed. S. Dhein, F.W. Mohr, and M. Delmar. 2005, Springer-Verlag GmbH: Heidelberg,Berlin. 557-567.
174. Ladilov, Y., et al., *Reoxygenation-induced rigor-type contracture.* J Mol Cell Cardiol, 2003. **35**(12): p. 1481-90.
175. Sommer, N., et al., *Mitochondrial cytochrome redox states and respiration in acute pulmonary oxygen sensing.* Eur Respir J, 2010. **36**(5): p. 1056-66.
176. Schluter, K.D., M. Weber, and H.M. Piper, *Effects of PTH-rP(107-111) and PTH-rP(7-34) on adult cardiomyocytes.* J Mol Cell Cardiol, 1997. **29**(11): p. 3057-65.
177. Sandoval, J., et al., *Survival in primary pulmonary hypertension. Validation of a prognostic equation.* Circulation, 1994. **89**(4): p. 1733-44.
178. van de Veerdonk, M.C., et al., *Progressive right ventricular dysfunction in patients with pulmonary arterial hypertension responding to therapy.* J Am Coll Cardiol, 2011. **58**(24): p. 2511-9.
179. Voelkel, N.F., et al., *Pathobiology of pulmonary arterial hypertension and right ventricular failure.* Eur Respir J, 2012. **40**(6): p. 1555-65.
180. Trenker, M., et al., *Uncoupling proteins 2 and 3 are fundamental for mitochondrial Ca2+ uniport.* Nat Cell Biol, 2007. **9**(4): p. 445-52.
181. Kukat, A., et al., *Loss of UCP2 attenuates mitochondrial dysfunction without altering ROS production and uncoupling activity.* PLoS Genet, 2014. **10**(6): p. e1004385.
182. Turner, J.D., et al., *Uncoupling protein-2 modulates myocardial excitation-contraction coupling.* Circ Res, 2010. **106**(4): p. 730-8.
183. Teshima, Y., et al., *Uncoupling protein-2 overexpression inhibits mitochondrial death pathway in cardiomyocytes.* Circ Res, 2003. **93**(3): p. 192-200.
184. Demaurex, N., D. Poburko, and M. Frieden, *Regulation of plasma membrane calcium fluxes by mitochondria.* Biochimica et Biophysica Acta (BBA) - Bioenergetics, 2009. **1787**(11): p. 1383-1394.
185. Murray, A.J., et al., *Uncoupling proteins in human heart.* Lancet, 2004. **364**(9447): p. 1786-8.
186. Noma, T., et al., *Possible role of uncoupling protein in regulation of myocardial energy metabolism in aortic regurgitation model rats.* Faseb j, 2001. **15**(7): p. 1206-8.
187. Li, N., et al., *[The relationship between uncoupling protein 2 expression and myocardial high energy phosphates content in abdominal aorta constriction induced heart failure rats].* Zhonghua Xin Xue Guan Bing Za Zhi, 2009. **37**(12): p. 1108-12.
188. Ji, X.B., et al., *Inhibition of Uncoupling Protein 2 Attenuates Cardiac Hypertrophy Induced by Transverse Aortic Constriction in Mice.* Cell Physiol Biochem, 2015. **36**(5): p. 1688-98.
189. Tsutsui, H., S. Kinugawa, and S. Matsushima, *Oxidative stress and heart failure.* Am J Physiol Heart Circ Physiol, 2011. **301**(6): p. H2181-90.
190. McLeod, C.J., et al., *Uncoupling proteins 2 and 3 function in concert to augment tolerance to cardiac ischemia.* J Biol Chem, 2005. **280**(39): p. 33470-6.
191. Bugger, H., et al., *Uncoupling protein downregulation in doxorubicin-induced heart failure improves mitochondrial coupling but increases reactive oxygen species generation.* Cancer Chemother Pharmacol, 2011. **67**(6): p. 1381-8.
192. Andersson, D.C., et al., *Mitochondrial production of reactive oxygen species contributes to the beta-adrenergic stimulation of mouse cardiomycytes.* J Physiol, 2011. **589**(Pt 7): p. 1791-801.
193. Brown, D.I. and K.K. Griendling, *Regulation of signal transduction by reactive oxygen species in the cardiovascular system.* Circ Res, 2015. **116**(3): p. 531-49.
194. Akhmedov, A.T., V. Rybin, and J. Marin-Garcia, *Mitochondrial oxidative metabolism and uncoupling proteins in the failing heart.* Heart Fail Rev, 2015. **20**(2): p. 227-49.
195. Gao, Y.H., et al., *[Effects of beta3-adrenergic receptor antagonist on myocardial UCP2 expression and energy metabolism in chronic heart failure rats].* Zhongguo Ying Yong Sheng Li Xue Za Zhi, 2013. **29**(4): p. 376-9, 384.
196. Hang, T., et al., *Apoptosis and expression of uncoupling protein-2 in pressure overload-induced left ventricular hypertrophy.* Acta Cardiol, 2007. **62**(5): p. 461-5.

References

197. Naeije, R. and S. Huez, *Right ventricular function in pulmonary hypertension: physiological concepts.* European Heart Journal Supplements, 2007. **9**(suppl_H): p. H5-H9.
198. Bogeholz, N., A. Muszynski, and C. Pott, *The physiology of cardiac calcium handling.* Wien Med Wochenschr, 2012. **162**(13-14): p. 278-82.
199. Meyer, M., et al., *Impaired sarcoplasmic reticulum function leads to contractile dysfunction and cardiac hypertrophy.* Am J Physiol Heart Circ Physiol, 2001. **280**(5): p. H2046-52.
200. Quaile, M.P., et al., *Reduced sarcoplasmic reticulum Ca2+ load mediates impaired contractile reserve in right ventricular pressure overload.* Journal of Molecular and Cellular Cardiology, 2007. **43**(5): p. 552-563.
201. Pieske, B., L.S. Maier, and S. Schmidt-Schweda, *Sarcoplasmic reticulum Ca2+ load in human heart failure.* Basic Res Cardiol, 2002. **97 Suppl 1**: p. I63-71.
202. Piacentino, V., 3rd, et al., *Cellular basis of abnormal calcium transients of failing human ventricular myocytes.* Circ Res, 2003. **92**(6): p. 651-8.
203. Morgan, J.P., et al., *Abnormal intracellular calcium handling, a major cause of systolic and diastolic dysfunction in ventricular myocardium from patients with heart failure.* Circulation, 1990. **81**(2 Suppl): p. Iii21-32.
204. Bers, D.M., D.A. Eisner, and H.H. Valdivia, *Sarcoplasmic reticulum Ca2+ and heart failure: roles of diastolic leak and Ca2+ transport.* Circ Res, 2003. **93**(6): p. 487-90.
205. Kawase, Y. and R.J. Hajjar, *The cardiac sarcoplasmic/endoplasmic reticulum calcium ATPase: a potent target for cardiovascular diseases.* Nat Clin Pract Cardiovasc Med, 2008. **5**(9): p. 554-65.
206. Periasamy, M., P. Bhupathy, and G.J. Babu, *Regulation of sarcoplasmic reticulum Ca2+ ATPase pump expression and its relevance to cardiac muscle physiology and pathology.* Cardiovasc Res, 2008. **77**(2): p. 265-73.
207. Marks, A.R., *Calcium cycling proteins and heart failure: mechanisms and therapeutics.* J Clin Invest, 2013. **123**(1): p. 46-52.
208. Stessel, H. and F. Brunner, *Effect of endothelin antagonism on contractility, intracellular calcium regulation and calcium regulatory protein expression in right ventricular hypertrophy of the rat.* Basic Clin Pharmacol Toxicol, 2004. **94**(1): p. 37-45.
209. Kogler, H., et al., *Mechanical load-dependent regulation of gene expression in monocrotaline-induced right ventricular hypertrophy in the rat.* Circ Res, 2003. **93**(3): p. 230-7.
210. Schultz Jel, J., et al., *Accelerated onset of heart failure in mice during pressure overload with chronically decreased SERCA2 calcium pump activity.* Am J Physiol Heart Circ Physiol, 2004. **286**(3): p. H1146-53.
211. Del Monte, F., et al., *Transcriptional changes following restoration of SERCA2a levels in failing rat hearts.* Faseb j, 2004. **18**(12): p. 1474-6.
212. Lipskaia, L., et al., *Sarcoplasmic reticulum Ca(2+) ATPase as a therapeutic target for heart failure.* Expert Opin Biol Ther, 2010. **10**(1): p. 29-41.
213. Molina, E.J., et al., *Right ventricular beneficial effects of intracoronary SERCA2a gene transfer in an experimental model of heart failure.* Folia Biol (Praha), 2010. **56**(1): p. 1-8.
214. Kawase, Y., et al., *Reversal of cardiac dysfunction after long-term expression of SERCA2a by gene transfer in a pre-clinical model of heart failure.* J Am Coll Cardiol, 2008. **51**(11): p. 1112-9.
215. Chen, Y., et al., *Constitutive cardiac overexpression of sarcoplasmic/endoplasmic reticulum Ca2+-ATPase delays myocardial failure after myocardial infarction in rats at a cost of increased acute arrhythmias.* Circulation, 2004. **109**(15): p. 1898-903.
216. Kondo, R.P., et al., *Comparison of contraction and calcium handling between right and left ventricular myocytes from adult mouse heart: a role for repolarization waveform.* J Physiol, 2006. **571**(Pt 1): p. 131-46.
217. Despa, S., et al., *Intracellular Na(+) concentration is elevated in heart failure but Na/K pump function is unchanged.* Circulation, 2002. **105**(21): p. 2543-8.
218. Prestle, J., et al., *Heterogeneous transmural gene expression of calcium-handling proteins and natriuretic peptides in the failing human heart.* Cardiovasc Res, 1999. **43**(2): p. 323-31.
219. Studer, R., et al., *Gene expression of the cardiac Na(+)-Ca2+ exchanger in end-stage human heart failure.* Circ Res, 1994. **75**(3): p. 443-53.

References

220. Reinecke, H., et al., *Cardiac Na+/Ca2+ exchange activity in patients with end-stage heart failure.* Cardiovasc Res, 1996. **31**(1): p. 48-54.
221. Piper, C., et al., *Is myocardial Na+/Ca2+ exchanger transcription a marker for different stages of myocardial dysfunction? Quantitative polymerase chain reaction of the messenger RNA in endomyocardial biopsies of patients with heart failure.* J Am Coll Cardiol, 2000. **36**(1): p. 233-41.
222. Hasenfuss, G., et al., *Relationship between Na+-Ca2+-exchanger protein levels and diastolic function of failing human myocardium.* Circulation, 1999. **99**(5): p. 641-8.
223. Weisser-Thomas, J., et al., *The Na+/Ca2+ Exchanger/SR Ca2+ ATPase Transport Capacity Regulates the Contractility of Normal and Hypertrophied Feline Ventricular Myocytes.* Journal of Cardiac Failure, 2005. **11**(5): p. 380-387.
224. Chen, Y., et al., *Mitofusin 2-containing mitochondrial-reticular microdomains direct rapid cardiomyocyte bioenergetic responses via interorganelle Ca(2+) crosstalk.* Circ Res, 2012. **111**(7): p. 863-75.
225. Givvimani, S., et al., *Dysregulation of Mfn2 and Drp-1 proteins in heart failure.* Can J Physiol Pharmacol, 2014. **92**(7): p. 583-91.
226. Thuerauf, D.J., et al., *Sarco/endoplasmic reticulum calcium ATPase-2 expression is regulated by ATF6 during the endoplasmic reticulum stress response: intracellular signaling of calcium stress in a cardiac myocyte model system.* J Biol Chem, 2001. **276**(51): p. 48309-17.
227. Armoundas, A.A., et al., *Cellular and molecular determinants of altered Ca2+ handling in the failing rabbit heart: primary defects in SR Ca2+ uptake and release mechanisms.* Am J Physiol Heart Circ Physiol, 2007. **292**(3): p. H1607-18.
228. Sag, C.M., S. Wagner, and L.S. Maier, *Role of oxidants on calcium and sodium movement in healthy and diseased cardiac myocytes.* Free Radic Biol Med, 2013. **63**: p. 338-49.
229. Brennan, J.P., et al., *Oxidant-induced activation of type I protein kinase A is mediated by RI subunit interprotein disulfide bond formation.* J Biol Chem, 2006. **281**(31): p. 21827-36.
230. Csordás, G. and G. Hajnóczky, *SR/ER–mitochondrial local communication: Calcium and ROS.* Biochimica et Biophysica Acta (BBA) - Bioenergetics, 2009. **1787**(11): p. 1352-1362.
231. Wagner, S., et al., *Reactive oxygen species-activated Ca/calmodulin kinase IIdelta is required for late I(Na) augmentation leading to cellular Na and Ca overload.* Circ Res, 2011. **108**(5): p. 555-65.
232. Gen, W., et al., *Mechanisms of Ca2+ overload induced by extracellular H2O2 in quiescent isolated rat cardiomyocytes.* Basic Res Cardiol, 2001. **96**(6): p. 623-9.
233. Yan, Y., et al., *Cross-talk between calcium and reactive oxygen species signaling.* Acta Pharmacol Sin, 2006. **27**(7): p. 821-6.
234. Andersson, D.C., et al., *Enhanced cardiomyocyte Ca(2+) cycling precedes terminal AV-block in mitochondrial cardiomyopathy Mterf3 KO mice.* Antioxid Redox Signal, 2011. **15**(9): p. 2455-64.
235. Zhang, M., et al., *NADPH oxidase-4 mediates protection against chronic load-induced stress in mouse hearts by enhancing angiogenesis.* Proc Natl Acad Sci U S A, 2010. **107**(42): p. 18121-6.
236. Archer, S.L., et al., *Metabolism and bioenergetics in the right ventricle and pulmonary vasculature in pulmonary hypertension.* Pulm Circ, 2013. **3**(1): p. 144-52.
237. Donadelli, M., et al., *UCP2, a mitochondrial protein regulated at multiple levels.* Cell Mol Life Sci, 2014. **71**(7): p. 1171-90.

Acknowledgments

10. Acknowledgements

This dissertation would not have been possible without the help of many people. First of all and in particular, I would like to express my sincere gratitude and appreciation to "my supervisor", Prof. Dr. Norbert Weissmann, for providing me the opportunity to do my PhD work in his group, his financial support throughout my PhD study, and for his ceaseless supervision, guidance and support.

I would like to thank Dr. Natascha Sommer "my postdoc" for the constructive scientific supervision of my project besides the detailed and critical assessment of my work. My deepest appreciation to Dr. Natascha Sommer for her non-stop scientific and non-scientific support and care during my PhD study.

I owe a lot of profound gratitude to my "great colleague" Dr. Oleg Pak, who was always beside me throughout my PhD research work. His thoughtful advice and scientific feedback were key to my progress.

I was privileged to have the expertise, scientific discussion and fruitful collaboration of Prof. Klaus-Dieter Schlüter and Dr. Rolf Schreckenberg from the Department of Physiology in designing, performing and analyzing calcium studies in my project. It has been a great pleasure to have your extensive support.

I would like to thank Dr. Akylbek Sydykov for his wonderful and constant support, guidance and motivation. Your invaluable professional comments, inputs and suggestions were of great help.

My special gratitude goes to my dear friend Dr. Christine Vohwinkel from the University of Colorado for her unconditional scientific discussions and indispensable suggestions throughout my thesis besides her great help in verification of English language. It was a great pleasure to have your encouragement and inspiration.

My sincere thanks belongs to Dr. Dale Brown from the University of Colorado for the review of this thesis and his helpful insights and comments. It was such an honor to have your support.

My special thanks goes to Dr. Daniel Cannon from the San Diego State University for the verification of the English language in my thesis.

I would like to thank Dr. Baktybek Kojonazarov and Dr. Akylbek Sydykov for the good cooperation in doing and analyzing the echocardiographic measurements of the mice in my project.

I would like to acknowledge Mrs. Karin Quanz and Mrs. Ingrid Breitenborn-Müller for the great support and care besides the open council in all occupational and private conditions.

Acknowledgments

I am deeply grateful to Mrs. Nadine Woitasky for her friendly and great cooperation and help regarding the performance of calcium studies in my project.

My sincere thanks are owned to all of the Weissmann group members whom I have been fortunate enough to work with during my doctoral study. I would like to specially thank Dr. Dorothea Greifenberg, Dr. Daniela Haag, Dr. Simone Kraut, Dr. Monika Malczyk, Dr. Mareike Gierhardt, Ms. Sabine Hurka, Mrs. Carmen Homberger, Ms. Elisabeth Kappes, Ms. Christina Vroom, Ms. Katharina Schaefer, Mrs. Ewa Bieniek, Mrs. Andrea Mohr, and Mr. Jochen Wilhelm for their great support.

Der Lebenslauf wurde aus der elektronischen Version der Arbeit entfernt.

The curriculum vitae was removed from the electronic version of the paper.